UNIVERSIDAD NACIONAL AUTÓNOMA DE MÉXICO
PROGRAMA DE MAESTRÍA Y DOCTORADO EN INGENIERÍA
ENERGÍA-SISTEMAS ENERGÉTICOS

Numerical study of the liquid metal flow and heat transfer in ducts under localized magnetic fields

TESIS
QUE PARA OPTAR POR EL GRADO DE:
DOCTORA EN INGENIERÍA

PRESENTA:
M. en I. Veronica Solano Olivares

TUTOR PRINCIPAL:
Dr. Sergio Cuevas García, Instituto de Energías Renovables, UNAM
CO-TUTOR:
Dr. Aldo Figueroa Lara, Conahcyt-CInC, UAEM

COMITÉ TUTOR:
Dr. Eduardo Ramos Mora, IER-UNAM
Dr. Jorge Antonio Rojas Menéndez, IER-UNAM
Dr. Rubén Ávila Rodríguez, Facultad de Ingeniería, UNAM

CIUDAD DE MÉXICO, Noviembre 2023

JURADO ASIGNADO:

Presidente: Dr. Eduardo Ramos Mora, IER-UNAM

Secretario: Dr. Sergio Cuevas García, IER-UNAM

1er. Vocal: Dr. Aldo Figueroa Lara, Conahcyt-CInC, UAEM

2do. Vocal: Dr. Rubén Ávila Rodríguez, Facultad de Ingeniería, UNAM

3er. Vocal: Dr. Jorge Antonio Rojas Menéndez, IER-UNAM

Lugar o lugares donde se realizó la tesis: Instituto de Energías Renovables, Temixco, Morelos, México.
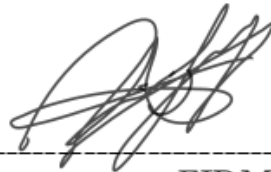
TUTOR DE TESIS:

Dr. Sergio Cuevas García   **Dr. Aldo Figueroa Lara**

_____   _____
FIRMA   **FIRMA**

Acknowledgement

Dedication

Dedicated to my mother, Rachel, my father, Higinio, and my siblings, Leticia, Karina, and Alexander.

Resumen

En esta tesis se realiza un estudio numérico de la dinámica de flujos de metal líquido en ductos de sección transversal rectangular uniforme sujetos a un campo magnético generado por imanes permanentes, tanto con distribución homogénea como no homogénea. El uso de fuerzas electromagnéticas en fluidos eléctricamente conductores, en particular, metales líquidos, puede modificar considerablemente los patrones de flujo e incluso propiciar agitación del fluido. La presencia de un campo magnético localizado intenso genera una fuerza de Lorentz que se opone al flujo del fluido actuando como un obstáculo no intrusivo y generando vorticidad aguas abajo del campo magnético localizado. Por lo tanto, surge el interés de investigar el impacto de diferentes patrones de flujo en la transferencia de calor. Para este propósito, se inicia presentando la modelación matemática de flujos de metal líquido en ductos, utilizando dos formulaciones de las ecuaciones fundamentales, basadas en el campo magnético inducido y el potencial eléctrico, bajo la aproximación de número de Reynolds magnético pequeño. Con el objetivo de lograr una comprensión profunda de los fenómenos físicos involucrados en los flujos magnetohidrodinámicos (MHD), en esta tesis se desarrollaron códigos numéricos basados en el Método de Volúmen Finito, implementados en un dominio numérico con mallas uniformes y no uniformes. El objetivo principal de esta investigación es caracterizar el comportamiento dinámico y térmico de los flujos de metal líquido bajo la acción de campos magnéticos inhomogéneos, al variar diversas condiciones tales como la conductividad eléctrica de las paredes del ducto, el tamaño del ducto y la configuración del campo magnético, junto con los parámetros adimensionales que gobiernan el flujo, a saber, el número de Reynolds, el parámetro de interacción, el número de Hartmann y el número de Péclet.

Con el propósito de analizar diferentes niveles de aproximación, a lo largo de este trabajo se exploran modelos bidimensionales (2D), cuasi-bidimensionales (Q2D) y tridimensionales (3D) para permitir una comprensión gradual de la física involucrada. Al contrastar los resultados de las diferentes aproximaciones, se discuten las ventajas y limitaciones inherentes a cada modelo.

Para validar el código numérico 3D desarrollado y garantizar su precisión y confiabilidad, se realiza una comparación de las soluciones numéricas con soluciones analíticas exactas disponibles en el límite de flujo completamente desarrollado. Con este propósito, se obtiene una nueva solución analítica exacta. Una validación adicional se lleva a cabo al comparar la simulación numérica 3D con los resultados experimentales reportados por Domínguez *et al.* [45], donde se generaron caudas mediante un campo magnético localizado en un flujo de metal líquido impulsado por una bomba electromagnética en un circuito conformado por un ducto rectangular de sección transversal delgada. En este análisis, la interacción entre las fuerzas

inerciales y electromagnéticas observada experimentalmente se replica de manera consistente por el modelo numérico. Además, se identifican características del flujo que no pueden ser observadas experimentalmente, como la transición de patrones de flujo estacionarios a patrones de flujo dependientes del tiempo.

Adicionalmente, se presenta una nueva solución analítica obtenida por el método de perturbaciones para el flujo alrededor de un dipolo magnético puntual.

Finalmente, se analiza el desempeño térmico de los flujos estudiados bajo diversas condiciones y se muestra que el uso de campos magnéticos localizados en flujos de metal líquido en ductos es una opción conveniente para mejorar la transferencia de calor.

Abstract

This thesis presents a numerical study of the dynamics of liquid-metal flows in ducts of uniform rectangular cross-section subject to a magnetic field generated by permanent magnets either with a homogeneous or non-homogeneous distribution. The use of electromagnetic forces in electrically conducting fluids, particularly liquid metals, can considerably alter flow patterns and even induce fluid stirring. The presence of a strong localized magnetic field generates a Lorentz force that opposes the flow, acting as a non-intrusive obstacle and producing vorticity downstream of the localized magnetic field. Therefore, there is an interest to investigate the impact of different flow patterns on heat transfer. For this purpose, the mathematical modeling of liquid-metal duct flows is presented as a primary step, using formulations of the governing equations based on the induced magnetic field and the electric potential, under the assumption of low magnetic Reynolds number. With the aim of achieving a deep understanding of the physical phenomena involved in magnetohydrodynamic (MHD) flows, in this thesis numerical codes were developed based on the Finite Volume Method, implemented in a numerical domain with uniform and non-uniform meshes. The main objective of this research is to characterize the dynamic and thermal behavior of liquid metal flows under the action of inhomogeneous magnetic fields, by varying various conditions such as the electrical conductivity of the duct walls, the size of the duct and the configuration of the magnetic field, along with the dimensionless parameters that govern the flow, namely the Reynolds number, the interaction parameter, the Hartmann number and the Péclet number. With the aim to analyse different levels of approximation, throughout this work, two-dimensional (2D), quasi-two-dimensional (Q2D) and three-dimensional (3D) models are explored to allow a gradual comprehension of the physics involved. By comparing results of different approaches, advantages and limitations of each model are discussed.

To validate the 3D numerical code developed and guarantee its accuracy and reliability, a comparison of numerical solutions with available exact analytical solutions in the limit of fully developed flow is performed. For this purpose, a new exact analytical solution is obtained. An additional validation is performed by comparing the 3D numerical simulation against experimental results reported by Domínguez *et al.* [45] where wakes generated by a fixed localized magnetic field in liquid-metal flow driven by an electromagnetic pump in a loop formed by a rectangular duct of slender cross-section was carried out. In this analysis, the interplay between inertia and electromagnetic forces observed experimentally is consistently replicated by the numerical model. Moreover, flow features that can not be observed experimentally are identified, such as the transition from steady to time-dependent flow patterns. Furthermore, a new analytical perturbation solution is reported for the creeping flow past a magnetic point dipole.

6

Finally, the thermal performance of the flows studied under various conditions is analyzed and it is shown that the use of localized magnetic fields in liquid metal flows in ducts is a suitable option for heat transfer enhancement purposes.

Contents

Introduction

The interaction of flows of electrically conducting fluids and magnetic fields arises in many relevant problems ranging from large-scale phenomena in astrophysics, solar physics, and geophysics, as well as in many technological applications. These problems are within the realm of Magnetohydrodynamics (MHD) that can be defined as the fluid dynamics of electrically conducting (non-magnetizable) fluids such as liquid metals, electrolytes and plasmas, under magnetic fields [1]. In terrestrial applications MHD has witnessed significant growth in various industrial and technological fields since the use of electromagnetic interactions provides a versatile and non-intrusive way to manipulate and control electrically conducting fluids. Particularly, areas such as the electromagnetic processing of materials, fluid monitoring and energy production have benefited from MHD methods, specially in the metallurgical, chemical and nuclear industries, among others.

Due to the complexity and adaptability of MHD flows, they are of interest from both a practical and a theoretical point of view. As other branches of fluid dynamics, the study of these flows can be grasped from theoretical, experimental and numerical simulation approaches. In the analysis of a particular flow, whenever possible the use of at least two of these approaches provides more confidence in results.

The present work deals with liquid metal flows in ducts under magnetic fields which is a classical topic of magnetohydrodynamics and one of the most studied due to several technological applications such as electromagnetic pumps and valves, electromagnetic flowmeters, MHD electric generators and blankets for fusion reactors. In all of them, the understanding of the flow dynamics is fundamental for the correct design and operation of the devices. In some applications, heat transfer is of paramount importance, as occurs in liquid metal blankets for fusion reactors that, in addition to breeding the tritium required for the reaction, are intended to receive the heat from the fusion reaction and transport it to another place where it is transformed into electricity, acting as a heat exchanger. This is a subject of ongoing research and different blanket concepts have been developed to promote enhanced heat transfer [2].

MHD flows in ducts under uniform magnetic field

The pioneering papers by Hartmann [3] and Hartmann and Lazarus [4] published in 1937, constitute the first theoretical and experimental study of a liquid metal duct flow under a magnetic field. They analysed the flow of mercury and were able to characterize the changes in drag and the suppression of turbulence by the action of the magnetic field. In general, MHD flow patterns are determined by the

magnetic forces that arise in the conducting fluid owing to the interaction of the applied magnetic field with electric currents induced by the fluid motion within the same applied field. In turn, current paths (particularly the way they close) depend on the electrical conductivity not only of the liquid metal but also of the duct walls. Therefore, ducts with walls of distinct conductivity may lead to very different flow patterns. As a matter of fact, many cases have been treated in the literature (see for instance [5, 6]). As most MHD flows at laboratory and industrial scale, liquid metal MHD duct flows are characterized by small values of the magnetic Reynolds number, which is defined as $R_m = \mu_0 \sigma U L$, where μ_0 is the magnetic permeability of vacuum, and σ is the electrical conductivity of the fluid, while U and L are characteristic scales of velocity and length. The condition $R_m \ll 1$ implies that induced magnetic fields are negligible compared with the applied magnetic field. Another key dimensionless parameters that govern liquid metal MHD duct flows are the Reynolds number, $Re = UL/\nu$, and the Stuart number or interaction parameter, $N = \sigma B_0^2 L/\rho U$, where ν is the kinematic viscosity of the fluid and B_0 is a characteristic value of the applied magnetic field. While the Reynolds number compares inertia versus viscous forces, the interaction parameter gives the ratio of magnetic forces to inertia. Another important parameter is the Hartmann number, defined as $Ha = BL(\sigma/\rho\nu)^{1/2}$, whose square can be interpreted as the ratio of magnetic to viscous forces. In fact, only two of these dimensionless numbers are independent since the interaction parameter can be expressed in therm of Re and Ha in the form $N = Ha^2/Re$. Finally, the conductance ratio, defined as $c = \sigma_w t_w/\sigma L$, where σ_w and t_w are the electrical conductivity and thickness of the wall, is another important parameter that compares the conductance of the wall and that of the fluid [6].

During the sixties, seventies and eighties of the last century, a great effort was devoted to the search of analytical solutions of liquid metal MHD duct flows in restricted conditions, mainly assuming a uniform constant magnetic field. Among the most relevant contributions in this topic are the papers by Shercliff, Hunt, Ludford and Walker, see for instance [7, 8, 9, 10, 11, 12] where fully developed incompressible flows in ducts with rectangular cross-section under a uniform magnetic field transverse to a pair of walls were analysed. For instance, Hunt obtained an exact solution [8] for the velocity and induced magnetic field for a duct with perfectly conducting walls perpendicular to the applied field and thin conducting walls parallel to the field. In these conditions, the electric current distribution may lead to the formation of the so-called "M-shaped" or "M-type" velocity profiles which are important in the context of liquid-metal blanket applications [13]. Hunt's solution showed that under strong magnetic field conditions high velocities are found close to the walls parallel to the field while the core remains almost stagnant. This flow pattern is particularly interesting since the presence of high velocities near the walls may promote the appearance of instabilities [14] and eventually turbulence [15]. In fact, recently an analytical solution of the heat transfer problem for the Hunt's flow has been reported [16]. In general, exact solutions of MHD flows in ducts have been extensively used to validate numerical codes, see for instance [17, 18, 19, 20].

MHD flows under non-uniform magnetic field

On the other hand, liquid metal duct flows under non-uniform magnetic fields have been much less explored although, as an extension of the flows under uniform magnetic fields, attention has been devoted to the problem of the duct flow at the entrance or exit of a magnetic field [21, 22, 23]. While in the seventies of last century an attempt was made to discern how a flow of liquid metal is affected when a localized magnetic field acts on it [24, 25], it has been in the last two decades that this problem has been more extensively studied. As a matter of fact, it has been recognized that internal shear layers can be created in liquid metal flows due to non-uniformities in the applied magnetic field, particularly when the magnetic source is confined in a small zone compared with the full flow region. Hence, induced currents in the liquid metal interact with the applied magnetic field, giving rise to a localized Lorentz force that, acting as an obstacle, brakes the fluid and creates vorticity. The term *magnetic obstacle* was coined to describe this phenomenon [26] which is mainly governed by two dimensionless parameters (instead of one as in the hydrodynamic flow past a bluff body), for instance, the Reynolds number, *Re*, and the interaction parameter N. In low-Reynolds number flows, a magnetic obstacle can give rise to steady flow patterns that display structures not observed in the flow past solid obstacles [27, 28]. On the other hand, if inertial effects are sufficiently strong in a free flow, the obstruction created by the magnetic obstacle can lead to unstable behavior manifested in the appearance of vortex shedding and the formation of a time-dependent wake [26]. When the flow is confined as occurs in a duct flow, steady flow patterns different from those observed in the flow past solid obstacles arise [29, 30]. Incidentally, the rich dynamic behavior presented in liquid metal flows past magnetic obstacles, as well as some technological applications of this kind of flows, has motivated several theoretical and experimental studies in the last two decades.

In fact, an important research project was carried out at the Technical University of Ilmenau, Germany, with the objective of developing a promising technological application, namely, the Lorentz force velocimetry [31, 32]. The main principle behind this application is that if a small magnet is placed externally but close to a duct where an electrically conducting liquid flows, the relative motion between the liquid and the magnetic field of the magnet will induce electric currents in the liquid that, in turn, generate an induced magnetic field that is able to drag the external magnet. By measuring the Lorentz force exerted on the magnet, the velocity of the liquid can be obtained. This technological application motivated a great number of works that have explored the dynamics involved in flows of conducting liquids past localized magnetic fields and the exerted magnetic forces [33, 34, 35]. Although Lorentz force velocimetry is mainly intended for applications in metallurgy [36], it has been shown that it is also a suitable method for measuring velocities in low conductivity fluids, for instance, electrolytes [37, 38, 39].

From the fluid dynamics perspective, using a two-dimensional numerical model Cuevas *et al.* [26] investigated the laminar free flow of a liquid metal past a localized field generated by a small squared magnet when inertia is not negligible. They found the formation of a wake behind the magnetic obstacle that displays two elongated

streamwise vortices that remain steady as long as the Hartmann number does not exceed a critical value. Once this value is reached, the wake becomes unstable and a vortex shedding process similar to the one observed in the flow past bluff bodies is established. The same authors [27] found that under creeping flow conditions a vortex dipole created by the magnetic interaction can develop into a four vortex pattern as the Hartmann number increases. Further, Votyakov and Kassinos [28] showed that increasing the Hartmann number even more, a pattern of six nested vortices may appear. This kind of pattern was also found in electromagnetically forced flows in thin liquid metal layers [40].

Votyakov *et al.* [29] conducted an experimental study and three-dimensional numerical simulations of the flow past a magnetic obstacle in a rectangular duct finding that the steady flow undergoes a first bifurcation that leads to the formation of a pair of vortices within the region of magnetic field (named inner magnetic vortices), while a second bifurcation originates a pair of attached vortices that are linked to the inner vortices by connecting vortices so that a pattern of six vortices is formed. In a later study, Votyakov *et al.* [30] studied flow characteristics for different magnetic field configurations by varying the the constrainment factor or blockage ratio, $\beta = M_y/L_y$, which which relates the size of the magnet, M_y, to the size of the duct in the transverse section, L_y. They found that the flow displays different stationary recirculation patterns, namely, two magnetic vortices at small β, a six-vortex ensemble at moderate β, and no vortices at large β. Therefore, the geometry of the flow container and the magnetic field location can impact the flow blocking effect of the obstacle. In particular, a higher blockage ratio can lead to unstable vortex patterns and fluctuant flow near the walls [41]. This behavior is a result of the interplay between MHD instability and shear flow instability, as demonstrated in Samsami *et al.* [42]. Votyakov *et al.* [30] also pointed out that the friction imposed by no-slip walls stabilizes the flow and can originate the delay of the critical Reynolds number for vortex shedding. In some cases, the increase of the wake stability could prevent the appearance of vortex shedding, in contrast with two-dimensional simulations [26]. However, using 3D simulations Votyakov *et al.* [43] reported the appearance of vortex shedding with a wake that can be symmetric or anti-symmetric depending on initial and inlet flow conditions.

In an interesting experimental study, Sasami *et al.* investigated the flow patterns created by a moving permanent magnet underneath a free quiescent liquid metal layer [42]. The magnet was dragged with different constant velocities so that the range of Reynolds number explored was from 125 to 2000. They observed a rich variety of flow patterns in the wake created by the moving magnet, for instance, the formation of vortices or their suppression, symmetry breakdown, vortex duplication and vortex shedding. A quasi-two-dimensional behavior was found for large values of the interaction parameter. Further, different instability mechanisms were identified as the Reynolds number and the interaction parameter were varied. In addition, Prinz *et al.* [44] carried out a numerical simulation of this experiment, being able to successfully reproduce some of the observed flow structures. The authors found that the process of vortex formation is accompanied by a decrease of the streamwise component of the Lorentz force compared to the time when the fluid is still quiescent.

An important reference for the present work is experimental and numerical study

performed by Domínguez *et al.* [45], where the wake dynamics behind a magnetic obstacle in a liquid metal duct flow was analysed. Through UDV measurements the stability and dynamics of the wake were explored and contrasted with a quasi-two-dimensional numerical model. It was found that for a given Hartmann number, the flow transits from a steady state to a time-dependent state as the Reynolds number is increased, as occurs in the wake of a rigid obstacle. However, in sharp contrast with the hydrodynamic case, when the Reynolds number is increased further, the flow becomes steady again. We use the experimental data of this study to validate the developed three-dimensional numerical code and overcome the limitations of the quasi-two-dimensional approach in fully understanding this flow.

Apart from the existing interest in the transition to turbulence in MHD flows under a uniform magnetic field [46, 47], the transition from a laminar to a turbulent regime in the liquid metal flow in a rectangular duct under a localized magnetic field has also been the subject of scientific investigation. From three-dimensional numerical simulations, Kenjeres *et al.* [48] found steady solutions for $100 \leq Re \leq 400$ and $N \leq 11.5$ with no vortices, two vortices and up to six vortices. He showed that even under laminar inflow conditions, by increasing the Reynolds number to $Re = 900$, vortex shedding appear and turbulent bursts are found in the magnetic wake region. Further, the author stress that turbulence was locally sustained in proximity to the edge of the magnetic wake. Kenjeres [49] also studied the channel flow configuration with electrically and thermally insulated horizontal walls containing one, two or three magnetic dipoles. He identified areas of intermittent velocity downstream of the magnetic obstacle [49] and experimentally confirmed the occurrence of vortex bursts in a duct caused by an elementary structure, with strong fluctuations of velocity in the laminar environment visualized as described in [50]. Furthermore, Tympel *et al.* [51] showed that turbulence can be initiated in a laminar flow through the presence of a strong magnetic point dipole field. They analyzed different orientations of the dipole and determined that the spanwise orientation present the most efficient generation of turbulence.

Heat transfer enhancement

The use of electromagnetic forces for heat transfer enhancement has been explored for different applications such as the processing of materials and nuclear fusion reactors. In fact, the versatility provided by the use of magnetic fields can lead to the design of innovative heat exchangers. As many technological applications rely on the optimal performance of heat exchangers, having reliable methods of improving heat transfer becomes of paramount importance. We can distinguish between active methods that require external power, and passive methods that require no external power. Due to practical and economic reasons, passive methods are usually preferred in many applications. With these methods, the heat transfer rate is increased by promoting changes in the flow pattern, for instance, by inserting swirl devices that lead to the enhancement of the convective heat transfer and to the increase of the pressure drop. In most common heat exchangers, these devices can be surface or geometrical modifications that promote swirl into the bulk flow while disrupting the

boundary layer at the walls. The appearance of vortex motion may increase the heat transfer coefficient and consequently the Nusselt number [52].

One of the most common strategies to enhance the heat transfer is by placing solid obstacles in the flow region. In particular, the use of extended surfaces like fins is widely employed with the aim of generating swirl and eventually turbulence. But mechanical methods are not the only option to promote vortex motion when electrically conducting fluids such as liquid metals come into play. Due to its high thermal conductivity, liquid metals under magnetic fields offer an alternative to the usual hydrodynamic flows in many technological applications, particularly, for cooling and heat transfer enhancement purposes, as occurs in metallurgical operations and coolant systems of fusion reactors. In fact, flows around solid obstacles have been investigated with the purpose of improving the heat transfer in MHD channel flows under a uniform magnetic field [53]. Other studies have explored active methods, for instance, by injecting a non-uniform electric current through electrodes under a uniform magnetic field [54]. A combination of passive and active methods have been also analysed to enhance the heat transfer from the heated sidewall of an MHD duct under a uniform magnetic field by using a cylinder wake mechanism augmented with a current injection forcing that enhances instability behind the cylinder [55]. In turn, the effects on the convective heat transfer of non-uniform magnetic fields have been investigated in a liquid metal flow in a parallel plate channel, where electric currents positioned underneath the channel walls created a "magnetic-ribs" distribution [56]. Actually, the heat transfer in liquid metal duct flows can be enhanced without solid obstacles or injected currents by the use of localized magnetic fields created by permanent magnets, which gives rise to magnetic obstacles [26]. In fact, the Lorentz force produced in the fluid by the interaction of the induced electric currents and the localized magnetic field brakes the liquid metal and creates vortical flows that improve the convective heat transfer. As a matter of fact, some previous works have investigated the influence on heat transfer of one central magnetic obstacle [41, 57] or a row of magnetic obstacles [58] in a duct flow, although only a few values of the interaction parameter and Reynolds number were examined.

In this thesis, we use a numerical simulation approach to study the dynamics and heat transfer that take place in liquid metal flows in ducts under inhomogeneous magnetic fields. The objective is to deepen the understanding of this type of flows through the development of a reliable numerical tool capable of exploring the flow in a wide range of governing parameters. This implies the validation of the numerical code through analytical results (in the proper limits) and experimental data. Motivated by the search of non-intrusive methods for heat transfer enhancement purposes, the aim is also to determine, through numerical simulations, proper conditions that allow the enhancement of heat transfer in liquid metal flows in ducts under inhomogeneous magnetic fields.

After this introductory chapter, the structure of the thesis is as follows. Chapter 2 serves as a guide for the mathematical formulation of the following chapters. It contains the fundamental MHD equations considering the formulations based on either the induced magnetic field (B-formulation) or the one based on the electric potential (ϕ-formulation), as well as the numerical strategies implemented in the

numerical code developed in this work to solve the governing equations.

In Chapter 3, the dynamics and heat transfer of a liquid metal flow in a duct under the presence of a single localized magnetic field is explored through a simplified two-dimensional numerical model, considering a wide interval of Hartmann numbers for fixed Reynolds numbers.

In Chapter 4, analytical solutions of MHD flows in rectangular ducts with different arrays of conducting walls under a uniform magnetic field are presented with the aim of comparing and validating, in the proper limit, the three-dimensional numerical simulations obtained with the developed code.

Chapter 5 presents a perturbation analytical solution of the creeping liquid metal flow past a point magnetic dipole, which reproduces the flow pattern of six vortices. Further, we addresses the full three-dimensional numerical simulation of the experiment performed at IER-UNAM [45], namely, the liquid metal duct flow under a localized magnetic field with a fixed Hartmann number and different Reynolds numbers. The main objective is to determine the interplay between inertia and magnetic forces. Moreover, extending the range of dimensionless parameters beyond those explored experimentally, different flow patterns of stationary vortices are reproduced and their three-dimensional structure are discussed.

Chapter 6 explores the heat transfer effects of different configurations of localized magnetic fields. For this purpose, three-dimensional numerical simulations are implemented applying thermal boundary conditions of the first and second kind. Finally, in Chapter 7 the conclusions and some recommendations for future work are presented.

Fundamental MHD equations and numerical methodology

In this chapter, the fundamental equations of Magnetohydrodynamics are presented, summarizing briefly the assumptions required to couple the fluid dynamic equations with the equations of classical electrodynamics. In addition, the formulation of the MHD equations in terms of either the induced magnetic field and the scalar electric potential are presented. Finally, the methodology used in this work for the numerical solution of the governing equations is discussed.

2.1 Governing Equations

In fluid dynamics, the conservation of mass for an incompressible fluid and the Newton's second law are expressed through the equations [59]

$$\nabla \cdot \boldsymbol{u} = 0, \tag{2.1}$$

$$\rho \left(\frac{\partial \boldsymbol{u}}{\partial t} + (\boldsymbol{u} \cdot \nabla) \boldsymbol{u} \right) = -\nabla P + \mu \nabla^2 \boldsymbol{u} + \boldsymbol{f}, \tag{2.2}$$

where $\boldsymbol{u}$ is the velocity field, P is the pressure field, ρ is the density of the fluid and μ is the dinamic viscosity. Equation (2.1) is known as the continuity equation while (2.2) is the Navier-Stokes equation, where $\boldsymbol{f}$ is a body force acting on the fluid. In order to accurately describe an MHD flow, the former equations must be properly combined with those of classical electrodynamics [60], which are expressed through Maxwell's equations:

$$\nabla \cdot \boldsymbol{E} = \frac{\rho_e}{\epsilon}, \tag{2.3}$$

$$\nabla \cdot \boldsymbol{B} = 0, \tag{2.4}$$

$$\nabla \times \boldsymbol{E} = -\frac{\partial \boldsymbol{B}}{\partial t}, \tag{2.5}$$

$$\nabla \times \boldsymbol{B} = \mu_0 \boldsymbol{j} + \mu_0 \epsilon \frac{\partial \boldsymbol{E}}{\partial t}, \tag{2.6}$$

where $\boldsymbol{E}$ is the electric field, ρ_e is the electric charge density, ϵ is the permitivity of the material medium, $\boldsymbol{B}$ is the magnetic induction field, μ_0 is the magnetic permeability

of the free space (this is a reasonable approximation for non-magnetizable materials, such as liquid metals [61]) and $\boldsymbol{j}$ is the electric current density. Equation (2.3) is the Gauss' law for the electric field, (2.4) is the Gauss' law for magnetic field, (2.5) is the Faraday's law of induction and (2.6) is the Ampère-Maxwell law. The relevant body force is the Lorentz force, given by the equation

$$\boldsymbol{f} = \rho_e \boldsymbol{E} + \boldsymbol{j} \times \boldsymbol{B}. \tag{2.7}$$

Additionally, the Ohm's law is considered

$$\boldsymbol{j} = \sigma(\boldsymbol{E} + \boldsymbol{u} \times \boldsymbol{B}) + \rho_e \boldsymbol{u}, \tag{2.8}$$

which is a constitutive equation for a conducting medium moving with velocity $\boldsymbol{u}$ with respect to the laboratory frame. The first term in parenthesis in the right-hand side is the effective electric field and the second term is the convection current.

2.2 The MHD approximation

Since electrodynamic equations are relativistic and invariant under Lorentz transformations, and fluid dynamic equations are non-relativistic and invariant under Galilean transformations, an approximation has to be employed, namely, the MHD approximation, to ensure compatibility between the two sets. This approximation can be summarized as follows [61]:

- The fluid velocity is much smaller than the speed of light, that is, flows are non-relativistic $|\boldsymbol{u}| \ll c$.

- Only low-frequency phenomena are considered, that is, only quasi-stationary phenomena are relevant.

- The induced electric fields are of the order of magnitude of the electromotive force (EMF) induced by the fluid motion, $\boldsymbol{E} \sim \boldsymbol{u} \times \boldsymbol{B}$.

With this approximationa the set of governing equations that describe the motion of an electrically conducting, Newtonian, non-magnetizable and incompressible fluid (liquid metal) in the presence of a magnetic field are

$$\nabla \cdot \boldsymbol{u} = 0, \tag{2.9}$$

$$\rho\left(\frac{\partial \boldsymbol{u}}{\partial t} + (\boldsymbol{u} \cdot \nabla)\boldsymbol{u}\right) = -\nabla P + \mu\nabla^2\boldsymbol{u} + \boldsymbol{j} \times \boldsymbol{B}, \tag{2.10}$$

$$\nabla \cdot \boldsymbol{B} = 0, \tag{2.11a} \qquad\qquad \nabla \times \boldsymbol{E} = -\frac{\partial \boldsymbol{B}}{\partial t}, \tag{2.11b}$$

$$\nabla \times \boldsymbol{B} = \mu_0 \boldsymbol{j}, \qquad (2.12a)$$

$$\boldsymbol{j} = \sigma(\boldsymbol{E} + \boldsymbol{u} \times \boldsymbol{B}). \qquad (2.12b)$$

By taking the divergence of Ampère's law (2.12a) yields $\nabla \cdot \boldsymbol{j} = 0$, which is the statement of the conservation of electric charge in this approximation.

In magnetohydrodynamics (MHD) there are different formulations of the fundamental equations, depending on the dependent electromagnetic variables chosen for the description of the flow [62]. The formulations based on the induced magnetic field, B-formulation, and the one based on the electric potential, ϕ-formulation, are the most widely used and are physically equivalent. The main difference between the two formulations lies in the way in which the induced electrical currents are calculated. In the B-formulation they are calculated using Ampère's law (2.12a), while in ϕ-formulation they are calculated using Ohm's law (2.12b). A fundamental characteristic of MHD flows is that, in principle, the magnetic field and the fluid velocity field are coupled, meaning that the magnetic field can modify the fluid velocity and vice versa. However, for liquid metal flows under laboratory or industrial conditions, the magnetic field is practically unaffected by the velocity field. In these cases, the approximation of small magnetic Reynolds number,

$$R_m \ll \frac{UL_c}{\gamma}, \qquad (2.13)$$

is satisfied, where $\gamma = \frac{1}{\mu_o \sigma}$ represents the magnetic diffusivity, μ_o being the permeability of vacuum and L_c a characteristic length. This parameter compares the induced magnetic field with the applied magnetic field [63]. In the approximation $R_m \ll 1$, the induced magnetic field is very small and can be neglected compared to the applied magnetic field [61].

2.2.1 B-formulation

We now present the fundamental MHD equations under the low magnetic Reynolds number approximation using the formulation based on the induced magnetic field (B-formulation) [61]. In this formulation, the dependent (or primitive) variables are the velocity, the pressure and the induced magnetic field. In a dimensionless manner, under the approximation $R_m \ll 1$, the total magnetic field can be expressed as the contribution of two components [63],

$$\boldsymbol{B} = \boldsymbol{B}^0 + R_m \boldsymbol{b}, \qquad (2.14)$$

where the first contribution is due to the applied magnetic field $\boldsymbol{B}^0$, and the second is the induced magnetic field $\boldsymbol{b}$ generated by the fluid flow within the $\boldsymbol{B}^0$ field. This form of the field is a good approximation when R_m is small, as the term $R_m \boldsymbol{b}$ is a small perturbation that slightly modifies the applied field due to fluid motion. Equations that govern the dynamics of a liquid metal flow under a magnetic field in the B-formulation can be expressed in the following dimensionless form

$$\nabla \cdot \boldsymbol{u} = 0, \tag{2.15}$$

$$\frac{\partial \boldsymbol{u}}{\partial t} + (\boldsymbol{u} \cdot \nabla)\,\boldsymbol{u} = -\nabla P + \frac{1}{Re}\nabla^2 \boldsymbol{u} + N(\boldsymbol{j} \times \boldsymbol{B}^0), \tag{2.16}$$

$$\nabla^2 \boldsymbol{b} = (\boldsymbol{u} \cdot \nabla)\boldsymbol{B}^0, \tag{2.17}$$

$$\nabla \times \boldsymbol{b} = \boldsymbol{j}, \tag{2.18}$$

$$\nabla \cdot \boldsymbol{b} = 0, \tag{2.19}$$

where the velocity $\boldsymbol{u}$, pressure P, electric current density $\boldsymbol{j}$, applied magnetic field $\boldsymbol{B}^0$, and induced magnetic field $\boldsymbol{b}$, have been normalized by U, ρU^2, $\sigma U B_{max}$, B_{max}, and $R_m B_{max}$ respectively. Here, U is a characteristic velocity of the flow, and B_{max} is the maximum magnetic field strength of the permanent magnet, while ρ and σ are the mass density and electrical conductivity of the liquid. Coordinates (x, y, z), and time t, are normalized by L_c and L_c/U, respectively. The dimensionless parameters are the Reynolds number, $Re = UL_c/\nu$, the interaction parameter $N = \sigma B_{max}^2 L_c/\rho U$, where ν is the kinematic viscosity. The interaction parameter can also be expressed as $N = Ha^2/Re$, where $Ha = B_{max}L_c\sqrt{\sigma/\rho\nu}$ is the Hartmann number. Equation (2.17), known as the induction equation or the magnetic field transport equation, combines Ohm's law, Faraday's law, and Ampère's law under the approximation $R_m \ll 1$, and describes the transport of the magnetic field. By solving equation (2.17), the induced magnetic field can be determined, which in turn allows the calculation of induced electric currents using Ampère's law (2.18). Equations (2.15) - (2.19) form a comprehensive system that can be solved by providing appropriate boundary and initial conditions, as it is done numerically in Chapter 3.

In addition, the applied magnetic field $\boldsymbol{B}^0$, must satisfy the magnetostatic equations, which guarantees its solenoidal and irrotational character

$$\nabla \cdot \boldsymbol{B}^0 = 0, \qquad \nabla \times \boldsymbol{B}^0 = 0. \tag{2.20}$$

2.2.2 ϕ-formulation

This formulation considers the scalar electric potential as an electromagnetic variable, enabling the fundamental equations of MHD to be expressed in terms of velocity, pressure, and electric potential. Under the approximation $R_m \ll 1$, the total magnetic field is approximately equal to the applied magnetic field $\boldsymbol{B}^0$ as it remains unaffected by fluid motion. Assuming that this field does not vary with time, Faraday's law of induction can be expressed as

$$\nabla \times \boldsymbol{E} = 0, \tag{2.21}$$

thus, the electric field is potential and it can be expressed in the form

$$\boldsymbol{E} = -\nabla\phi, \tag{2.22}$$

where ϕ is the electric potential, normalized by $UB_{max}L_c$.

The complete system of equations in dimensionless terms under this formulation is given by:

$$\nabla \cdot \boldsymbol{u} = 0, \tag{2.23}$$

$$\frac{\partial \boldsymbol{u}}{\partial t} + (\boldsymbol{u} \cdot \nabla)\,\boldsymbol{u} = -\nabla P + \frac{1}{Re}\nabla^2\boldsymbol{u} + N\boldsymbol{j} \times \boldsymbol{B}^0, \tag{2.24}$$

$$\boldsymbol{j} = -\nabla\phi + \boldsymbol{u} \times \boldsymbol{B}^0, \tag{2.25}$$

$$\nabla^2\phi = \nabla \cdot (\boldsymbol{u} \times \boldsymbol{B}^0), \tag{2.26}$$

where dimensionless variables are defined in the same way as with the $B-$formulation. The applied magnetic field must also satisfy the magneto-static equations (2.20). Equations (2.23) - (2.26) form a comprehensive system that can be solved by providing appropriate boundary and initial conditions, as it is done analytically and numerically in Chapter 4 and 5 and numerically in Chapters 5 and 6.

With the ϕ-formulation, electric current density is calculated from Ohm's law (2.25) while the charge conservation, $\nabla \cdot \boldsymbol{j} = 0$, while the Poisson's equation for the electric potential (2.26).

2.2.3 Heat transfer equation

The transport of heat in a liquid metal flow under a magnetic field is governed by the heat transfer equation, namely,

$$\frac{\partial T}{\partial t} + (\boldsymbol{u} \cdot \nabla)\,T = \alpha\nabla^2 T + S, \tag{2.27}$$

where T is the temperature, α is the thermal diffusivity and S represents any source of heat. Due to the MHD phenomena heat sources within the fluid appear in the heat transfer equation due to Joule and viscous dissipations. In dimensionless form is expressed as

$$\frac{\partial T}{\partial t} + (\boldsymbol{u} \cdot \nabla)\,T = \frac{1}{Pe}\nabla^2 T + \frac{Ec\,Ha^2}{Re}\boldsymbol{j}^2 + \frac{Ec}{Re}\Phi, \tag{2.28}$$

where the temperature is normalized as $(T' - T_0)/(T_1 - T_0)$ where T' is the dimensional fluid temperature and T_0 and T_1 are two reference temperatures, for instance, the inlet fluid temperature and the heated wall temperature. The term Φ stands for the viscous dissipation function [59]. Time t is normalized with the diffusive time L_c^2/α, where α is the thermal diffusivity. The dimensionless control

parameters are: the Prandtl number $Pr = \nu/\alpha$, the Péclet number $Pe = UL_c/\alpha$ (which can also be written as $Pe = Pr\,Re$) and the Eckert number $Ec = U^2/C\Delta T$, where C is the specific heat and $\Delta T = T_1 - T_0$ is a characteristic temperature difference. In the present work, Galinstan (GaInSn) alloy is chosen as working fluid whose Prandtl number is $Pr = 0.053$. It has to be mentioned that an important limitation in the heat transfer analysis of the present work, is the absence of natural convection effects which are assumed to be negligible under the explored conditions.

Since the velocity field appears in this equation, it is necessary to first obtain the velocity field in order to solve the heat transfer equation as it is done numerically in Chapters 3, 4, 5 and 6.

2.3 Numerical methodology

In this section, we explain the numerical methodology followed to solve the fundamental MHD equations using Computational Fluid Dynamics based on the Finite Volume Method.

2.3.1 Computational Fluid Dynamics

Computational Fluid Dynamics (CFD) provides the capability to tackle and reproduce real systems based on fluid flows with electromagnetic interaction. CFD presents well-known advantages to reduce costs of new experimental designs due to the possibility of performing wide parametric studies with high reliability, particularly when when laboratory experiments are difficult to perform. Numerically solving these equations involves finding approximate solutions to the governing equations at selected points in the domain. The strategy used in CFD involves replacing a problem defined on a continuous domain with a discrete domain defined by a mesh. For the two-dimensional Cartesian case, a numerical domain can be visualized using a mesh as shown in Figure 2.1, where a structured mesh is used for simplicity, however, it is not always the case. The physical domain is divided into a predetermined number of cells or control volumes of the same size. In this sense, for all $1 \leqslant i \leqslant nx$, $1 \leqslant j \leqslant ny$, $1 \leqslant k \leqslant nz$, and $t_n \geqslant 0$, where nx, ny, and nz represent the number of points in the respective directions.

2.3.2 Finite Volume Method

The governing equations described in the previous section can be solved numerically using the Finite Volume Method (FVM), this is a low-order method that consists of converting a partial differential equation into a system of linear algebraic equations that can be solved using direct or iterative methods to obtain an approximate solution, which involves obtaining a distribution of the dependent variable at specific points in the numerical domain, averaged over small non-overlapping control volumes. The general equation of transport in conservative form is given by:
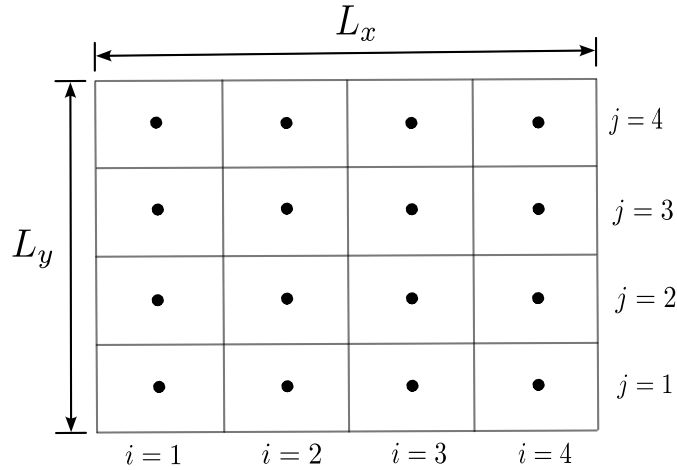
Figure 2.1: Numerical meshing of a two-dimensional domain, i and j are the x and y counters of a structured mesh.

$$\frac{\partial \varphi}{\partial t} + \nabla \cdot (\boldsymbol{u}\varphi) = \nabla \cdot (\Gamma \nabla \varphi) + S, \qquad (2.29)$$

where φ is a generalized dependent variable, Γ is a generalized diffusion coefficient and S represents a source term. Depending on the physical quantity that φ represents, (2.29) can be reduced to the momentum equation (if φ is a velocity component) or the heat transfer equation (if φ is temperature). To solve fluid problems, it is necessary to obtain the velocity field as part of the solution. In the general advection-diffusion equation (2.29), the velocity field is assumed to be known and unaffected by the transported quantity. However, in reality, the velocity field is generally unknown. Therefore, to solve the Navier-Stokes equation (2.30), it is necessary to carefully treat the non-linearity arising from the convective term, since the velocity field is, a priori, unknown. This equation involve determining the velocity components and pressure field as functions of spatial coordinates and time,

$$\frac{\partial \boldsymbol{u}}{\partial t} + (\boldsymbol{u} \cdot \nabla) \, \boldsymbol{u} = -\nabla P + \frac{1}{Re} \nabla^2 \boldsymbol{u} + N \boldsymbol{j} \times \boldsymbol{B}^0. \qquad (2.30)$$

To solve (2.30) using the FVM, the domain is discretized into finite volumes or control volumes, and the fluxes across the cell interfaces are approximated, as shown in Figure 2.2 for a two-dimensional domain. Uppercase letters N, S, E, and W represent the centers of the volumes north, south, east and west, to the central volume P, respectively. Lowercase letters denote the corresponding boundaries of the central volume. The blue and red spots represent the location of the velocity components used to calculate the fluxes entering/leaving the central control volume. In Appendix B the finite Volume discretization as well as the algorithm used for the numerical solution of the governing equations are presented.

In order to find a solution at the selected points (see Figs. 2.1 and 2.2), the governing equations must be converted into its discrete form. This is achieved by aproximating
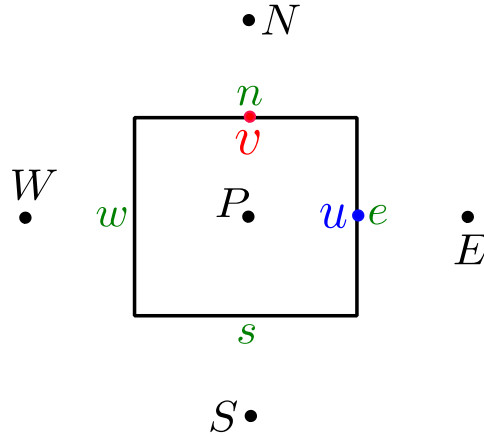
Figure 2.2: Finite volume or control volume for a two-dimensional domain. Upper-case letters N, S, E and W refer to the location of the neighbouring control volumes, according to the cardinal points, of the central volume P. Lower case letters represent the boundaries of the central volume following the same nomenclature.

every term of the general equation by means of discretization schemes, which are briefly described in the next subsection.

Discretization schemes

To ensure the accuracy and stability of the discretization schemes used to solve numerically the governing equations, these must be choosen carefully. For the numerical solution of the MHD governing equations the following discretization schemes are used:

- The Euler discretization method is employed to discretize the temporal term using forward differences due to its computational efficiency. It has a first-order precision.

- Finite difference approximation is employed to estimate derivatives.

- The central scheme is used to calculate the convective term. It is a second-order scheme that provides accurate approximation of the fluxes at the boundaries of the control volumes and considers the same influence of the flow velocities neighbouring a boundary.

- The upwind scheme is applied when the flow is strongly convective. It depends on the direction of the flow, when the flow is from left to right, then the boundaries receive a stronger influence from the control volume on their adjacent left side and viceversa.

Boundary conditions

To solve the system of equations, appropriate and physically meaningful boundary conditions are required. Throughout this work, the following conditions were implemented:

- First-type or Dirichlet boundary condition, which corresponds to a physical situation where the value of the dependent variable, φ, is known at the boundary of the domain.

- Second-type or Neumann boundary condition, which is applied when the value of the derivative, φ', of the dependent variable is known at the boundary.

- Third-type or Robin boundary condition, which is a combination of Dirichlet and Neumann conditions, $\varphi + \varphi' = f$.

In the FVM, the implementation of boundary conditions involves modifying discretized equations of the control volumes adjacent to the domain boundary.

Treatment of numerical difficulties

The systems of governing equations (2.15) - (2.19) and (2.23) - (2.26) present several characteristics that pose challenges when trying to solve it numerically, such as:

- Nonlinearity of the convective term $[(\boldsymbol{u} \cdot \nabla)\, \boldsymbol{u}]$: It is addressed by employing a semi-implicit numerical approximation of the convective term to ensure *numerical stability*.

- Strong coupling between the equations: Which is tackled using an iterative methodology inside the semi-implicit approximation, where the velocity field of the previous time instant is used to compute the current time step iteratively until reaching a physically accurate solution.

- Lack of an equation describing pressure behavior and boundary conditions for pressure: To determine the pressure field, the SIMPLEC method (Semi Implicit Method for Pressure Linked Equations - Corrected) is used for pressure-velocity decoupling, which is a methodology to gradually correct the pressure field by solving transport-like discrete equations iteratively until obtaining a divergence-free velocity field.

Additionally, there is another numerical challenge that requires special attention to ensure that the numerically obtained solutions are physically accurate, which involves using a staggered mesh.

Arrangement of variables in the mesh

When the velocity and pressure are defined at the nodes of a regular control volume, a highly non-uniform pressure distribution can yield a uniform field in the discretized momentum equations, causing the pressure at the central node to vanish. This results in zero gradients at the nodal points, which is known as the "checkerboard effect", and is responsible of the presence of unphysical oscillations in the numerical solution. To address this concern, a staggered grid is employed, where scalar variables are computed at the volume centers and vector variables are calculated at the faces, as depicted in Figure 2.3. In this kind of arrangement, the spatial points at which the components of vector quantities are sought, are staggered half a control volume (dashed red and blue lines) with respect to the center of the scalar control volume (continuous black line). By utilizing a staggered grid system, we prevent the occurrence of the checkerboard effect in the computed pressure that may arise with a regular grid configuration.

The choice of numerical grid has a significant impact on solution accuracy, also the numerical resolution since an appropriate grid configuration allows an accurate representation of physical phenomena. Nevertheless, increasing the grid resolution comes at the expense of higher computational costs.
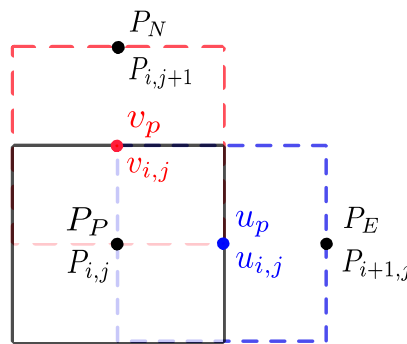

Figure 2.3: Staggered grid arrangement. Vector components are displaced half a control volume (dashed lines) with respect to the control volumes for scalar variables.

On the other hand, both the magnetic field transport equation (2.17) and the Poisson's equation for the electric potential (2.26), as well as the heat transfer equation (2.28), can be treated in the same manner as the general advection-diffusion equation.

Convergence issues

For the solution of the linear system of algebraic equations, the TDMA (TriDiagonal Matrix Algorithm) iterative method is employed. This method was developed with the purpose of optimizing the system solution to converge more quickly, taking advantage of the properties exhibited by the matrices resulting from the finite volume discretization in as structured Cartesian grid, that is,

sparse matrices with only a few non-zero diagonals. These matrices are pentadiagonal for two-dimensional problems and heptadiagonal for three-dimensional problems.

The numerical code is implemented using the FORTRAN 90 programming language implementing a double precision finite volume in-house code. This language is well-suited for scientific computing applications. For details on the implementation of the Finite Volume Method see the book [64].

2.3.3   Applied magnetic field

To reproduce numerically the three-dimensional applied magnetic field, analytical expressions obtained by Furlani [65] that model the magnetic field distribution generated by a rectangular permanent magnet are introduced to the numerical code. Geometry and polarization of the rectangular permanent magnet are shown in Figure 2.4 where a permanent magnet of dimensions l, m and n in the x, y and z coordinates, respectively, is considered. These analytical expresions produces a three-dimensional field with the componentes B_x^0, B_y^0 and B_z^0 as follows:
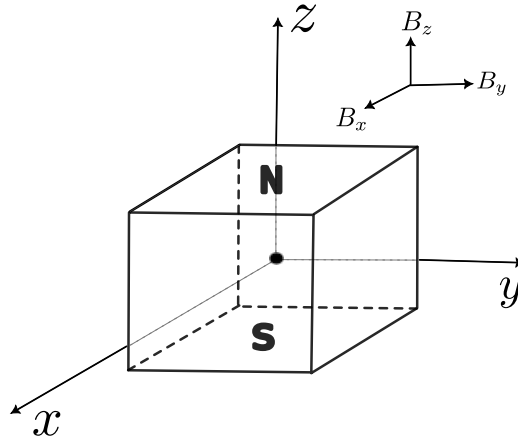

Figure 2.4: Geometry and polarization of the rectangular permanent magnet. Origin of the reference frame is located at the geometric center of the magnet.

The $x-$component of the field is given by

$$B_x^0(x,y,z) = \frac{\mu_o M_s}{4\pi} \Sigma_{k=1}^2 \Sigma_{m=1}^2 (-1)^{k+m} \times \ln\left(F(x,y,z,x_m,y_1,y_2,z_k)\right), \qquad (2.31)$$

where

$$F(x,y,z,x_m,y_1,y_2,z_k) = \frac{(y-y_1) + ((x-x_m)^2 + (y-y_1)^2 + (z-z_k)^2)^{\frac{1}{2}}}{(y-y_2) + ((x-x_m)^2 + (y-y_2)^2 + (z-z_k)^2)^{\frac{1}{2}}}.$$

The $y-$component of the field is given by

$$B_y^0(x,y,z) = \frac{\mu_o M_s}{4\pi} \Sigma_{k=1}^2 \Sigma_{m=1}^2 (-1)^{k+m} \times \ln\left(H(x,y,z,x_1,x_2,y_m,z_k)\right), \qquad (2.32)$$

where

$$H(x, y, z, x_1, x_2, y_m, z_k) = \frac{(x - x_1) + ((x - x_1)^2 + (y - y_m)^2 + (z - z_k)^2)^{\frac{1}{2}}}{(x - x_2) + ((x - x_2)^2 + (y - y_m)^2 + (z - z_k)^2)^{\frac{1}{2}}}.$$

The $z-$component of the field is given by

$$
\begin{aligned}
B_z^0(x, y, z) = \frac{\mu_o M_s}{4\pi} &\Sigma_{k=1}^2 \Sigma_{n=1}^2 \Sigma_{m=1}^2 (-1)^{k+n+m} \times \\
&\tan^{-1}\left(\frac{(x - x_n)(y - y_m)}{(z - z_k)} g(x, y, z, x_n, y_m, z_k)\right),
\end{aligned}
\tag{2.33}
$$

where

$$g(x, y, z, x_n, y_m, z_k) = \frac{1}{((x - x_n)^2 + (y - y_m)^2 + (z - z_k)^2)^{\frac{1}{2}}},$$

and $\mu_0 = 4\pi \times 10^{-7}$ Tm/A is the magnetic permeability of vacuum and M_s is the magnetization parameter of the magnet, given in A/m. Subindices k, m, n, are used to indicate the initial (x_1, y_1, z_1) and final (x_2, y_2, z_2) coordinates in the Cartesian reference frame. These analytical expresions have been validated [66] and compared to experimental measurements [67] obtaining an accurate agreement.

2.3.4   Lorentz force implementation

The calculation of the source term, represented by the Lorentz force in the Navier-Stokes equation, is explained using the ϕ-formulation for three-dimensions, followed by the B-formulation simplified to two-dimensions. The Lorentz force is computed based on

$$\boldsymbol{F} = \boldsymbol{j} \times \boldsymbol{B}^0 = (-\nabla\phi + \boldsymbol{u} \times \boldsymbol{B}^0) \times \boldsymbol{B}^0, \tag{2.34}$$

which can be cast into two terms, $\boldsymbol{B}^0 \times \nabla\phi$ and $\boldsymbol{B}^{0^2}\boldsymbol{u}_\perp$, where $\boldsymbol{u}_\perp$ represents the velocity component perpendicular to the applied magnetic field direction. These two parts can be computed in different positions of the control volume and result in different schemes depending on whether a conservative or non-conservative formula is used [68], [69]. In the computational grid, pressure (P), and electrical potential (ϕ) are located at the center of the control volume since they are scalar quantities, while the velocity components are located at the center of the cell boundaries, according to the staggered arrangement, as shown in Figure 2.5.

To include the Lorentz force in the numerical code, the source term is integrated within a control volume as follows

$$\int_{\Delta V} \boldsymbol{j} \times \boldsymbol{B}^0 \, dV \approx \boldsymbol{j} \times \boldsymbol{B}^0 \, \Delta V. \tag{2.35}$$

where ΔV is the control volume defined as $\Delta V = \delta x \, \delta y \, \delta z$. Considering the three-dimensional componentes of the electric current density flow and the magnetic field
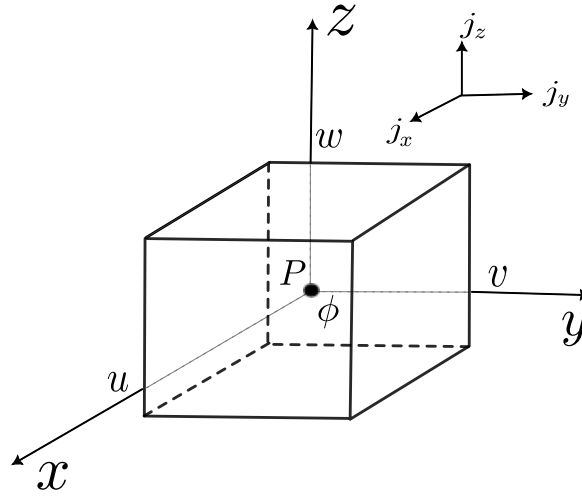
Figure 2.5: Spatial location of scalar quantities and vector components for a staggered arrangement.

as $\boldsymbol{j} = (j_x, j_y, j_z)$ and $\boldsymbol{B}^0 = (B_x^0, B_y^0, B_z^0)$, respectively, detailed expressions are provided for their numerical calculation.

$$\boldsymbol{j} \times \boldsymbol{B}^0 = (j_y B_z^0 - j_z B_y^0)\hat{\imath} + (j_z B_x^0 - j_x B_z^0)\hat{\jmath} + (j_x B_y^0 - j_y B_x^0)\hat{k}. \tag{2.36}$$

The Lorentz force is computed at a cell center by performing the cross product operation with the magnetic field as

$$(F_x)_{i,j,k} = (j_y)_{i,j,k}(B_z^0)_{i,j,k} - (j_z)_{i,j,k}(B_y^0)_{i,j,k},$$
$$(F_y)_{i,j,k} = (j_z)_{i,j,k}(B_x^0)_{i,j,k} - (j_x)_{i,j,k}(B_z^0)_{i,j,k},$$
$$(F_z)_{i,j,k} = (j_x)_{i,j,k}(B_y^0)_{i,j,k} - (j_y)_{i,j,k}(B_x^0)_{i,j,k},$$

in this context, i, j, and k are counters that provide information about the position of the control volume in the structured grid, representing the three spatial directions. For the Lorentz force, the electric current density used is calculated using Ohm's law, based on the velocity at the cell center and using a conservative interpolation

$$(j_x)_{i,j,k} = (v_c)_{i,j,k}(B_z^0)_{i,j,k} - (w_c)_{i,j,k}(B_y^0)_{i,j,k} - \frac{(\phi)_{i+1,j,k} - (\phi)_{i-1,j,k}}{2\delta x}, \tag{2.37}$$

$$(j_y)_{i,j,k} = (w_c)_{i,j,k}(B_x^0)_{i,j,k} - (u_c)_{i,j,k}(B_z^0)_{i,j,k} - \frac{(\phi)_{i,j+1,k} - (\phi)_{i,j-1,k}}{2\delta y}, \tag{2.38}$$

$$(j_z)_{i,j,k} = (u_c)_{i,j,k}(B_y^0)_{i,j,k} - (v_c)_{i,j,k}(B_x^0)_{i,j,k} - \frac{(\phi)_{i,j,k+1} - (\phi)_{i,j,k-1}}{2\delta z}. \tag{2.39}$$

The resulting expression of the source term is a function of the electric potential ϕ, the velocity field $\boldsymbol{u}$, and the magnetic field $\boldsymbol{B}^0$. Given that the electric potential is needed at the cell center and the neighbor control volume center to accurately calculate the induced electric current on the cell face, based on the Gauss' rule

$$(\nabla\phi)_P = \frac{1}{\Delta V} \sum_{f=1}^{nf} \phi_f s_f \boldsymbol{n}_f, \tag{2.40}$$

where the cell face is denoted as f, the number of cell faces is n_f, the area of a cell face is s_f and $\boldsymbol{n}_f$ is the outward normal unit vector direction that requires that there is continuity of the electric field in its normal component on the faces of the control volumes. This process allows us to calculate electric currents on the cell faces (Figure 2.6) using a consistent scheme, to incorporate potential gradients into each velocity component, either u, v, or w. Six points of the electric potential are interpolated to obtain its derivative, as demonstrated for $\partial\phi/\partial z$ at the u component of the velocity

$$
\left(\frac{\partial\phi}{\partial z}\right)_{i+\frac{1}{2},j,k} = \frac{1}{4}\left((\phi)_{i,j,k} + (\phi)_{i+1,j,k} + (\phi)_{i,j,k+1} + (\phi)_{i+1,j,k+1}\right)
$$
$$
-\frac{1}{4}\left((\phi)_{i,j,k} + (\phi)_{i+1,j,k} + (\phi)_{i,j,k-1} + (\phi)_{i+1,j,k-1}\right). \quad (2.41)
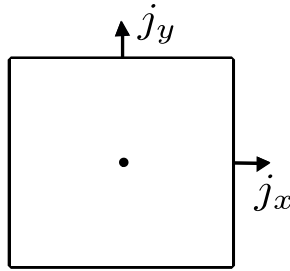$$

Figure 2.6: Location of the electric current density in a plane.

The other derivatives are incorporated in a similar way. Additionally, to perform the magnetic field operations with velocity or electric potential, products at center cells are interpolated to obtain the products at the corresponding cell face depending on the velocity component u, v, w considered.

Using the B-formulation, the Lorentz force is calculated by determining the induced electric currents through Ampère's law (2.18). This approach simplifies the process as the equation for the induced magnetic field is solved. In two dimensions, the Lorentz force is given by

$$
\boldsymbol{j} \times \boldsymbol{B}^0 = (j_y B_z^0)\hat{\imath} - (j_x B_z^0)\hat{\jmath}. \quad (2.42)
$$

The Lorentz force is computed at a cell center by performing the cross product operation with the magnetic field as

$$
(F_x)_{i,j} = (j_y)_{i,j}(B_z^0)_{i,j},
$$
$$
(F_y)_{i,j} = -(j_x)_{i,j}(B_z^0)_{i,j}.
$$

Explicit expressions for electric current components at cell faces are calculated as

$$(j_x)_{i,j+\frac{1}{2}} = \left(\frac{\partial b}{\partial y}\right)_{i,j+\frac{1}{2}}, \qquad (j_y)_{i+\frac{1}{2},j} = -\left(\frac{\partial b}{\partial x}\right)_{i+\frac{1}{2},j}, \qquad (2.43)$$

where b is the z-component of the induced magnetic field. To incorporate it into each velocity component, either u or v, in the numerical code, two points of the induced magnetic field are interpolated to obtain the derivatives required to calculate induced electric currents on the cell faces, in such a way that the expresion is conservative and consistent with respect to the current density

$$\left(\frac{\partial b}{\partial x}\right)_{i+\frac{1}{2},j} = \frac{1}{\delta x}\left((b)_{i+1,j,k} - (b)_{i,j,k}\right), \qquad (2.44)$$

$$\frac{\partial b}{\partial y} = \frac{1}{\delta y}\left((b)_{i,j+1} - (b)_{i,j}\right). \qquad (2.45)$$

We have shown the procedure in this manner since a fully three-dimensional numerical code was used in this study, employing the $\phi-$formulation for the development of the problems presented in Chapters 4, 5, and 6. On the other hand, in Chapter 3, a two-dimensional approximation was employed with the $B-$formulation for solving the numerical problem.

Parametric study of dynamics and heat transfer in a 2D MHD duct flow

In this chapter[‡], we begin the analysis of the liquid metal flow and heat transfer under a localized magnetic field considering a simplified situation, namely, a flow in a two-dimensional duct exposed to the field of a small magnet located close to a conducting wall whose temperature is higher than that of the fluid at the inlet. With the aim of exploring a broad range of parameters where a transition among a variety of flow patterns created by the localized magnetic field is displayed, we restricted the attention to the laminar bulk flow exterior to the Hartmann and viscous layers approximating it as two-dimensional, and analyse its influence on the heat transfer on the heated sidewall. In addition, the effect of the magnet-wall separation from the heated wall which is assumed to be electrically conducting is considered. Although the approach used in this chapter is limited, it offers a first approximation to the description of the dynamic and heat transfer effects of localized magnetic fields in liquid metal duct flows.

3.1 Description of the problem

We analyse numerically the flow and heat transfer of a viscous, incompressible, electrically conducting fluid in a rectangular duct under the field produced by a rectangular permanent magnet located underneath the duct and close to a heated side wall, as shown in Figure 3.1. Due to the heat transfer effect of the localized magnetic field on the liquid metal flow we named this configuration a magnetic fin, in analogy with the extended surfaces or fins used in heat exchangers for heat transfer enhancement purposes. Since Hartmann and viscous layers near horizontal walls have a minor influence on the heat transfer and the largest temperature gradients are in the transversal direction to the heated sidewall, we approximate the flow as two-dimensional to focus the attention on the effect of the laminar bulk flow on the heat transfer. In dimensionless units, the sides of the rectangular magnet are $M_x = 1$ and $M_y = 2$. Considering the side length of the magnet in the x-direction as the characteristic length L_c, the duct length is L_x=50 and the distance between side walls is L_y=14.

[‡]This chapter is mainly based on the paper : Solano-Olivares, V., Cuevas, S. and Figueroa, A. Magnetic fin for heat transfer enhancement in liquid metal duct flow. Magnetohydrodynamics, 58(4), 379-387, 2022. DOI: 10.22364/mhd.58.4.1
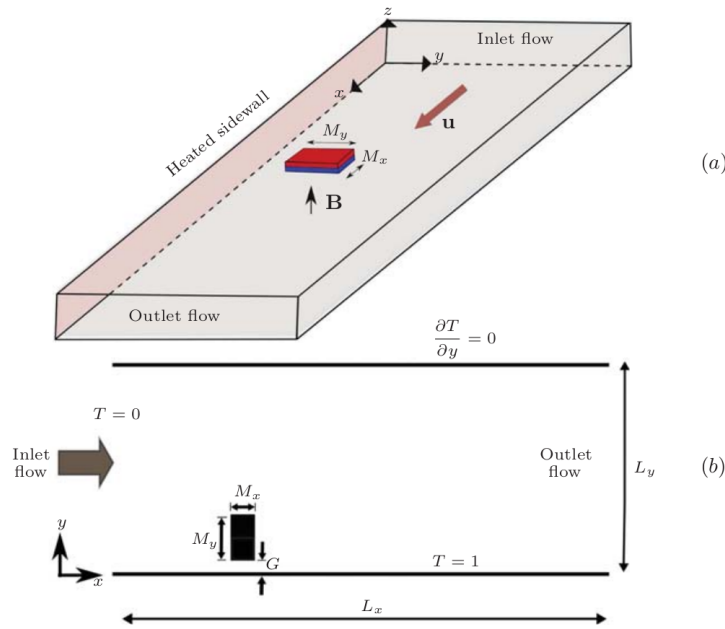
Figure 3.1: Sketch of the analysed flow region.

The side wall at $y = 0$ (the heated wall) is set at a uniform temperature that is higher than the fluid inlet temperature. This wall is assumed to be of perfect electrical conductivity while the opposing wall at $y = L_y$ is electrically insulating and adiabatic. The separation distance between the magnet and the heated wall is G. We carry out this study for a fixed blockage ratio $\beta = M_y/L_y = 1/7$, and different the gap ratios, $h = G/M_y$, in the range $0.05 < h < 0.45$, while the location of the magnet in the x coordinate remains fixed at $x = 12$. The field distribution of the permanent magnet was modeled using analytical expressions provided by Furlani [65].

Initial and boundary conditions

For this problem, the $B-$formulation was used, therefore, the equations (2.15)-(2.19) are solved numerically. For the applied magnetic field, only the B_z^0 component transversal to the flow is considered. To solve numerically the equations initial and boundary conditions are needed.

The boundary conditions used for the numerical solution of the problem are the following. At the entrance of the duct, a constant and uniform flow, $u = 1$, and temperature, $T = 0$, are imposed. At the outlet of the duct, the streamwise gradient of velocity and temperature are set to zero to satisfy fully developed conditions. At the duct walls, the no-slip condition for the velocity is applied, while the side wall at $y = L_y$ has a zero normal temperature gradient at the surface (thermally insulating wall),

$$\frac{\partial T}{\partial y} = 0, \tag{3.1}$$

and at the opposite side wall $y = 0$ (heated wall) a constant temperature $T = 1$ is

fixed. The heated wall is assumed to be perfectly conducting. Mathematically, the dimensionless condition for the induced magnetic field at the fluid-wall interface in a thin conducting wall, according to [6] is written as

$$\frac{\partial b}{\partial n} - \frac{1}{c}b = 0, \tag{3.2}$$

where c is the wall conductance ratio defined as $c = \sigma_w t_w/(\sigma L_c)$ where σ_w and σ are the electric conductivity of the wall and fluid, respectively, t_w is the thickness of the wall and L_c is the characteristic length of the flow. Since the heated wall at y=0 is assumed to be a perfectly conducting wall, $\sigma_w = \infty$, the induced magnetic field mus satisfy the condition

$$\frac{\partial b}{\partial n} = 0, \tag{3.3}$$

whereas for an insulating wall at $y = L_y$, $\sigma_w = 0$, and condition (3.2) becomes $b = 0$.

The solution of the governing equations is performed numerically using the Finite Volume Method 2.3.1. A high-resolution uniform mesh of 900×700 nodes with $\Delta x = 0.05$ and $\Delta y = 0.02$ was used, while time step was of the order 10^{-3}.
A study of mesh independence was performed through the calculation of the frequency of the vortex shedding. The validation of the code, written for the solution of the MHD flow and heat transfer problem, was performed by comparing obtained numerical results against published results under a localized magnetic field and against analytical solutions [66].

3.2   Flow dynamics

To appreciate the effect of placing a localized magnetic field near to the high temperature wall the vorticity map (ω_z) is shown in Fig. 3.2 on the $x - y$ plane at time $t = 600$ for $Re = 1000$ and three different Ha numbers, namely, $Ha = 50$ (which corresponds to $N = 2.5$, Figure 3.2(a)), $Ha = 100$ ($N = 10$, Figure 3.2(b)) and $Ha = 250$ ($N = 62$, Figure 3.2(c)). Additionally, a zoom of the region around the magnetic fin is also shown with streamlines, where a strong modification of the upstream flow due to its presence close to the sidewall can be clearly observed. In this flow, there are two sources of vorticity, first owing to the presence of the walls and second due to the presence of the magnetic obstacle. It is observed that for $N = 2.5$, although the effect of the localized field on the flow close to the heated wall is clear, there are no formation of vortices. In turn, if the interaction parameter increases to N=10, vortex formation and detachment appears. When this parameter takes the value of $N = 62$, the strength of the coupling between the electromagnetic and inertial forces is enough to produce a wake downstream the high magnetic intensity region with periodic vortex detachment that produces stirring close to the hot wall.

(a) $Ha = 50, N = 2.5$.
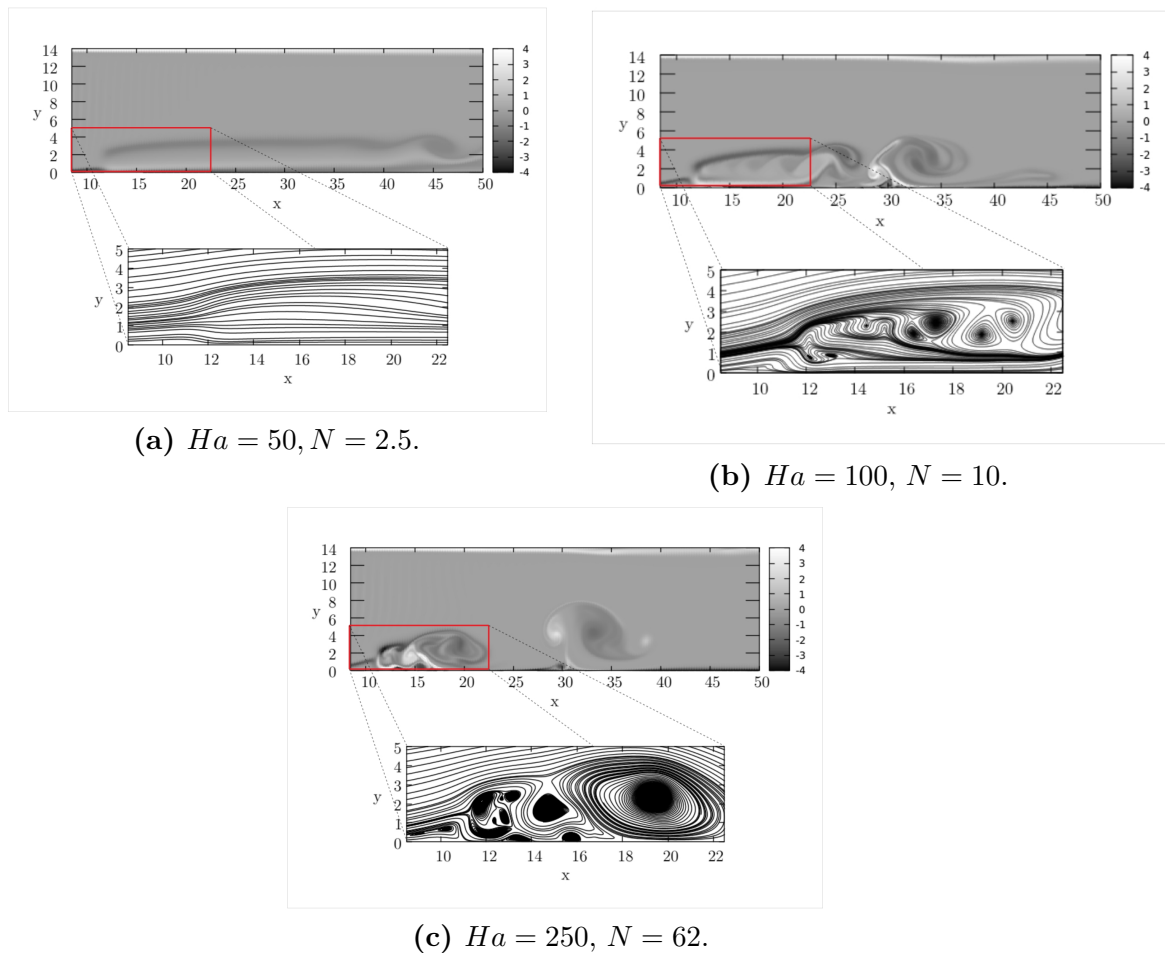
(b) $Ha = 100, N = 10$.

(c) $Ha = 250, N = 62$.

Figure 3.2: Vorticity map and streamlines at $t = 600$ for $Re = 1000$ and different Hartmann numbers (or equivalently different interaction parameters). For each case, the upper figure is the instantaneous vorticity map and the lower figure corresponds to the instantaneous streamlines in the enlarged region marked by the red rectangle.
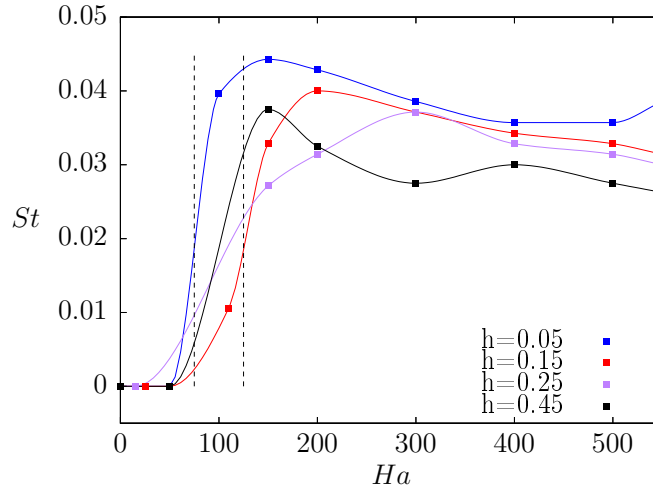
Figure 3.3: Strouhal number St as a function of the Hartmann number Ha for different values of gap ratio h and $Re = 1000$.

The dimensionless frequency of the vortex shedding can be observed in Figure 3.3, where the Strouhal number $St = fL_c/U$ is plotted as a function of the Hartmann number for $Re = 1000$ and several gap ratios, h. It is observed that for small Ha numbers, $Ha < 75$, there is no vortex shedding, while a transition occurs over the range between dotted lines, and the onset of vortex shedding appears at $Ha \approx 150$. Depending on the gap ratio h, the Strouhal number reaches a maximum. As it will be discussed later, the onset of the vortex shedding has a direct consequence on the heat transfer.

3.3 Heat transfer analysis

Figure 3.4 shows, through snapshots, the effect of the magnetic fin on the temperature field for two cases, namely, (a,b) $Re = 1000$, $N = 5.6$, and (c,d) $Re = 1000$, $N = 84.1$. These snapshots show the instantaneous changes produced by electromagnetic stirring, particularly, how the thermal boundary layer on the sidewall is disrupted by the presence of the magnetic fin. Notice that the greater agitation is observed in case (c,d) where the interaction parameter is larger, leading to more widespread detached vortices. For the smaller value $N = 5.6$, cross-stream temperature gradients are reduced which means a less intense heat flow through the wall. To investigate this in more detail, the heat transfer enhancement is evaluated through the global Nusselt number

$$Nu = \frac{1}{L_x} \int_0^{L_x} \overline{Nu_x}(x)dx, \tag{3.4}$$

computed by integrating over time the local Nusselt number

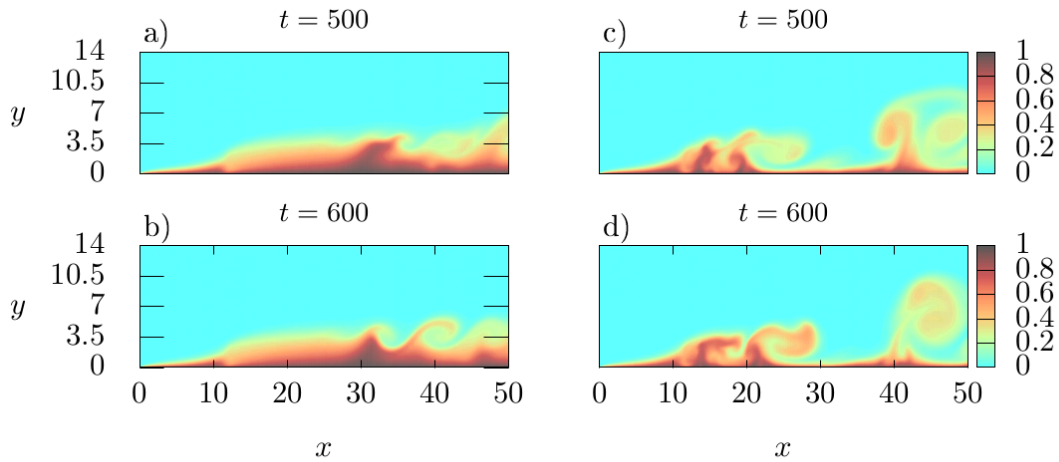$$Nu_x(x,t) = \frac{\partial T}{\partial y}\bigg|_w \frac{L_y}{T_b - T_w}, \tag{3.5}$$

Figure 3.4: Temperature field at two time instants. (a,b) $Re = 1000$, $N = 5.6$ and (c,d) $Re = 1000$, $N = 84.1$.

along the hot wall, being T_w and T_b the wall and bulk temperatures, the latter defined as

$$T_b(x,t) = \int_0^{L_y} uT \ dy / \int_0^{L_y} u \ dy. \tag{3.6}$$

First, the local Nusselt number Nu_x is computed for $Re = 1000$ for a purely hydrodynamic flow, that is, in absence of a localized magnetic field, and for a magnetohydrodynamic flow with $Re = 1000$ and $Ha = 100$ ($N = 10$). Figure 3.5 shows the Nu_x as a function of x coordinate for both hydrodynamics and MHD cases in order to appreciate the effect that each flow has on the heat transfer; for the purely hydrodynamic case a decreasing is observed while for the MHD case the local Nusselt numbers shows an irregular behavior, increasing and decreasing along the heated wall. Notice that at certain location Nu_x reaches values much higher that with the hydrodynamic flow, indicating the presence of stirring that improves the convective heat transfer considerably. This clearly shows the effect of the vortex flow pattern in the heat transfer.

Three Reynolds numbers were explored, namely, $Re = 500, 1000$ and 1500, and the Hartmann number was varied in the range $0 \leq Ha \leq 550$, while the effect of the location of the magnet with respect to the heated wall was examined by considering different values of the gap ratio, h, namely, $h = 0.05, 0.15, 0.25, 0.45$. Figure 3.6 shows the global Nusselt number as a function of the interaction parameter for different Reynolds numbers and a fixed $h = 0.25$ value. It is observed that for the different Re values, the maximum Nu is obtained for the same critical interaction parameter, namely, $N \approx 105$. This means that the optimum Nu value is obtained for the same ratio of Lorentz to inertia forces. Moreover, the presence of the magnetic fin produces a local pressure drop due to the braking of the flow caused by the Lorentz force. Figure 3.7 shows the local pressure drop calculated upstream and downstream the magnetic fin as a function of Ha for different values of h. Notice that a maximum is reached for $Ha = 100$ for all h values and that it increases as h
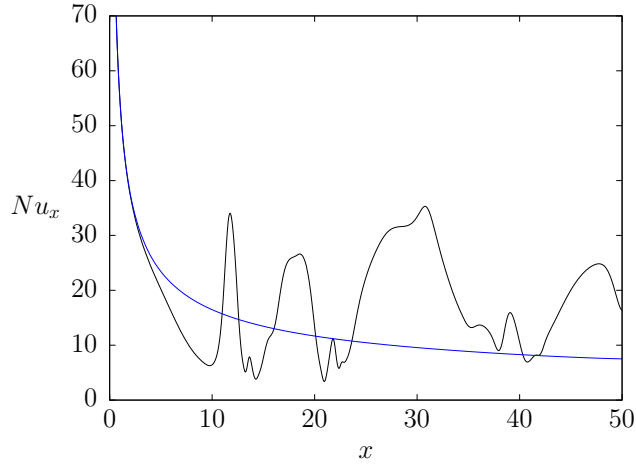
Figure 3.5: Instant local Nusselt number along the hot wall is computed for $Pe = 53$, $Ha = 100$ ($N = 10$) at $t = 400$.

increases.

As is usually done with mechanical swirl flow devices, the thermal performance factor, η, defined as [52]

$$\eta = \frac{Nu/Nu_0}{(f_c/f_0)^{1/3}},\tag{3.7}$$

can be used to evaluate the performance of the magnetic fin, where Nu_0 is the Nusselt number of the purely hydrodynamic flow, while f_c and f_0 are the friction factors with and without magnetic fin. A device with a good performance is able to reach a significant increase of heat transfer coefficient (i.e. Nu) with minimum increase of friction factor. The latter is calculated from the global pressure drop across the test section due to the interaction between the fluid and the duct with inserts (a magnetic fin in this case). It was found that due to the location of the magnet and its size relative to the with of the duct, the friction factor remains practically unchanged with or without magnetic fin. Figure 3.8 displays η and the percentage increment of overall heat transfer, $HI = \langle (Nu - Nu_0)/Nu_0 \rangle \times 100\%$, as a function of Ha for $Re = 1000$ and different h values. It is observed that for $Ha < 100$ the performance of the magnetic fin is in general worse than the purely hydrodynamic flow for all values of h. This corresponds to negative percentage values of HI. Notice from Figure 3.3 that in this region of Ha values vortex shedding has not started yet, that is, $St = 0$. As Ha increases ($Ha > 100$), η rises and reaches a maximum value for each value of h. It was found that, for $Re = 1000$, optimal conditions that maximize η occur when $h = 0.15$ and $Ha = 290$. In terms of HI, this corresponds to a maximum percentage increment 43.2% compared to the purely hydrodynamic case. This behavior may be explained by contrasting the inertial and Lorentz forces. For a given Re, when Ha is small inertia overcomes the Lorentz force so that the braking of the flow is not strong enough to produce vortex shedding and boundary layer detachment, therefore, the heat transfer from the hot wall is reduced. As Ha grows, the opposing Lorentz force increases and may become comparable with inertia or even much larger. In this case, vortex shedding is produced by the magnetic fin,
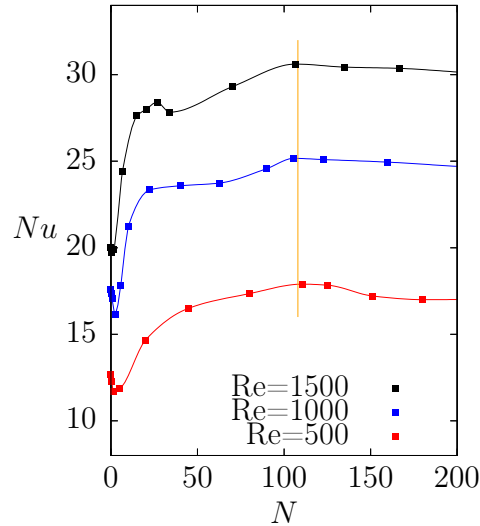
Figure 3.6: Nusselt number, Nu, as a function of the interaction parameter N for $Re = 500, 1000$ and 1500, the of gap ratio is $h = 0.25$.

promoting an efficient stirring near the heated wall and enhancing the heat transfer.

3.4 Conclusions

Assuming a two-dimensional approximation, a numerical heat transfer characterization of the performance of a magnetic fin in a liquid metal duct flow was carried out in a wide range of Hartmann numbers for three fixed Reynolds numbers. Although this approximation strongly limits the scope of our approach, it retains some important physical features of the flow. When the coupling between electromagnetic and inertial forces is strong enough, vortex shedding arises producing an intense stirring that increases the heat transfer from the heated wall. For the Re values explored, the global Nusselt number Nu presents a maximum for $N \approx 105$, what means that optimal heat transfer is obtained for the same ratio of Lorentz to inertial forces. As the blockage ratio is small ($\beta = 1/7$), the friction factor remains practically unchanged with or without magnetic fin, thus, the trend of the global thermal performance, η, and the percentage increment of heat transfer, HI, as functions of the Hartmann number Ha are similar. For $Re = 1000$, an optimal global performance $\eta = 1.43$ or a maximum percentage of heat transfer improvement of 43% compared to the purely hydrodynamic case, were obtained for a given ratio $h = 0.15$ and $Ha = 290$. Therefore, magnetic fins appear to be a suitable non-intrusive method to enhance heat transfer in liquid metal duct flows and deserve to be studied in more realistic situations. This will be done in Chapters 5 and 6 where three-dimensional numerical simulations are carried on.
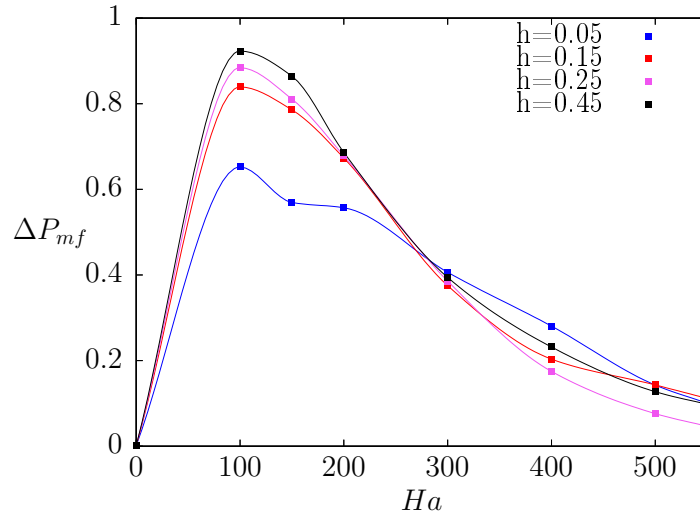
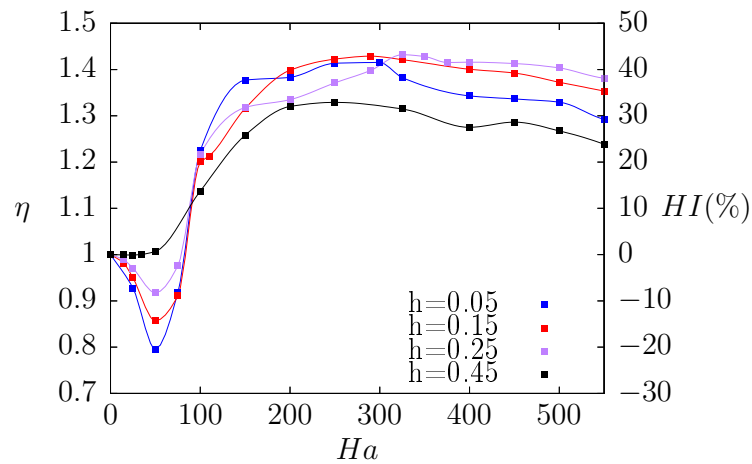Figure 3.7: Local pressure drop ΔP_{mf} as a function of the Hartmann number Ha and $Re = 1000$.

Figure 3.8: Global thermal performance, η, percentage increment of heat transfer, HI, as a function of Ha at different gap ratios, h, and $Re = 1000$.

Exact and numerical solution of MHD flows in a rectangular duct under a uniform magnetic field

In this chapter[‡], we analyze steady, fully developed magnetohydrodynamic (MHD) flows in ducts with rectangular cross-section under a uniform transversal magnetic field with the aim to validate the developed code by comparing their numerical solutions with exact analytical solutions. In the literature, there exist analytical solutions of MHD flows in a rectangular duct [5, 6], under a uniform magnetic field using the $B-$formulation (based on the induced magnetic field). However, to extend the validation of the numerical code, we present new alternative exact analytical obtained using a different formulation, namely, the $\phi-$formulation (based on the electrical potential). To the best of our knowledge these solutions have not been reported in the existing literature. Non-dimensionalized solutions for both formulations are compared, demonstrating their complete equivalence.

Although the code developed in this work is intended to simulate three-dimensional liquid metal flows in ducts under non-homogeneous magnetic fields, we first address MHD duct flows in simplified cases where the existence of exact analytical solutions allow to ensure the satisfactory performance of the code by comparing the numerical solutions in this limits. The comparison involves to reach the fully developed flow in the numerical three-dimensional solution so that the velocity profiles as a function of the transversal y and z coordinates can be compared with the two-dimensional analytical solution in the cross-section plane of the duct. We explore three different cases based on the chosen electrically boundary conditions: CASE 1 corresponds to a duct with perfect electrically conducting walls; CASE 2 corresponds to a duct with electrically insulating walls, and finally; CASE 3 corresponds to a combination of perfectly conducting and insulating walls. For each case, we first present the analytical solution and then the corresponding numerical solution.

[‡]Part of the content of this chapter is mainly based on the paper: Solano-Olivares, V., Cuevas, S., & Figueroa, A. (2020). Liquid metal MHD flow and heat transfer in a rectangular duct with perfectly conducting walls perpendicular to the applied magnetic field. Suplemento de la Revista Mexicana de Física, 1(2), 38-44. DOI: 10.31349/SuplRevMexFis.1.2.38

4.1   CASE 1:   Duct   with   perfectly   conducting walls

First, let us consider the case where all four duct walls that contain the flow are perfectly conducting. The physical model is illustrated in Figure 4.1, where liquid metal flows in the x-direction through a duct of uniform rectangular cross-section duct under a uniform magnetic field applied in the y-direction. For the sake of simplicity, in the exact solution we chose to set the coordinate origin at the center of the duct as shown in Figure 4.2, instead of the lower left corner of the duct, as is done for the numerical solution.
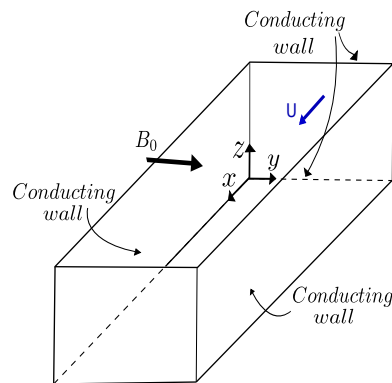

Figure 4.1: Sketch of the configuration considered for the numerical simulation of the case 1: Duct with perfectly conducting walls.
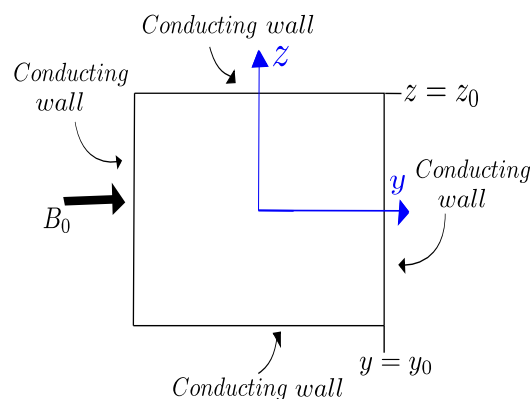

Figure 4.2: Scheme of the cross-section of the duct considered for the analytical solution of the case 1: Duct with perfectly conducting walls.

4.1.1 Analytical solution with B-formulation

We now present an exact analytical solution obtained by assuming a steady, fully developed flow of a viscous, incompressible, and electrically conducting fluid with constant thermophysical properties in a duct with perfectly conducting walls. Under these assumptions, the governing dimensionless equations were reduced to the following set of equations using the $B-$formulation

$$\frac{\partial^2 u}{\partial y^2} + \frac{\partial^2 u}{\partial z^2} + Ha^2 \frac{\partial b}{\partial y} = \frac{dP}{dx}, \tag{4.1}$$

$$\frac{\partial^2 b}{\partial y^2} + \frac{\partial^2 b}{\partial z^2} + \frac{\partial u}{\partial y} = 0, \tag{4.2}$$

where u es the velocity component in the $x-$direction and the induced magnetic field in the same direction is represented by b. For the $B-$formulation, specific boundary conditions must be satisfied. These conditions include the no-slip condition for the velocity at the solid walls and the condition for the induced field that ensures that the derivative of the induced magnetic field with respect to the coordinate normal to the wall is zero [5, 6], that is,

$$u(\pm y_0) = 0, \qquad u(\pm z_0) = 0, \tag{4.3}$$

$$\frac{\partial b}{\partial y}(y, \pm z_0) = 0, \qquad \frac{\partial b}{\partial z}(\pm y_0, z) = 0. \tag{4.4}$$

The exact solution which corresponds to such a case is obtained in a similar way to Hughes & Young [5] when $y_0 = 1$. Therefore, a solution with the following form is proposed

$$u(y, z) = u_p + \sum_{n=0}^{\infty} u_n(z) \cos(\lambda_n y), \tag{4.5}$$

$$b(y, z) = b_p + \sum_{n=0}^{\infty} H_n(z) \sin(\lambda_n y), \tag{4.6}$$

where

$$\lambda_n = (2n + 1)\frac{\pi}{2}. \tag{4.7}$$

For this particular solution, u_p and b_p are the particular solutions when the walls located at $(+z_0, -z_0)$ are located sufficiently far from the mid-central plane, yielding a flow between two perfectly conducting plates of infinite length. Thus, the velocity field is given by

$$u(y, z) = \frac{dP}{dx} \left\{ \frac{\cosh(Hay) - \cosh(Ha)}{Ha^2 \cosh(Ha)} + 2 \sum_{n=0}^{\infty} \frac{(-1)^n \alpha_n(z) \cos(\alpha_n y)}{\lambda_n (Ha^2 + \lambda_n^2) \Delta n} \right\}, \tag{4.8}$$

where

$$\Delta n = \frac{1}{2}(-s_n \sin(2s_n z_0) + r_n \sinh(2r_n z_0)), \tag{4.9}$$

$$\alpha_n(z) = \gamma_n \sinh(r_n z) \sin(s_n z) + \delta_n \cosh(r_n z) \cos(s_n z), \tag{4.10}$$

$$\gamma_n = r_n \cosh(r_n z_0) \sin(s_n z_0) + s_n \sinh(r_n z_0) \cos(s_n z_0), \tag{4.11}$$

$$\delta_n = r_n \sinh(r_n z_0) \cos(s_n z_0) - s_n \cosh(r_n z_0) \sin(s_n z_0), \tag{4.12}$$

$$r_n = \sqrt{\frac{\lambda_n}{2}} \sqrt{\sqrt{Ha^2 + \lambda_n^2} + \lambda_n}, \qquad s_n = \sqrt{\frac{\lambda_n}{2}} \sqrt{\sqrt{Ha^2 + \lambda_n^2} - \lambda_n}, \tag{4.13}$$

whereas the solution for the induced magnetic field is as follows

$$b(y,z) = \frac{dP}{dx} \left\{ \frac{Ha^2 y \cosh(Ha) - \sinh(Hay)}{Ha^2 \cosh(Ha)} + 2\sum_{n=0}^{\infty} \frac{(-1)^n \beta_n(z) \sin(\lambda_n y)}{\lambda_n (Ha^2 + \lambda_n^2)\Delta n} \right\}, \tag{4.14}$$

where

$$\beta_n(z) = \delta_n \sinh(r_n z) \sin(s_n z) + \gamma_n \cosh(r_n z) \cos(s_n z). \tag{4.15}$$

For the analytical solution the dimensions considered are $y_0 = z_0 = 1$, and the pressure gradient is obtained as

$$\frac{dP}{dx} = \frac{4}{\int_{-1}^{1} \int_{-1}^{1} \left(\frac{\cosh(Hay) - \cosh(Ha)}{Ha^2 \cosh(Ha)} + 2\sum_{n=0}^{\infty} \frac{(-1)^n \alpha_n(z) \cos(\alpha_n y)}{\lambda_n (Ha^2 + \lambda_n^2)\Delta n} \right) dy dz}. \tag{4.16}$$

4.1.2 Numerical solution with ϕ-formulation

As it was mentioned in Section 2.2.2, in a 3D problem, ϕ-formulation allows us to solve a scalar equation for the electric potential, which enables us to calculate the induced electric current. On the other hand, the $B-$formulation requires solving a vector equation for the induced magnetic field in order to obtain the induced electric current through Ampère's law. For the sake of simplicity, to compare with the analytical solution we develop the three-dimensional numerical solution based in the Finite Volume method using the $\phi-$formulation. Boundary conditions are the following: at the entrance of the duct, a constant and uniform flow, $u = 1$ is imposed. At the outlet of the duct, the streamwise gradient of velocity is set to zero in order to satisfy fully developed conditions. At the duct walls, the no-slip condition for the velocity is applied. As solid walls are assumed to be perfectly conducting, the dimensionless boundary condition for the electric potential at the fluid-wall interface according to [6] is written as $\phi = 0$, which indicates that there are no variations in the electric field given

that $\boldsymbol{E} = -\nabla\phi$, where $\boldsymbol{E}$ is the electric field. For the numerical simulation we consider a duct of dimensionless size of $35 \times 2 \times 2$ units, using a mesh of 8.3×10^6 CVs with $\delta x = 0.1$, $\delta y = 0.01$, $\delta z = 0.01$. The numerical solution is carried out with a time step of $\delta t = 0.005$ until a converged steady state solution is obtained.

In the presence of a strong magnetic field, characterized by a high Hartmann number, very strong velocity gradients are formed near the duct walls. Particularly, the walls perpendicular to the magnetic field experience significant MHD effects, leading to the formation of the Hartmann boundary layers whose dimensionless thickness is given by $\delta_H = 1/Ha$. In turn, in the walls parallel to the magnetic field, Shercliff layers are formed whose dimensionless thickness can be estimated as $\delta_S = 1/\sqrt{Ha}$. In fact, it is crucial to resolve these boundary layers properly due to their impact on the overall flow. For comparison purposes, the highest Hartmann number considered numerically was 80, so that the Hartmann layer thickness was $\delta_H = 0.025$ and was properly resolved using three points. In turn, for the Shercliff layer, we got $\delta_S = 0.22$. Being significantly thicker than the Hartmann layer, Shercliff layers are well resolved with more than eight points.

Figure 4.3 shows the comparison of the velocity profiles calculated numerically with the exact analytical solution. Since the numerical solution was obtained with the ϕ-formulation, only the velocity profile can be compared, not the induced magnetic field. In Figure 4.3(a), the u velocity component is shown as a function of the y-coordinate at the cross-section plane of the duct in z, while in Figure 4.3(b), the u velocity component is shown as a function of z coordinate at the mid-plane of the duct in y. In both cases, Hartmann number takes the values $Ha = 10, 30, 60, 80$ and $Re = 100$, for the numerical solution velocity profiles are taken at a distance of $x = 30$ where the flow has reached the fully developed condition. In both figures we are indicating the analytical solution with a continuous line and the numerical solution with a line with markers. The observed trend indicates that as the strength of the magnetic field increases, velocity profiles are flattened predominantly in the central region of the flow. As can observed, that both profiles match very well, so we can say that our numerical three-dimensional solution reproduces correctly the flow under consideration.

Figure 4.4 shows the electric potential, ϕ, as well as the induced electric current density vectors on the $y - z$ plane obtained numerically with a Hartmann number of $Ha = 80$ and Reynolds number $Re = 100$. Figure 4.4(a) illustrates the formation of closed loops at opposite ends of the z-coordinate which is consistent with the induced electric current depicted in Figure 4.4(b) where the electric current vectors are perpendicular to the walls at $z = 0, 2$. In fact, since all the walls are electrically conducting, the current also penetrates tangentially the walls normal to the magnetic field. Note that since, the magnetic field is applied in the y-direction, the current flows in the z-direction.
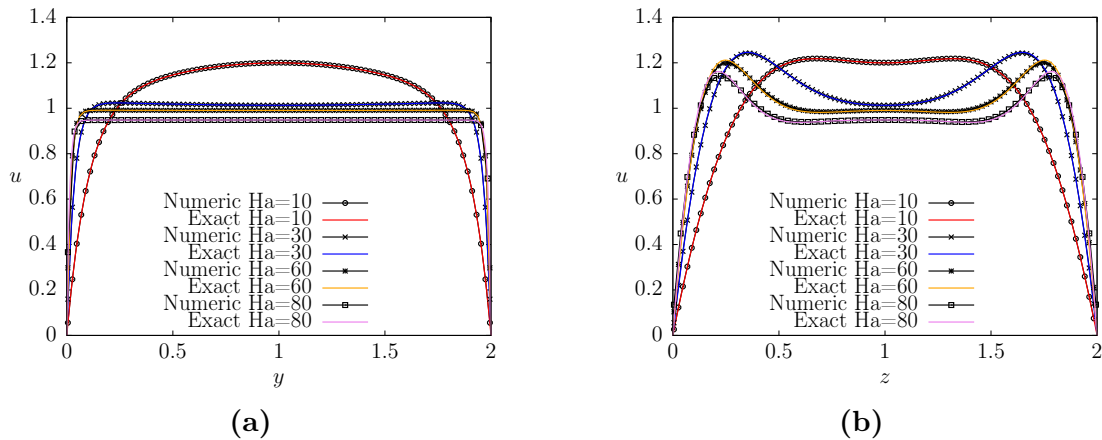
(a)   (b)

Figure 4.3: Comparison of the $u-$component of velocity obtained numerically and analytically, (a) as a function of the $y-$coordinate at the mid-plane of the duct in the $z-$direction, (b) as a function of the $z-$coordinate at the mid-plane of the duct in the $y-$direction, considering a Reynolds number $Re=100$ and Hartmann numbers in the range $10 < Ha < 80$ for a fully developed MHD flow in a duct with all perfectly conducting walls.
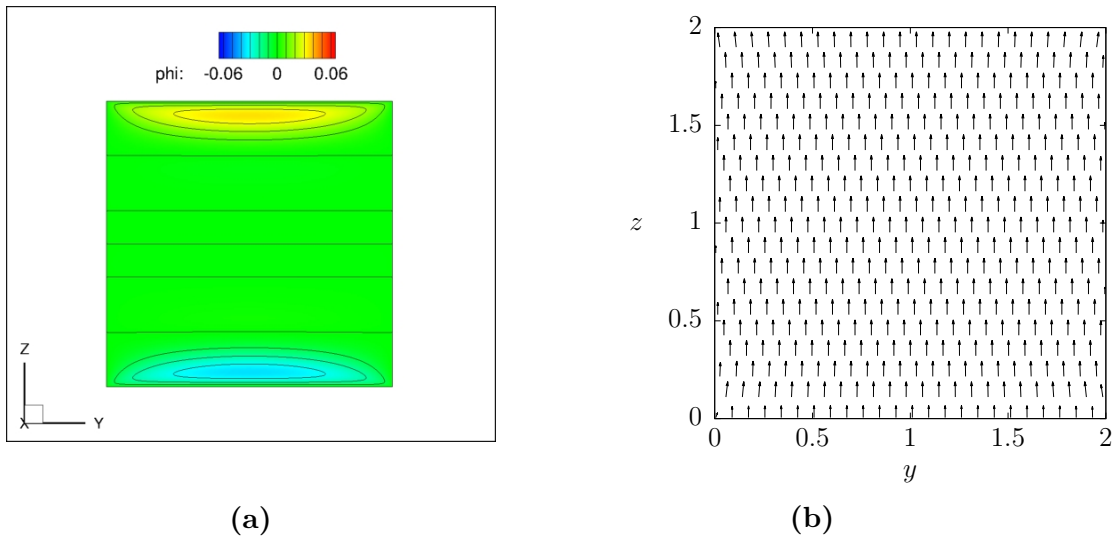

(a)   (b)

Figure 4.4: (a) Isolines of electric potential, ϕ, and (b) electric current density vectors, on the cross-section $y - z$, computed for the Reynolds number $Re = 100$ and the Hartmann number $Ha = 80$ at $x = 30$. Case 1: Duct with perfectly conducting walls.

4.2   CASE 2:   Duct with electrically insulating walls

Now we address the case of an MHD flow through a uniform rectangular cross-section duct under a uniform magnetic field applied in the $y-$direction, similar to

the previous case but assuming that all four solid walls of the duct are electrically insulating. Figure 4.5 shows the configuration considered for which there are available exact analytical solutions with both $B-$ and ϕ-formulations.
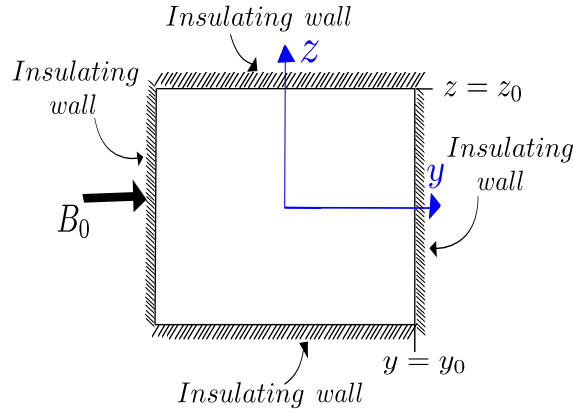

Figure 4.5: Sketch of the duct's cross-section for the analytical solution of an MHD flow in a duct with insulating walls.

4.2.1   Analytical solution with B-formulation

We now present an exact solution for an MHD flow in a rectangular duct with insulating walls following the methodology presented in the book by Hughes and Young [5]. The dimensionless set of equations with B-formulation is given by equations (4.1) and (4.2) while the following boundary conditions must be satisfied

$$u(\pm y_0) = 0, \qquad u_n(\pm z_0) = 0, \tag{4.17}$$

$$\frac{\partial b}{\partial y}(y, \pm z_0) = 0, \qquad \frac{\partial b}{\partial z}(\pm y_0, z) = 0. \tag{4.18}$$

The solution for the axial velocity component and induced magnetic field can be expressed in the form

$$u(y, z) = \frac{Re}{2}\frac{dP}{dx}\left(z^2 - 1 + 4\sum_{n=0}^{\infty}\frac{(-1)^n\alpha(y)}{\Delta_n\lambda^3}\cos(\lambda z)\right), \tag{4.19}$$

$$b(y, z) = 2Re\frac{dP}{dx}\sum_{n=0}^{\infty}\frac{(-1)^n\alpha(y)\beta(y)}{\Delta_n\lambda}\cos(\lambda z), \tag{4.20}$$

where

$$\lambda = (2n+1)\pi/2, \tag{4.21}$$

$$P_{1,2}^2 = \frac{Ha^2}{2} + \lambda^2 \pm Ha\sqrt{\frac{Ha^2}{4} + \lambda^2}, \tag{4.22}$$

$$\alpha(y) = P_2 \left(\lambda^2 - P_1^2\right) \sinh(P_1 y_0) \cosh(P_2 y) - P_1 \left(\lambda^2 - P_2^2\right) \cosh(P_1 y) \sinh(P_2 y_0),$$
(4.23)

$$\beta(y) = \sinh(P_1 y) \sinh(P_2 y_0) - \sinh(P_1 y_0) \sinh(P_2 y),$$
(4.24)

$$\Delta_n = P_2 \left(\lambda^2 - P_1^2\right) \sinh(P_1 y_0) \cosh(P_2 y) - P_1 \left(\lambda^2 - P_2^2\right) \cosh(P_1 y) \sinh(P_2 y_0).$$
(4.25)

4.2.2 Analytical solution with ϕ-formulation

Since the solution for an MHD flow through a uniform rectangular cross-section duct with insulating walls, under a uniform magnetic field applied in one transversal direction has not been previously reported for the $\phi-$formulation, we present this solution using such a formulation. Under the previously stated assumptions of a steady, fully developed flow of a viscous, incompressible, and electrically conducting fluid with constant thermophysical properties, the governing equations can be reduced to the following dimensionless form using the $\phi-$formulation

$$\frac{\partial^2 u}{\partial y^2} + \frac{\partial^2 u}{\partial z^2} + \frac{Ha^2}{k^2} \left(\frac{\partial \phi}{\partial z} - u\right) = \frac{1}{k}\frac{dP}{dx},$$
(4.26)

$$\frac{\partial^2 \phi}{\partial y^2} + \frac{\partial^2 \phi}{\partial z^2} - \frac{\partial u}{\partial z} = 0,$$
(4.27)

where k is the duct's aspect ratio $k = y_0/z_0$.

The boundary conditions required to solve the set of equations given by (4.26) and (4.27) are the following

$$u(\pm y_0) = 0, \qquad u(\pm z_0) = 0,$$
(4.28)

$$\frac{\partial \phi}{\partial y}(\pm y_0, z) = 0, \qquad \frac{\partial \phi}{\partial z}(y, \pm z_0) = 0.$$
(4.29)

We look for a solution of the velocity field and the electric potential that can be expressed in the form

$$u(y, z) = \sum_{n=0}^{\infty} u_n(y) \cos(\lambda_n z),$$
(4.30)

$$\phi(y, z) = \sum_{n=0}^{\infty} \phi_n(y) \sin(\lambda_n z),$$
(4.31)

such that

$$\lambda_n = \frac{\pi}{2}(2n+1). \tag{4.32}$$

By introducing equations (4.30) and (4.31) in the governing equations (4.26) and (4.27) and satisfiying boundary conditions (4.28) and (4.29), it is determined that

$$u_n(y) = A_n \cosh(P_1 y) + B_n \cosh(P_2 y) - \frac{C_n G}{\lambda^2}, \tag{4.33}$$

$$\phi_n(y) = \frac{A_n\left(\text{Ha}^2 + \lambda^2 - P_1^2\right)\cosh(P_1 y) + B_n\left(\text{Ha}^2 + \lambda^2 - P_2^2\right)\cosh(P_2 y)}{\text{Ha}^2 \lambda}, \tag{4.34}$$

where

$$C_n = \frac{\pi(-1)^n}{2n+1}, \qquad G = -\frac{dP}{dx}, \tag{4.35}$$

$$P_{1,2}^2 = \frac{\text{Ha}^2}{2} + \lambda^2 \pm \text{Ha}\sqrt{\frac{\text{Ha}^2}{4} + \lambda^2}, \tag{4.36}$$

$$A_n = -\xi P_2 \left(\text{Ha}^2 + \lambda^2 - P_2^2\right)\text{csch}(P_1 y_0)\sinh(P_2 y_0), \tag{4.37}$$

$$B_n = \xi P_1 \left(\text{Ha}^2 + \lambda^2 - P_1^2\right), \tag{4.38}$$

$$\xi = \frac{C_n G}{\lambda^2 \Delta_n}\frac{\text{sech}(P_1 y_0)}{}, \tag{4.39}$$

$$\Delta_n = P_1 \left(\text{Ha}^2 + \lambda^2 - P_1^2\right)\text{sech}(P_1 y_0)\cosh(P_2 y_0) -$$
$$P_2 \left(\text{Ha}^2 + \lambda^2 - P_2^2\right)\text{csch}(P_1 y_0)\sinh(P_2 y_0).$$

Solutions with both formulations, B and ϕ, are compared in Figure 4.6 for the Hartmann number $Ha = 38$, and Reynolds number $Re = 100$ with aspect ratio $k = 2$. In Figure 4.6(a) the axial velocity is shown as a function of y coordinate and, in Figure 4.6(b) the axial velocity is shown as a function of z coordinate. It can be observed that results obtained with both formulations ϕ and B show an excellent agreement since they are fully equivalent. These solutions are used to validate the numerical solutions in the corresponding limits.
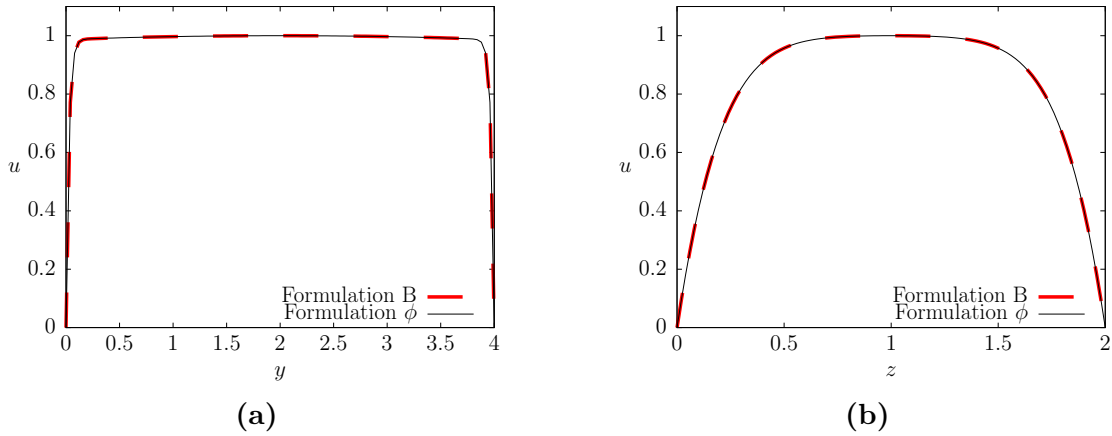
Figure 4.6: Comparison of analytical solutions obtained with both ϕ and B-formulation for $Ha = 38$, $Re = 100$ with aspect ratio $k = 2$, in (a) velocity as a function of y coordinate and (b) velocity as a function of z coordinate.

4.2.3   Numerical solution with ϕ-formulation

We employ the Finite Volume Method described in Section 2.3.1 to develop a three-dimensional numerical solution using the $\phi-$formulation. The boundary conditions used for this numerical solution are identical to those employed in the previous Case 1. However, a significant distinction arises in the electric conditions for the present numerical solution, as the solid walls are now assumed to be perfectly insulating so that condition (4.29) must be satisfied. For the numerical simulation we consider a duct of dimensionless size of $35 \times 2 \times 2$ units, using a mesh of 7.2×10^6 CVs with $\delta x = 0.1$, $\delta y = 0.01$, $\delta z = 0.01$. This numerical solution is solved as time-dependent until reaching a steady state at a time $t = 500$ with a time step of $\delta t = 0.005$. For the highest Hartmann number solved numerically, the dimensionless Hartmann layer thickness $\delta_H = 0.06$ is solved using six points.

Figure 4.7 shows a comparison of velocity profiles obtained numerically and analitycally. In Figure 4.7(a), the u velocity component is shown as a function of y coordinate while in Figure 4.7(b), the u velocity component is shown as a function of z coordinate for different values of Hartmann number $Ha = 10, 30$ and Reynolds number $Re = 100$, while the numerical profiles are taken at $x = 30$ where the flow has reached the fully developed condition. It can be seen that as the strength of the magnetic field increases velocity profiles tend to be flattened. It can be observed that results obtained with both numerical and analytical solutions show a good agreement, so that the numerical solution correctly reproduces the flow in the corresponding limit.

Now, in order to contrast the effect of the electrical conductivity of the walls on the induced current, we present in Figure 4.8 the electric potential, ϕ, and the induced electric current density vectors in the $y - z$ plane for $Ha = 60$ and $Re = 100$ at $x = 30$ for the case of electrically insulating walls obtained from the numerical
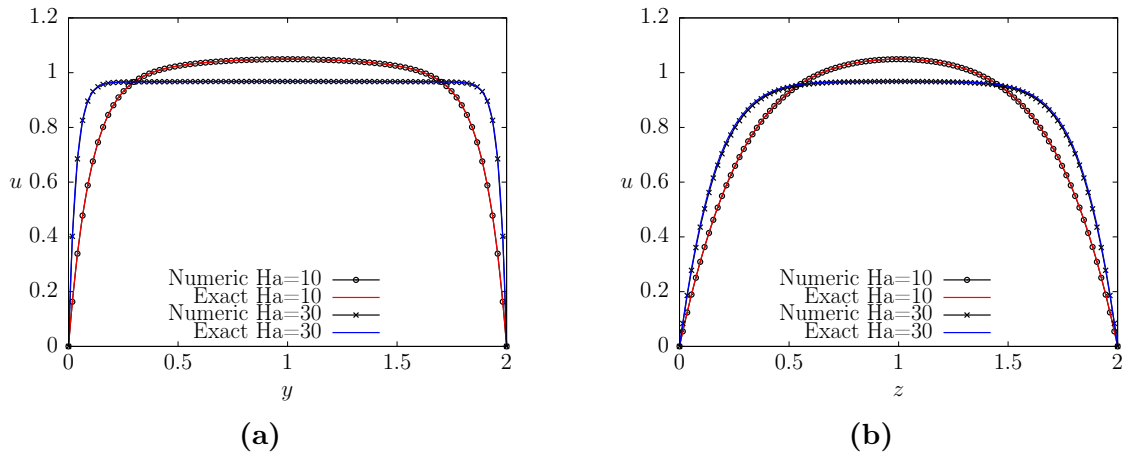
Figure 4.7: Comparison between numerical and exact solutions for Reynolds number $Re = 100$ and different values of Hartmann number $Ha = 10, 30$ for the MHD flow in a duct with insulating walls. (a) u component of the velocity as a function of y coordinate, and (b) u component of the velocity as a function of z coordinate.

solution. Figure 4.8(a) illustrates the formation of horizontal lines in the y-direction that do not close, indicating a potential difference in the z-direction perpendicular to the applied magnetic field. On the other hand, in Figure 4.8(b) the electric current vectors show the formation of two current loops, with the predominant current direction being more pronounced in the z-direction at the center of the duct. The current returns along the walls perpendicular to the applied magnetic field. For clarity of the description of the current path, in Figure 4.9, the electric current density vectors are amplified near the duct wall to observe the current return occurring at a distance of $d = 0.05$ units from the wall. Relating this fact to the Hartmann layer, with $\delta_H = 0.03$, we have solved for three points inside δ_H, which for these conditions is a proper resolution.
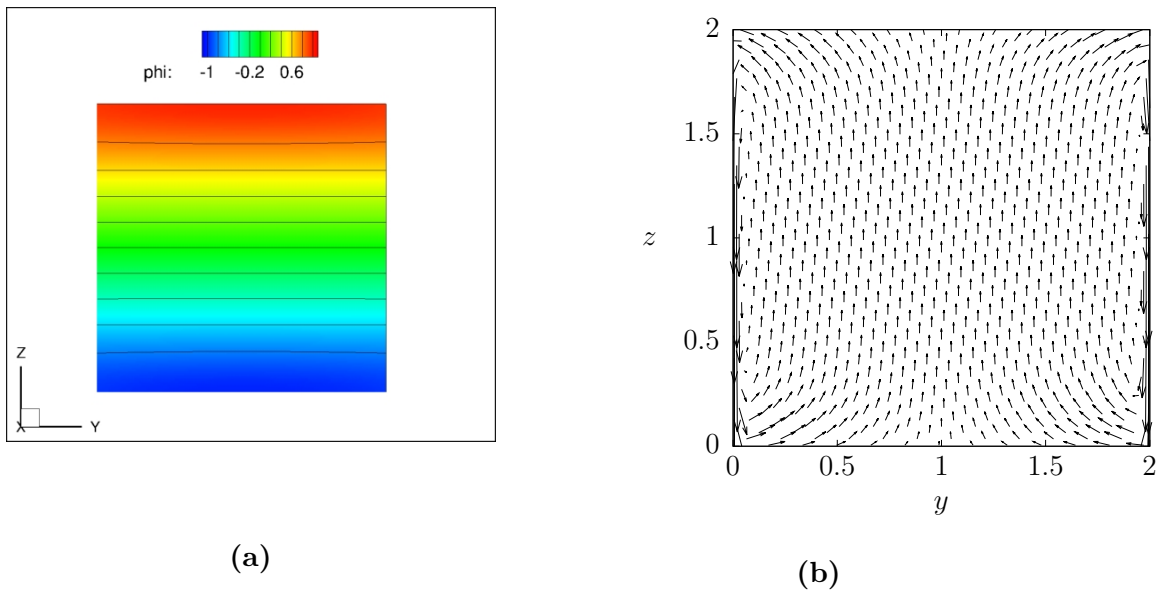
(a)

(b)

Figure 4.8: Numerical results for Case 2: Duct with electrically insulating walls, for the parameters $Ha = 60$ and $Re = 100$. (a) Electric potential ϕ in the cross section and (b) electric current recirculation in the cross-section.
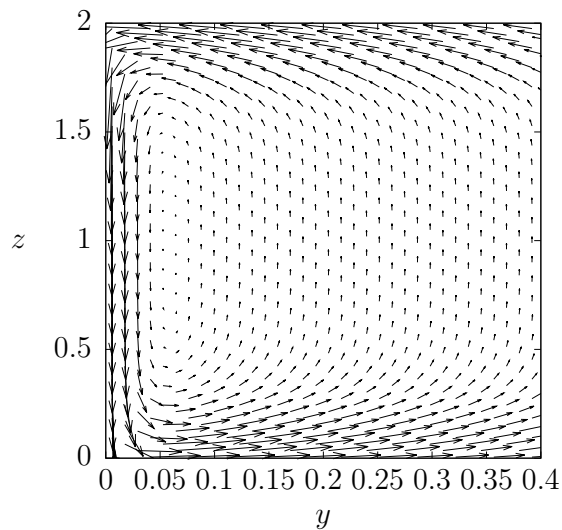

Figure 4.9: Zoom in the region of the return of the electric current near to $x-z$ plane to visualize the size of the layer where the electric current changes its direction.

4.3 CASE 3: Duct with perfectly conducting walls perpendicular to the applied magnetic field

4.3.1 Analytical solution with ϕ-formulation

We now obtain an exact solution for the MHD flow in a rectangular duct with two perfectly conducting walls perpendicular to the uniform magnetic field and two insulating walls parallel to the field. Although this solution is well known in terms of the B-formulation [5], apparently it had not been reported for the ϕ-formulation [70]. Therefore, it could be useful for validation of numerical codes based on the latter. The analytical solution is obtained by solving the equations (4.26) and (4.27). Boundary conditions are changed in order to combine perfectly conducting and insulating walls, as shown in Figure 4.10.
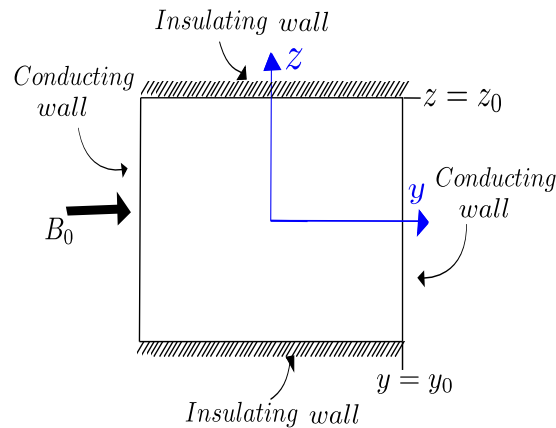

Figure 4.10: Sketch of physical domain for the analytical solution for a duct with conducting walls perpendicular to the applied magnetic field.

Mathematically, perfectly conducting and electrically insulating walls satisfy, respectively, the following boundary conditions

$$\frac{\partial \phi}{\partial z}(\pm y_0, z) = 0, \qquad \frac{\partial \phi}{\partial z}(y, \pm z_0) = 0. \tag{4.40}$$

The velocity field which satisfies the boundary conditions is expressed in the form

$$u(y, z) = \sum_{n=1,3\ldots}^{\infty} \sum_{m=1,3\ldots}^{\infty} A_{mn} \cos \frac{n\pi y}{2k} \sin \frac{m\pi z}{2}, \tag{4.41}$$

where

$$A_{mn} = \frac{-16\frac{Re}{k}\frac{dP}{dx}\left(m^2 + \frac{n^2}{k^2}\right)\sin\frac{n\pi}{2}\cos\frac{m\pi}{2}}{mn\pi^2\left[\frac{\pi^2}{4}\left(m^2 + \frac{n^2}{k^2}\right)^2 + Ha^2\left(\frac{n^2}{k^4}\right)\right]},\tag{4.42}$$

while the electric potential is given by

$$\phi(y,z) = \frac{2}{\pi}\sum_{n=1,3\ldots}^{\infty}\sum_{m=1,3\ldots}^{\infty} B_{mn}\cos\frac{n\pi y}{2k}\sin\frac{m\pi z}{2},\tag{4.43}$$

where

$$B_{mn} = \frac{-16\frac{Re}{k}\frac{dP}{dx}\sin\frac{n\pi}{2}\cos\frac{m\pi}{2}}{n\pi^2\left[\frac{\pi^2}{4}\left(m^2 + \frac{n^2}{k^2}\right)^2 + Ha^2\left(\frac{n^2}{k^4}\right)\right]}.\tag{4.44}$$

Then, from Ohm's law, the electrical current density

$$j_y = \frac{1}{k}\sum_{n=1,3\ldots}^{\infty}\sum_{m=1,3\ldots}^{\infty} nB_{mn}\sin\frac{n\pi y}{2k}\sin\frac{m\pi z}{2},\tag{4.45}$$

$$j_z = \frac{1}{k^2}\sum_{n=1,3\ldots}^{\infty}\sum_{m=1,3\ldots}^{\infty} \frac{n^2}{m}B_{mn}\cos\frac{n\pi y}{2k}\cos\frac{m\pi z}{2}.\tag{4.46}$$

Figure 4.11 presents velocity maps for different Hartmann numbers ($Ha = 0, 30, 100$) in a duct with an aspect ratio of $k = 3$, while keeping the Reynolds number constant at $Re = 100$. It can be observed that the no-slip boundary conditions are satisfied, and the location of the maximum velocity depends on the Hartmann number. Unlike the case of a duct with insulating walls, where the maximum velocity is typically found in the center of the duct, here the maximum velocity approaches the insulating walls as the Hartmann number increases. In fact, for high Hartmann numbers, a pair of jets appears close to these walls, as shown in Figure 4.12, where different velocity profiles for various Hartmann numbers are displayed for an aspect ratio of $k = 1$ and Reynolds number $Re = 100$. Additionally, Figure 4.12(a) depicts the velocity as a function of the z coordinate, while Figure 4.12(b) shows the velocity as a function of the y coordinate for $k = 1$, and $Ha = 0.1, 1, 30, 100$. In all cases, mass conservation is verified. As the Hartmann number increases, the flow tends to form jets close to the insulating walls. Consequently, the mass flow is predominantly carried by these side jets rather than the bulk flow in the central region. This results in significantly reduced velocities in the central region, and in some cases, the velocity can even become negative.

4.3.2 Numerical solution with ϕ-formulation

We employ the Finite Volume method to develop a three-dimensional numerical solution using the $\phi-$formulation. The boundary conditions used for this numerical
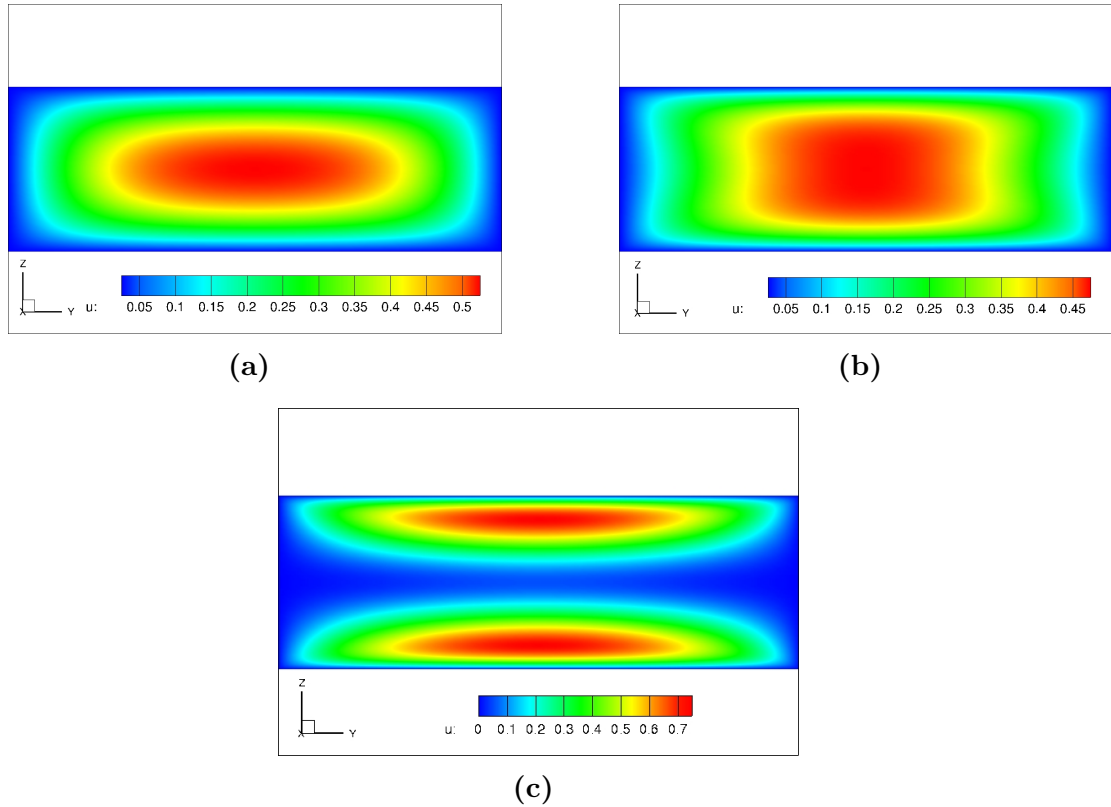
Figure 4.11: Velocity maps for Reynolds number $Re = 100$, $k = 3$ and different Hartmann numbers: (a) $Ha = 0$, (b) $Ha = 30$ and (c) $Ha = 100$, for the CASE 3: Duct with conducting walls perpendicular to the applied magnetic field.
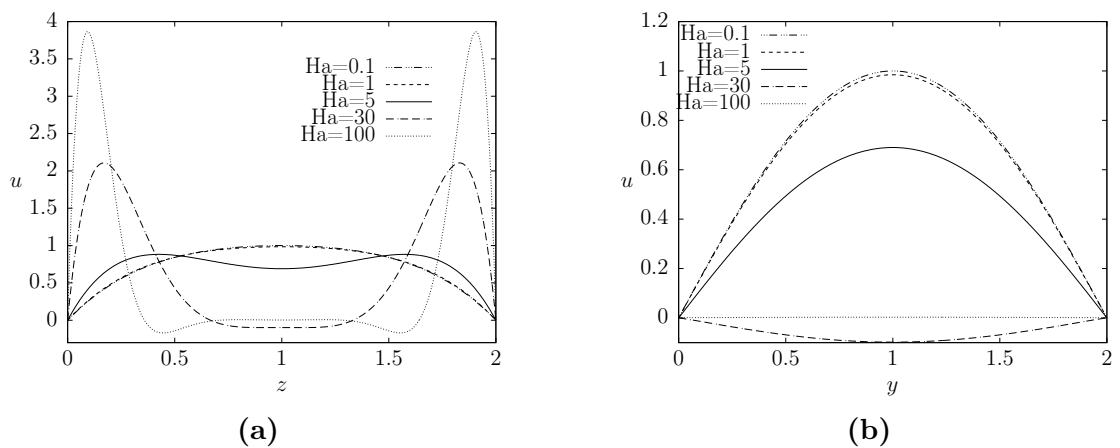

Figure 4.12: Velocity profiles for $Re = 100$, $k = 1$ and different Hartmann numbers $Ha = 0.1, 1, 5, 30, 100$. (a) u as a function of z coordinate and (b) u as a function of y coordinate.

solution are a combination of those employed in the previous Case 1 and Case 2. Conditions (4.40) must be satisfied. For the numerical simulation we consider a duct of dimensionless size of $35 \times 2 \times 2$ units, using a mesh of 7.9×10^6 CVs with $\delta x = 0.1$, $\delta y = 0.01$, $\delta z = 0.008$. The numerical solution is solved as time dependent until reaching a steady state at a time $t = 300$ with a time step of $\delta t = 0.005$.

Both analytical and numerical solutions are compared in order to validate the numerical solutions in the corresponding limits. In Figure 4.13(a), the u velocity component is shown as a function of y coordinate while in Figure 4.13(b), the u velocity component is shown as a function of z coordinate at $x = 30$ for the numerical solution. It can be seen that results obtained show a good agreement for the Hartmann numbers $Ha = 5, 10$ and Reynolds number $Re = 100$.

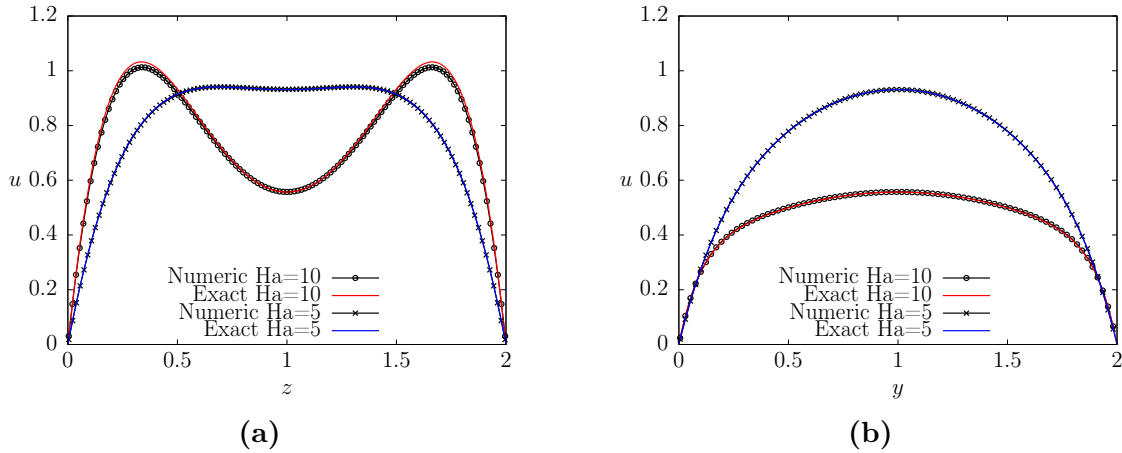(a)   (b)

Figure 4.13: Comparison between numerical and exact solutions for $Ha = 5$ and 10 for the MHD flow in a rectangular duct with two perfectly conducting walls perpendicular to the applied field and two insulating walls. (a) u velocity component as a function of y coordinate and (b) u velocity component as a function of z coordinate.

Figure 4.14 shows isolines of electric potential and electric current density vector field for the parameters $k = 1$, $Re = 100$ and $Ha = 30$. It is important to notice that the electric current distribution determined by the combination of insulating and perfectly conducting walls, has a direct influence in the flow dynamics. As the Hartmann number increases, close to the insulating walls the current density is almost parallel to the applied magnetic field and therefore, the braking Lorentz force $\boldsymbol{j} \times \boldsymbol{B}^0$ is negligible. On the other hand, in the central region the current density is perpendicular to the applied field and the Lorentz force that brakes the flow is maximum. This explains the formation of the side jets and the small velocity in the central region.
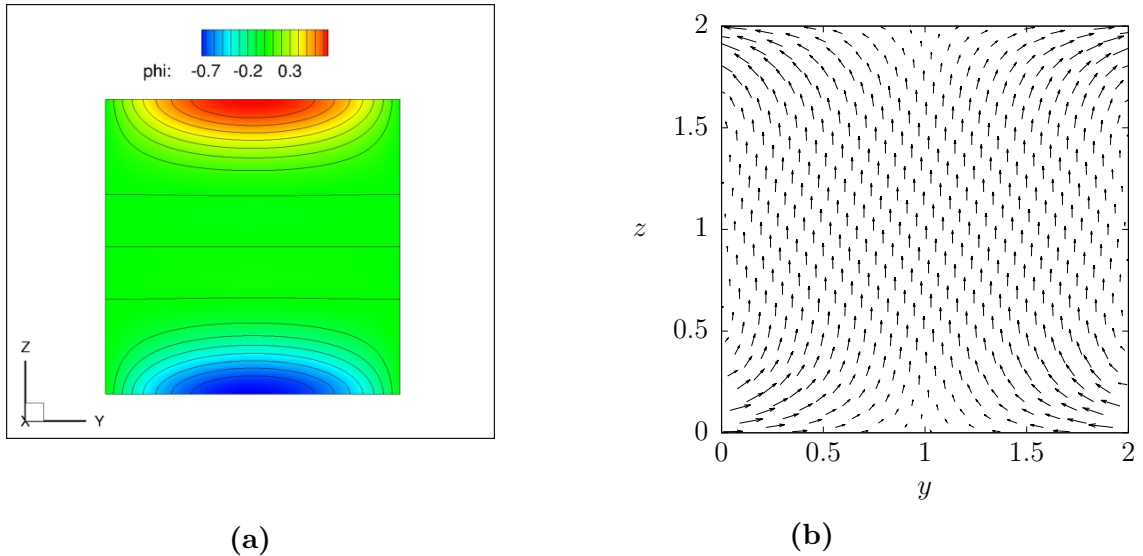
(a)   (b)

Figure 4.14: Numerical results of (a) electric potential denoted as ϕ and (b) electric current density, obtained for the parameters $k = 1$, $Re = 100$ and $Ha = 30$ for CASE 3: Duct with conductive walls perpendicular to the applied magnetic field.

4.3.3 Heat transfer problem

For the sake of illustration, we now asses the effect of the MHD flow in the heat transfer process, we use the velocity profile of the exact solution for the Case 3, to solve numerically the three-dimensional heat transfer problem in which a pair of walls, either the conducting or the insulating ones, are exposed to a uniform heat flux.

We consider the fully developed flow of a viscous, incompressible electrically conducting fluid in a duct of constant rectangular cross-section under a transverse uniform magnetic field. It is assumed that the applied field is perpendicular to a pair of perfectly conducting walls and is parallel to a pair of insulating walls. In addition, a constant and uniform heat flux is applied at both perfectly conducting walls, while the insulating walls parallel to the field remain adiabatic. Figure 4.15 shows an sketch of the treated problem. The case where the heat flux is applied at the insulating walls is also considered.

Numerical results

As it was mentioned above, the analytical velocity profile was used to solve the forced convection heat transfer problem in the duct, assuming that a pair of walls, either the perfectly conducting or the insulating ones, receive a constant uniform heat flux. We consider that the duct has a square cross-section whose dimensions in the $x - y - z$-directions are $10 \times 2 \times 2$, respectively. At the inlet the fluid temperature is assumed to be constant. Mathematically, the thermal boundary conditions applied to the solution of equation (2.28) for the case in which the heat flux enters at the
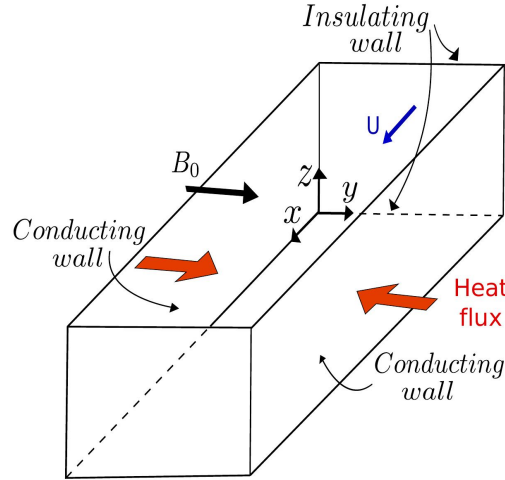
Figure 4.15: Sketch of flow and heat transfer analyzed problem.

perfectly conducting walls are:

$$\frac{\partial T}{\partial z} = 0, \quad z = 0, 2, \ \ 0 \le y \le 2, \ \ 0 \le x \le 10, \tag{4.47}$$

$$\frac{\partial T}{\partial y} = 1, \quad y = 0, 2, \ \ 0 \le z \le 2, \ \ 0 \le x \le 10, \tag{4.48}$$

$$T = 0, \quad x = 0, \ \ 0 \le y \le 2, \ \ 0 \le z \le 2. \tag{4.49}$$

The numerical solution methodology has been presented in Section 2.3.1.

Figure 4.16(a) shows the temperature profile in the mid-plane $y = 0$ at the heated perfectly conducting wall, $z = 1$, as a function of x-coordinate for a Hartmann number $Ha = 30$ and different Péclet numbers, $Pe = 15.9, 26.5, 53$. It can be clearly observed that as the Péclet number grows, the wall temperature decreases, indicating a heat transfer enhancement. In turn, Figure 4.16(b) shows the temperature profiles at the heated (perfectly conducting) wall, $z = 1$, for three different Ha numbers $Ha = 0, 30, 100$ and a fixed Péclet number $Pe = 26.5$. It can be noticed that the lowest wall temperature is obtained when $Ha = 0$, that is, when the profile is the hydrodynamic one. As Ha increases, the wall temperature increases manifesting the influence of the small velocities found at the heated wall due to a stronger opposing Lorentz force. Therefore, in this case the hydrodynamic parabolic profile leads to a more efficient heat removal than the flat MHD profile (see Figure 4.12(b)).

Figure 4.17 shows the local Nusselt number at the heated perfectly conducting wall as a function of x-coordinate for different Péclet numbers, $Pe = 53, 530, 2650$, and a fixed Hartmann number $Ha = 30$. Remember that we have previously defined the local Nusselt number, also known as the local heat transfer coefficient as

$$Nu_x(x,t) = \left.\frac{\partial T}{\partial y}\right|_w \frac{L_y}{T_b - T_w}, \tag{4.50}$$

where L_y is the distance between the heated walls, T_w is the wall temperature and T_b is the bulk temperature given by

$$T_b(x,t) = \frac{\int_0^{L_y} uT dy}{\int_0^{L_y} u dy}. \tag{4.51}$$

The parameter Nu_x gives information about the local heat transfer rate and, as it is expected, the larger the Péclet number, the larger the heat removal and the lower the wall temperature, as discussed in Figure 4.16(a).

(a) $Ha = 30$.

(b) $Pe = 26.5$.

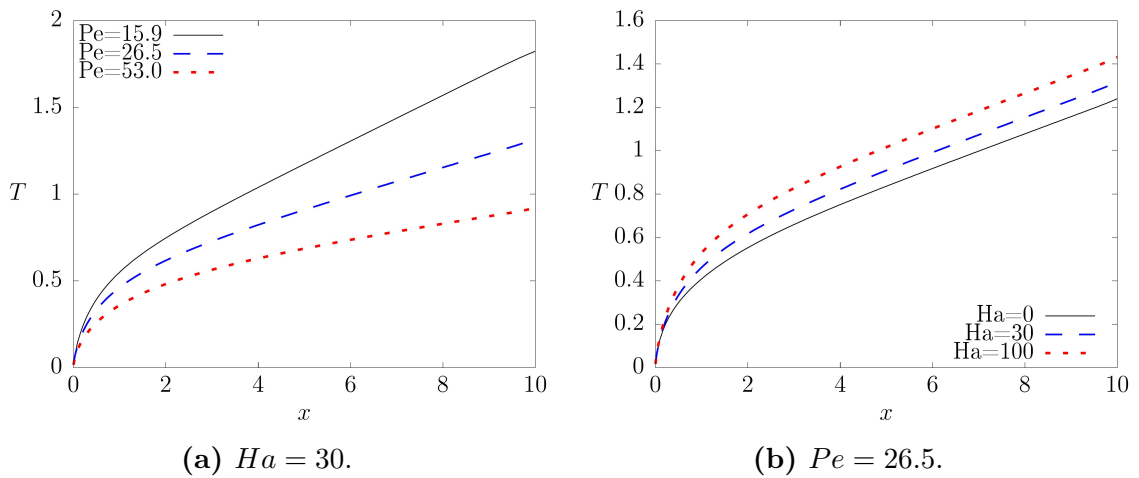Figure 4.16: Temperature profiles at the heated perfectly conducting wall, $z = 1$, at $y = 0$, for different Péclet and Hartmann numbers ($k = 1$).

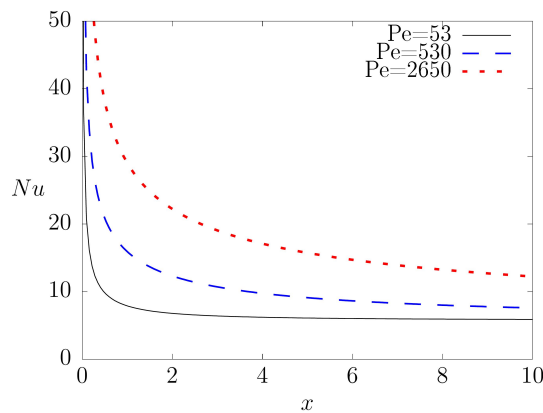Figure 4.17: Local Nusselt number as a function of x coordinate for different Péclet numbers when Ha=30.

Let us now explore the heat transfer when the uniform heat flux is applied at the insulating walls. An effect is expected since the flow exhibits high velocity jets near

the insulating walls, parallel to the applied magnetic field. Figure 4.18 shows the wall temperature profiles along a heated insulating wall, $y = 1$, at the mid-plane $z = 0$, as a function of the x-coordinate for the same parameters used in Figure 4.16. As in the previous case (see Figure 4.16(a)), Figure 4.18(a) shows that the larger the the Péclet number for a given Hartmann number ($Ha = 30$) the lower the wall temperature. However, in this case, the reduction in wall temperature is higher than the case of the heated conducting wall. In addition, Figure 4.18(b) shows the temperature profiles at the heated insulating wall for different Hartmann numbers observing that the higher the Hartmann number the lower the wall temperature. Evidently, this occurs due to the presence of the high velocity jets that appear near these walls for high Ha promoting a more efficient heat removal.
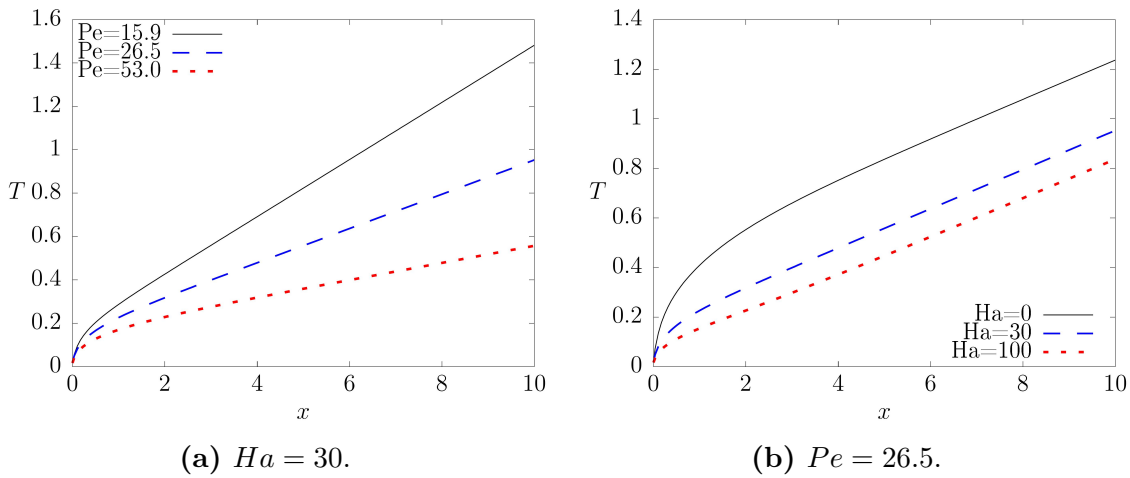

(a) $Ha = 30$.   **(b)** $Pe = 26.5$.

Figure 4.18: Temperature profile at the heated insulating wall, $y = 1$, at $z = 0$ for different Péclet and Hartmann numbers ($k = 1$).

In this section, we used the MHD formulation based on the electric potential to obtain an exact analytical solution for the fully developed flow of a liquid metal in a duct of rectangular cross-section with two insulating walls and two perfectly conducting walls perpendicular to the applied magnetic field. This solution is equivalent to the reported solution in terms of the induced magnetic field [5]. The analytical velocity profile was used to explore numerically the forced convective heat transfer when a constant and uniform heat flux is imposed on either the perfectly conducting or the insulating walls. As expected, the heat transfer process is strongly influenced by the flow pattern which displays high velocity regions near both insulating walls for high values of the Hartmann number. For a fixed Péclet number, when the heat flux enters the perfectly conducting walls, the hydrodynamic profile leads to a stronger heat removal and lower wall temperatures than the MHD profiles. However, when the surface heat flux is set at the insulating walls where the high velocity regions are formed, the heat removal is more efficient the larger the Hartmann number leading to lower wall temperatures. It was also verified that for a constant Hartmann number, the local Nusselt number increases as the Péclet number grows, which indicates a better heat removal from the heated wall.

Three-dimensional modeling of the flow past a magnetic obstacle

In this chapter[‡], we explore in detail the dynamics of liquid metal flows in ducts under localized magnetic fields in different regimes with the aim of describing the overall flow behavior as the Reynolds number grows for a fixed Hartmann number, which leads to different steady and time-dependent flow patterns. Although our interest is mainly addressed to flows where inertia is not negligible, we present an analytical solution obtained by a perturbation method for the creeping flow past a magnetic point dipole. This is the first reported analytical solution which reproduces the characteristic flow pattern of six vortices that has been found in experimental and numerical studies. Afterwards, we perform a three-dimensional numerical analysis of the experimental flow reported by Domínguez *et al.* [45] where wakes generated by a fixed localized magnetic field in a flow of liquid metal driven by an electromagnetic pump in a loop formed by a rectangular duct of slender cross-section, were explored. Experimental results obtained with an Ultrasonic Doppler Velocimeter are numerically reproduced and, particularly, the interplay between inertia and electromagnetic forces observed experimentally is consistently replicated by the numerical model. Further, different three-dimensional flow patterns are examined and characteristic features that were not obtained from the experiment are identified.

5.1   Background

Several technological applications, particularly in the metallurgical industry, rely on the use of steady magnetic fields to suppress unwanted motion and promote a more quiescent process. That is the case, for instance, of the cold crucible technique or the continuous casting of steel where the application of a steady magnetic field that embraces the whole flow region allows the control of liquid metal free surfaces. The stabilizing effect of a steady field involves, on the one hand, the damping of velocity fluctuations due to the dissipation of induced electric currents circulating in the liquid metal, so that kinetic energy is transformed into heat by Joule dissipation [61]. On the other, electric currents circulating in boundary layers attached to walls with a normal component of the applied magnetic field, give rise to a Lorentz force that promotes the braking of the fluid motion, what is known as Hartmann braking.

[‡]This chapter is mainly based on the paper: Solano-Olivares, V., Cuevas, S. & Figueroa, A. 2023 "Interaction of inertia and magnetic forces in the liquid metal flow past a magnetic obstacle". In preparation.

But steady magnetic fields can also be the source of unstable behavior. This may occur when heterogeneous electromagnetic conditions are present in the flow, promoting the creation of Lorentz forces able to produce a destabilizing effect on the flow by modifying the mean-flow velocity distribution. For instance, non-uniformities of the electrical conductivity of the walls may produce the formation of internal shear layers and lead to the emergence of flow instabilities when inertial effects are not negligible [71]. In fact, the creation of inflection points in the velocity profile is the mechanism by which Lorentz forces may reduce the stability of the flow. Internal shear layers can also be created in liquid metal flows due to non-uniformities in the applied magnetic field, particularly when the magnetic source is confined in a small zone compared with the full flow region. In fact, induced currents in the liquid metal interact with the applied magnetic field, giving rise to a localized Lorentz force that, acting as an obstacle, namely, a *magnetic obstacle*, brakes the fluid and creates vorticity. In low-Reynolds number flows, a magnetic obstacle can create steady flow patterns that display structures not observed in the flow past solid obstacles (see, for instance [27, 28]). If, in turn, inertial effects are sufficiently strong, the obstruction created by the magnetic obstacle can lead to unstable behavior manifested in the appearance of vortex shedding and the formation of a time-dependent wake. However, when strong dissipation is also present, such as due to confining walls, the flow can be stabilized and the occurrence of vortex shedding is avoided [30].

The flow past bluff bodies, for instance cylinders or spheres, is one of the most studied problems in fluid dynamics and, therefore, its phenomenology is very well known. In fact, the observed flow patterns as the Reynolds number increases have been clearly established from experiments and numerical simulations. For example, in the case of the flow past a cylinder, it is found that when the Reynolds number is small ($Re \ll 1$), a laminar flow surrounds smoothly the obstacle. As Re increases ($Re \approx 10$), steady vortices appear symmetrically behind the obstacle being elongated as the governing parameter grows even further. When Re reaches a critical value ($Re \approx 100$), vortices can no longer remain attached to the obstacle and are shed periodically forming a highly structured wake, namely, the Bénard-von Kármán vortex street. If Re increases ($Re \approx 10^4$) the flow becomes turbulent but the wakes still preserves some structure. Finally, at higher Re values ($Re \approx 10^5$), a fully turbulent wake is obtained [72].

One may wonder if an analogous situation could be explored in the flow past a magnetic obstacle. As we have mentioned, although some similarities exist between the flow past solid obstacles and the flow past magnetic obstacles, important differences can be identified that lead to substantial distinctions in dynamic behavior and flow patterns. While the flow past solid obstacles is governed essentially by one dimensionless parameter, that is Re, in the magnetic obstacle case an additional parameter comes into play, namely, either the Hartmann number, Ha, or the interaction parameter, N. This manifest the fact that in addition to the role that inertial and viscous forces play in the hydrodynamic problem, magnetic forces also determine the MHD flow. Therefore, the expected dynamic behavior in the flow past a magnetic obstacle will be established by the interaction of these forces. As Ha determines the strength of the magnetic force that opposes the oncoming flow, it can be thought as a parameter that characterises the *rigidity* of the magnetic obstacle. Hence, it

becomes a relevant issue to explore the flow dynamics for a fixed Hartmann while the Reynolds number is varied. Incidentally, this issue was experimentally addressed by Domínguez *et al.* [45] who analysed the wake dynamics behind a magnetic obstacle in a liquid metal duct flow through UDV measurements. They observed that, for a given Hartmann number, as the Reynolds number increases, the flow undergoes a transition from a steady state to a time-dependent state. However, in contrast to the wake of a solid obstacle, further increasing the Reynolds number results in the flow returning to a steady state. These authors implemented a quasi-two-dimensional numerical model to try to reproduce the experimental observations although the comparison is limited due to the nature of the model.

In this work, we use the experimental data obtained by Domínguez *et al.* [45] to validate the developed three-dimensional numerical code and overcome the limitations of the quasi-two-dimensional approach so that a more complete understanding of the analysed flow is provided. The main objective is to determine the interplay between inertia and magnetic forces, focusing on the transient behavior of the wake structure behind a magnetic obstacle with a high constrainment factor (analogous to blockage ratio), as well as on the observed vortical structures. Moreover, extending the range of dimensionless parameters beyond those explored experimentally, different flow patterns of stationary vortices are reproduced and its three-dimensional structure is discussed.

5.2   Experimental setup

We now briefly describe the experimental setup used by Domínguez *et al.* [45] to analyse the flow of a liquid metal past a magnetic obstacle. It consists of rectangular loop made of acrylic walls with a rectangular effective cross-section of 1 cm × 8 cm. It is formed by two long and two short legs with lengths of 85.8 cm and 40 cm, respectively. The working fluid was the eutectic alloy Galinstan which is liquid at room temperature, and has kinematic viscosity of $\nu = 3.3 \times 10^{-7}$ m^2 s^{-1}, an electrical conductivity $\sigma = 3.46 \times 10^6$ Ω^{-1} m^{-1}, and a mass density $\rho = 6360$ kg m^{-3}. The liquid metal was driven by an electromagnetic induction pump located on one of the long legs. The pump consisted of a motor that rotates two parallel disks where 24 permanent neodymium magnets are radially mounted, so that the duct was between the disks. An ultrasonic Doppler velocimeter (UDV) was used to measure the velocity of the liquid metal with a probe of 0.8 cm in diameter and a wave frequency of 4 MHz. This instrument allowed to determine one component of the velocity along the propagation line of the acoustic wave emerging from the emitter. The ultrasonic gauge was fixed at the downstream end of the region of analysis to detect the axial velocity along the axial coordinate.

Figure 5.1(a) shows a photograph of the experimental device indicating the position of the MHD pump, the magnets and the UDV system. In turn, Figure 5.1(b) presents a sketch showing the position of the magnets and the UDV, together with some details of the flow, and the axes of coordinates used in the numerical study. The magnetic obstacle was created with two identical neodymium square
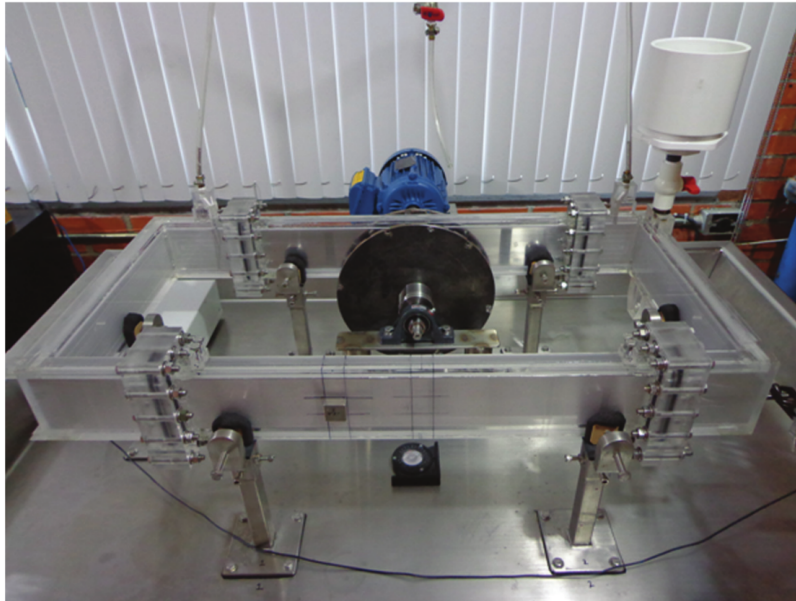
(a) The experimental liquid metal loop. The MHD pump is in the far long leg. The disks with permanent magnets and the liquid metal rotate in the counterclockwise direction. The magnets that generate the magnetic obstacle are close to the central part of the near long leg, 30 cm away from the upstream corner and 4 cm above the lower wall of the duct. The ultrasonic gauge is in the far right of the picture near the duct corner.
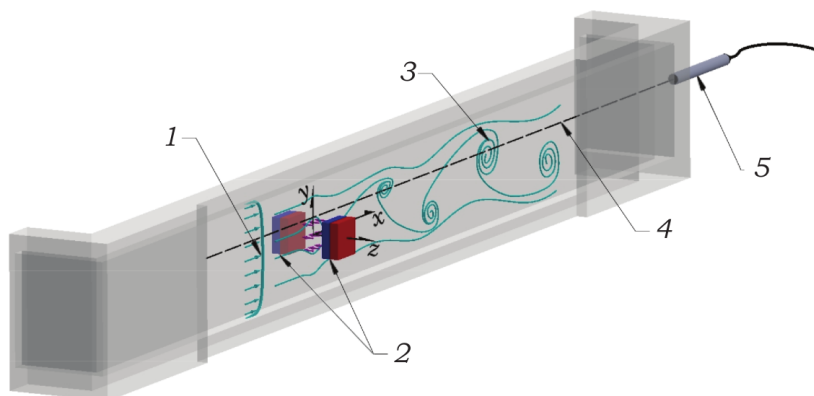
(b) Sketch of the observation zone and position of the axis of coordinates. 1 − upstream velocity profile, 2 - magnets, 3 - wake of the magnetic obstacle, 4 - line for ultrasonic Doppler velocity recordings, 5 - ultrasonic Doppler velocimetry probe.

Figure 5.1: Taken from Domínguez *et al.* [45].

magnets with a side length of 2.54 cm and a thickness of 1.25 cm, placed on the outer side of the opposite vertical walls of the central part of one of the long legs and located 30 cm away from the upstream corner and 4 cm from the lower horizontal wall of the duct (see Fig. 5.1(b)). With this magnet configuration, the maximum magnetic field obtained at the center of the duct was 0.23 T, and the constrainment factor is $\kappa = 0.36$ (side of the magnet/height of the duct) and a gap ratio $h = 1.1$ (magnet-wall distance/side of the magnet). However, by separating the magnets, reduced strengths were also obtained. For comparison purposes with the numerical results presented here, a maximum magnetic field strength of $B_m = 0.185$ T was considered that corresponds to a separation distance of 31 mm.

Before presenting the corresponding results of the numerical simulation, in the following section the analytical solution of the flow past a magnetic point dipole under creeping flow conditions is addressed.

5.2.1 Two-dimensional analytical model

Although most of the studies of flows under localized magnetic fields address cases where inertial effects are not negligible, it is interesting to explore these phenomenon under creeping flow conditions. In fact, only few works have considered the flow past a magnetic obstacle assuming that the Reynolds number is very low (see for instance [27], [28]). Making this assumption offers the opportunity to search for analytical solutions under simplified conditions, as shown below.

With the aim at getting analytical solutions of equations (2.23)-(2.26), we introduce some simplifying assumptions. We consider a two-dimensional liquid metal flow in an unbounded region where a non-uniform magnetic field produced by a magnetic point dipole is present. Far from the magnetic source, the flow is assumed steady and uniform. The motion of the fluid within the applied magnetic field induces electric currents which interact with the same magnetic field, producing a non-uniform Lorentz force that modifies the original flow and creates vorticity. Under these conditions, only the component of the applied magnetic field normal to the plane of motion is relevant, namely $B_z^0(x, y)$. With these assumptions, the governing equations reduce to

$$\frac{\partial u}{\partial x} + \frac{\partial v}{\partial y} = 0, \tag{5.1}$$

$$\frac{\partial u}{\partial t} + u\frac{\partial u}{\partial x} + v\frac{\partial u}{\partial y} = -\frac{\partial p}{\partial x} + \frac{1}{Re}\nabla_\perp^2 u + \frac{Ha^2}{Re}\,j_y B_z^0, \tag{5.2}$$

$$\frac{\partial v}{\partial t} + u\frac{\partial v}{\partial x} + v\frac{\partial v}{\partial y} = -\frac{\partial p}{\partial y} + \frac{1}{Re}\nabla_\perp^2 v - \frac{Ha^2}{Re}\,j_x B_z^0, \tag{5.3}$$

$$j_x = -\frac{\partial \phi}{\partial x} + vB_z^0, \quad j_y = -\frac{\partial \phi}{\partial y} - uB_z^0, \tag{5.4}$$

$$\nabla_\perp^2 \phi = \omega_z, \tag{5.5}$$

where $\omega_z = \partial v/\partial x - \partial u/\partial y$ is the vorticity in the z-direction. Additionally, the subindex $\perp$ indicates the projection of the ∇ operator on the (x, y)-plane. Upon taking the curl of equations (5.2)-(5.3) and using the law of charge conservation $\nabla \cdot \boldsymbol{j} = 0$, assuming steady state we get the following vorticity transport equation for the only component ω_z

$$Re \left(u\frac{\partial \omega_z}{\partial x} + v\frac{\partial \omega_z}{\partial y} \right) = \nabla_\perp^2 \omega_z - Ha^2 \left(j_x\frac{\partial B_z^0}{\partial x} + j_y\frac{\partial B_z^0}{\partial y} \right). \tag{5.6}$$

The normal component of a two-dimensional magnetic point dipole located at the origin with its magnetic dipole moment pointing in the positive z-direction, can be expressed as [27, 73]

$$B_z^0(x, y) = \frac{\eta}{\pi} e^{-\eta(x^2+y^2)}. \tag{5.7}$$

Considering $\eta > 0$, equation (5.7) represents a two-dimensional Gaussian-like magnetic distribution for the normal component. The induced electric currents can be obtained from the Ohm's law, eq. (5.4). We assume that far from the magnetic dipole, a steady uniform flow in the positive x-direction is imposed. With the origin of coordinates located at the point of maximum magnetic field strength, the boundary conditions on the velocity components are

$$u(x, y) \to 1, \quad v(x, y) \to 0, \quad \text{as } x, y \to \pm\infty. \tag{5.8}$$

As a first approximation, we assume that, for the unperturbed flow, the Poisson's equation (5.5) for the electric potential is

$$\nabla_\perp^2 \phi = 0. \tag{5.9}$$

As no external potential difference is applied, the solution for (5.9) is $\phi(x, y) = 0$. Thus, the components of the induced electric current are

$$j_x(x, y) = 0, \quad j_y(x, y) = -B_z^0(x, y). \tag{5.10}$$

In order to linearize the equations of motion, we assume that the flow past the magnetic point dipole is only slightly perturbed by the Lorentz force produced by the interaction of the induced electric currents with the applied field. Therefore, the dimensionless velocity components can be expressed as

$$u(x, y) = 1 + u'(x, y), \quad v(x, y) = v'(x, y), \tag{5.11}$$

where u' and v' are the perturbations in the oncoming uniform flow due to the presence of the magnetic dipole. We now look for an asymptotic solution as a perturbation expansion for small values of the parameter Re. First, we expand the vorticity ω_z (and similarly the velocity components u, v and the stream function ψ) as a series in integral powers of Re, namely,

$$\omega_z = \omega_z^{(0)} + Re\ \omega_z^{(1)} + Re^2\omega_z^{(2)} + \mathcal{O}(Re^3), \tag{5.12}$$

where the super-index denotes the order of the approximation. Solutions of this sort become increasingly accurate as the perturbation parameter, Re, is smaller

than 1.

Zeroth-order solution

In steady state, the vorticity equation (5.6) at order $\mathcal{O}(Re^0)$ satisfies

$$\nabla_\perp^2 \omega_z^{(0)} = Ha^2 \left(j_y \frac{\partial B_z^0}{\partial y} \right). \tag{5.13}$$

The solution of eq. (5.13) is

$$\omega_z^{(0)}(x, y) = -\frac{\eta \, y \, Ha^2}{4\pi^2 (x^2 + y^2)}. \tag{5.14}$$

Observe that $\lim_{x,y\to\infty} \omega_z^{(0)} = 0$, and that although solution (5.14) presents a singularity at the origin, it reproduces correctly the vorticity in the neighborhood of the origin. The velocity field can be obtained through the stream function ψ, defined as $u = \partial\psi/\partial y$, $v = -\partial\psi/\partial x$. By expanding the stream function, at zeroth order in Re, it satisfies

$$\nabla_\perp^2 \psi^{(0)} = -\omega_z^{(0)}. \tag{5.15}$$

The solution for the stream function is

$$\psi^{(0)}(x, y) \approx y - c \frac{Ha^2 \, y}{32 \, \pi^2 (x^2 + y^2)}, \tag{5.16}$$

where the velocity components are obtained from the equations

$$u^{(0)} = \frac{\partial\psi^{(0)}}{\partial y}, \quad v^{(0)} = -\frac{\partial\psi^{(0)}}{\partial x}. \tag{5.17}$$

First-order solution

At $\mathcal{O}(Re^1)$, the vorticity satisfies the equation

$$\nabla_\perp^2 \omega_z^{(1)} = u^{(0)} \frac{\partial\omega_z^{(0)}}{\partial x}. \tag{5.18}$$

The solution of eq. (5.18) is found to be

$$\omega_z^{(1)}(x, y) = -\frac{x \, y \, Ha^2}{16\pi \, (x^2 + y^2)^2}. \tag{5.19}$$

Correspondingly, the stream function at this order is found to be

$$\psi^{(1)}(x, y) = c \frac{x \, y \, Ha^2}{192\pi \, \eta \, (x^2 + y^2)^2}. \tag{5.20}$$

Second-order solution

At $\mathcal{O}(Re^2)$, the vorticity satisfies the equation

$$\nabla_\perp^2 \omega_z^{(2)} = u^{(1)}\frac{\partial \omega_z^{(0)}}{\partial x} + u^{(0)}\frac{\partial \omega_z^{(1)}}{\partial x} + v^{(1)}\frac{\partial \omega_z^{(0)}}{\partial y} + v^{(0)}\frac{\partial \omega_z^{(1)}}{\partial y}. \tag{5.21}$$

The solution of eq. (5.21) is

$$\omega_z^{(2)}(x,y) = \frac{y(Ha^4 + 48\ Ha^2\pi^2(y^2 - 3x^2))}{6144\pi^3\ (x^2 + y^2)^2}. \tag{5.22}$$

Correspondingly, the stream function at this order is

$$\psi^{(2)}(x,y) = \frac{y\ Ha^2(Ha^2 - 288\ \pi\ y^2 + Ha^2\ln(x^2 + y^2))}{24576\pi^2\ \eta\ (x^2 + y^2)}. \tag{5.23}$$

Finally, the approximate solution reads

$$\psi = \psi^{(0)} +\ Re\ \psi^{(1)} +\ Re^2\psi^{(2)}. \tag{5.24}$$

The velocity components can be calculated from (5.24) by using the definition of the stream function. Note that the term $\mathcal{O}(Re^0)$ introduces induced effects, while terms $\mathcal{O}(Re)$ and $\mathcal{O}(Re^2)$ originate small non-linear effects. As in previous studies [27, 73], the analytical solution (5.24) diverges for $r \to 0$ and $r \to \infty$, which reveals a problem intrinsic to the approximation $Re < 1$. Nevertheless, as it is shown in Figure 5.2, solution (5.24) provides a suitable approximation of the flow in the neighborhood of the magnetic source and is able to reproduce the complex patterns with several vortices found in numerical studies at larger values of Re. As observed, the analytical solution reproduces qualitatively the flow patterns with two, four and six vortices as the Reynolds number is slightly increased for a fixed Hartmann number, namely, for $Ha = 35$ and $Re = 0.01$ ($N = 1.2 \times 10^5$), $Re = 0.12$ ($N = 1.0 \times 10^4$) and $Re = 0.9$ ($N = 1.3 \times 10^3$), respectively. To the best of our knowledge, this is the first analytical solution that reproduces the four and six vortices flow patterns. It results interesting that this complex structures produced by the magnetic interaction can be found in such a wide range of Reynolds numbers. Although, as it will be shown from the numerical simulation, stronger inertial effects modify the particular structure of the flow patterns.

5.3   Three-dimensional numerical solution

We now proceed to simulate numerically an electrically conducting and incompressible Newtonian fluid flowing through a duct of rectangular cross-section. Figure 5.3 shows the considered physical model where a uniform flow interacts with a magnetic obstacle in a rectangular cross-section duct with the same dimensions as in the experiment reported by Domínguez *et al.* [45], namely: 85.8 cm in the streamwise x-direction, 8.0 cm in the spanwise y-direction and 1.0 cm in the z-direction.
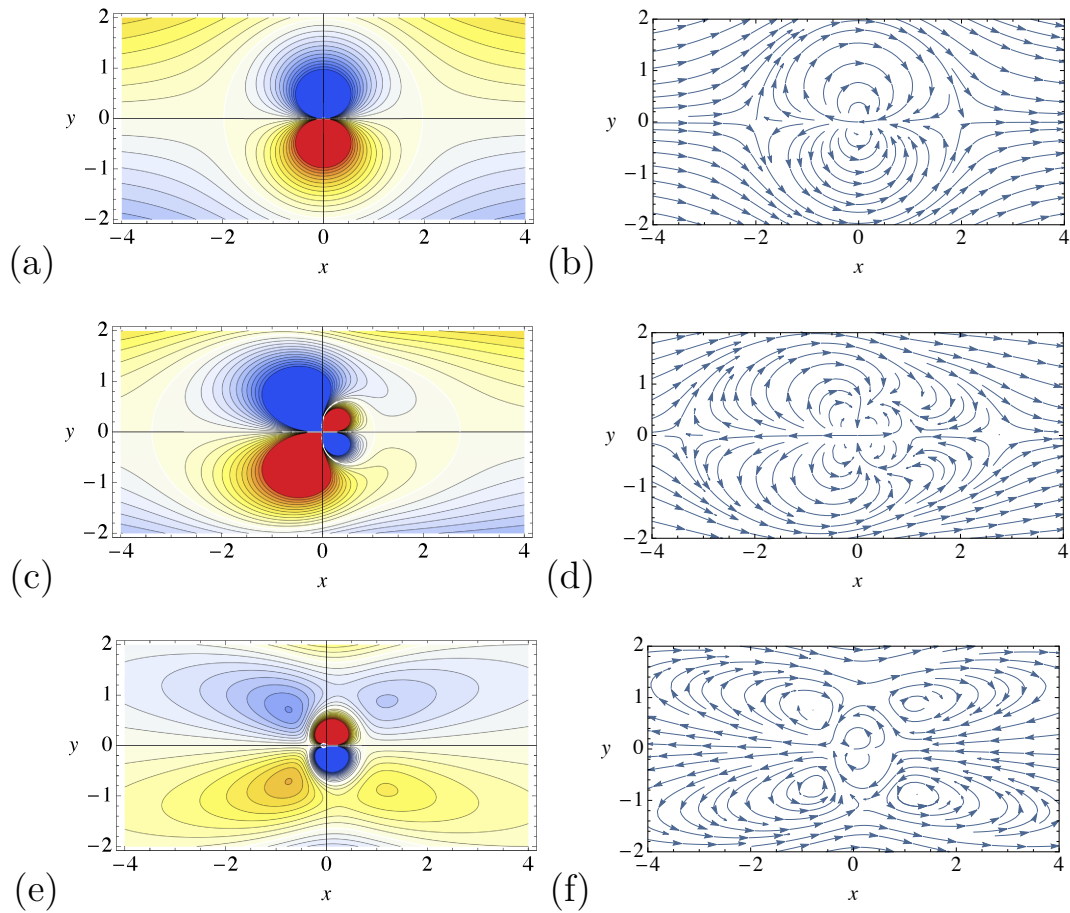
Figure 5.2: Analytic solution, eq. (5.24), for the creeping flow past a magnetic point dipole. Left column: Stream lines. Right column: Velocity fields. (a,b) $Re = 0.01$. (c,d) $Re = 0.2$. (e,f) $Re = 0.9$. In all cases $Ha = 35$.

Since the set of equations (2.23) - (2.26) that govern the MHD flow is strongly coupled, it has to be solved simultaneously using an iterative procedure based on the finite volume method. We used a structured, Cartesian grid with a sufficiently fine refinement. The computations were performed by dividing the computational domain into a grids of 1.9^6 and 2.5^6 CVs by considering a coarser and a finer mesh respectively, looking for a suitable grid that properly resolve the set of equations that govern the MHD flow and reproduce experimental results under the same conditions. In fact, no substantial changes were found by testing the different grids. Most of the computations were performed using streamwise grid size of $\Delta_x = 0.14$, meanwhile the grid sizes in the cross-section were $\Delta_y = 0.03$ and $\Delta_z = 0.005$. In turn, the time step was $\Delta t = 10^{-3}$. Given that experimental data are publicly available for specific configurations, we chose the mesh that showed good concordance when compared to experimental data.

The three-dimensional applied magnetic field is modeled using the equations provided in the book by Furlani [65] that are presented in Chapter 2, which give the full three-dimensional field distribution generated by a rectangular permanent magnet.
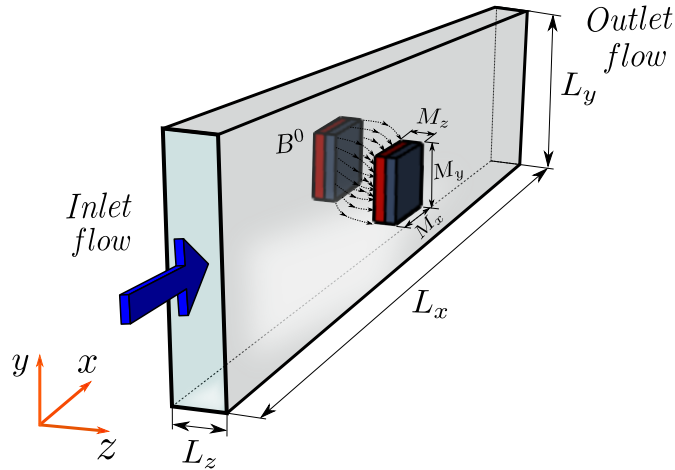
Figure 5.3: Physical model. A uniform liquid metal flow interacts with a magnetic obstacle in a rectangular cross-section duct.

Figure 5.4 shows the distribution of the intensity of the component B_z^0 of the applied magnetic field at the mid-plane of the duct when two magnets are superposed with a separating distance of 31 mm.
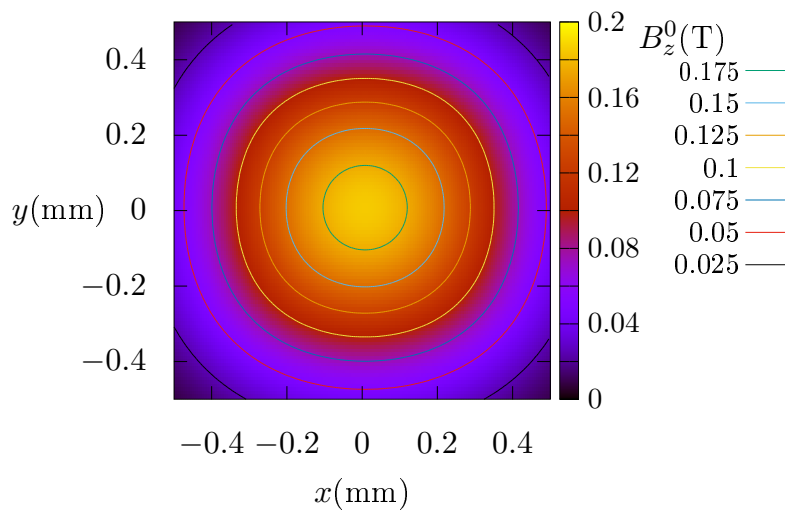

Figure 5.4: Distribution of the intensity of the applied magnetic field at the center of the duct $(Bz_{max} = 0.185$ T) considering the two-magnet arrangement with a gap of 31 mm between them for the numerical simulation.

In addition, to solve the governing equations, appropriate boundary conditions are established:

- No-slip condition at all solid walls $\boldsymbol{u} = 0$.

- At the inlet of the duct a uniform flow is imposed $u = 1, v = 0, w = 0$.

- At the outlet of the duct homogeneous Neumann boundary conditions on the velocity components were imposed.

- To guarantee electrically insulating walls, the normal component of the induced current was set to zero at all walls, which implies that the normal gradient of the electric potential is zero at the walls, $\frac{\partial \phi}{\partial n} = 0$.

Numerical simulations were performed using a node of the local Ehecatl cluster at IER-UNAM.

Before presenting the comparison of the numerical simulation with the experimental results provided by Domínguez *et al.* [45], we have to clarify an important point, namely, that the characteristic length scale used in the present numerical study differs from that used in [45]. Dominguez *et al.* [45] used the hydraulic diameter as a length scale in the Reynolds number while the separation between the Hartmann walls (those normal to the main component of the magnetic field) was used to define the Hartmann number. In contrast, in the present numerical study the side length of the square magnet was used consistently as a characteristic length scale for both Reynolds and Hartmann numbers, as well as for the normalization of the coordinates. Due to this fact, the values of the dimensionless parameters reported in [45] have been rescaled to be consistent with the characteristic length used in the present numerical simulation.

5.4   Comparison of numerical simulation with experimental data

Figure 5.5 shows a map of the axial velocity component, u, in the $x - t$ space, for the vertical position $y = 12.7$ mm. This kind of map is provided by the UDV technique. Figure 5.5(a) corresponds to the experimental results reported by Domínguez *et al.* [45] obtained with UDV for $Ha = 190$ and $Re = 4068$. In turn, Figure 5.5(b) corresponds to the full 3D numerical simulation for the same Hartmann and Reynolds numbers. In both figures, a zoom is provided for a better comparison between numerical and experimental results. Since the magnetic obstacle is located at $x = 0$, it can be observed the braking of the flow shown as a reduction of the axial velocity in the neighborhood of the obstacle, as well as the increase of velocity downstream the obstacle.

In fact, it can be observed from experimental results that the axial velocity just upstream the magnetic obstacle is reduced (red-purple vertical strip at -50 mm $< x < 0$mm) and then it increases in the region 0 mm $< x < 150$ mm. The inclined, red and purple parallel strips in the region $x > 170$ mm indicate the transit of a periodic perturbation in time for a fixed point in space, or in space for a snapshot. As noticed in Domínguez *et al.* [45], this velocity pattern is consisted with vortex shedding with an approximate characteristic time of the order of 1 s. On the other hand, the numerical results show that the axial velocity is reduced just after the magnetic obstacle (red-purple vertical strip at 0 mm $< x < 50$
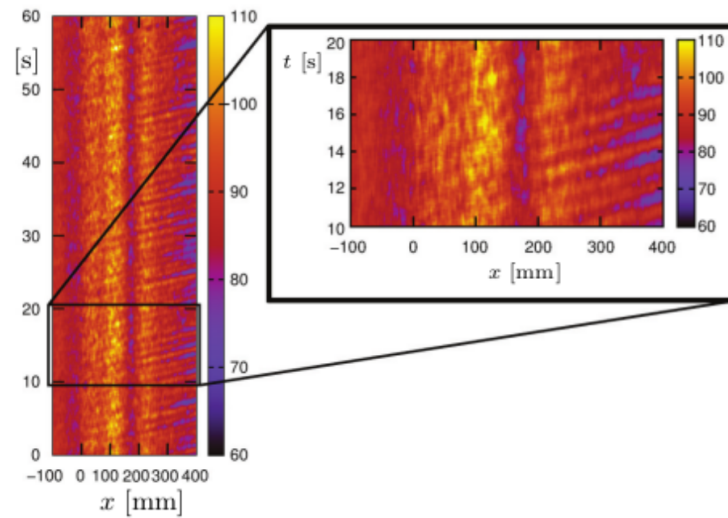
(a) Map of the axial velocity u in the (x,t) space. UDV experimental observations for $Ha = 190$, $Re = 4068$ for $y = 12.7$. (Domínguez *et al.* 2015).
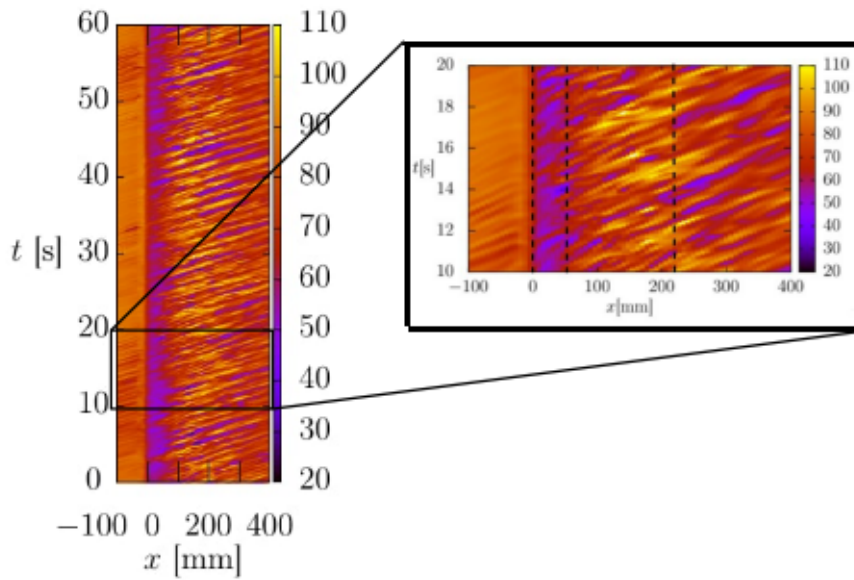
(b) Map of the axial velocity u in the (x,t) space. Fully 3D numerical simulation for $Ha = 190$, $Re = 4068$, $y = 12.7$ mm.

Figure 5.5: Axial velocity u.

mm), then it increases in the region 50 mm $< x <$ 215 mm. The inclined, red and purple parallel strips in the region $x >$ 215 mm indicate in a more marked way the appearance of a periodic perturbation, as observed in the experimental case.

We now examine in more detail the experimental results presented in [45] with the aim of comparing them with numerical results. Firstly, we analyse three cases, where the strength of the magnetic field is kept constant so that $Ha = 190$, while the inertia of the fluid, controlled by the Reynolds number, varies, taking the values $Re = 1800$, 4000 and 7200, that is, $N = 20, 9$, and 5, respectively. To perform a first comparison between the results obtained with the numerical simulation and the experimental results presented in [45], we plot time-series of the streamwise velocity u. The monitoring location is situated downstream the magnetic obstacle, at $(x, y) = (15, 0.5)$, which is located at the edge of the wake, where fluctuations of velocity are significant. In addition, we introduce the parameter $\mathcal{A}$ defined as

$$\mathcal{A} = u - \langle u \rangle, \tag{5.25}$$

where $\langle u \rangle$ is the average streamwise velocity at a fixed point over a time interval τ, so that just the change of the u component of the velocity with respect to its average is quantified. Figure 5.6 shows the time series of the u component for the three cases previously mentioned where colored lines correspond to numerical results (blue color for $N = 20$, green color for $N = 9$ and salmon color for $N = 5$), while the experimental data reported by Domínguez *et al.* (2015) is plotted with black color. The superposition of the numerical results on the experimental data show that the numerical simulation reproduces the experimental streamwise velocity with the same order of magnitude. Figure 5.7 shows the time-series of the parameter $\mathcal{A}$ for the same cases, again superposing the numerical results on the experimental results, following the same color code. Note that the velocity fluctuations are significantly more intense yet the amplitude of the oscillation of the monitored variable show a good concordance despite is clear that for the largest Reynolds number, differences between both methods (numerical and experimental) shows more pronounced.
In order to depict the effect of the oscillations in the velocity time series, the experimental study also reports the use of the parameter L^2, which is mathematically defined as

$$L^2 = \frac{1}{\tau} \int_0^\tau \mathcal{A} d\tau. \tag{5.26}$$

The parameter L^2 is a function of the Hartmann and Reynolds numbers only or, in other words, it is a function of N, and indicates the average of the square of the amplitude of the axial velocity oscillation with respect to its average value in the interval τ which is related to the kinetic energy of the vortices in the wake [45]. The time-series are carried out over a time interval of 200 seconds. In Figure 5.8(a) numerical results (in red) and experimental results (in blue) for the parameter L^2 are shown as a function of the Reynolds number. The lines accompanying the points are interpolations made to better observe the trends. Numerical results show a good agreement with the behavior of the parameter L^2 reported experimentally.
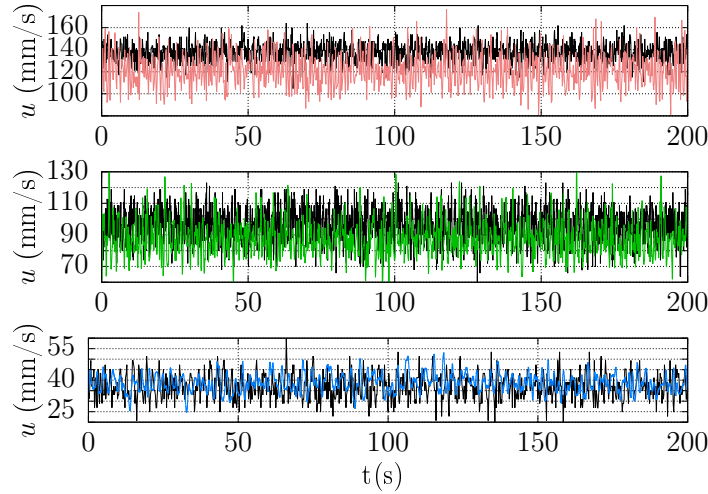
Figure 5.6: Time-series of the streamwise velocity component u. First row: $Re = 7200$ ($N = 5$). Second row: $Re = 4000$ ($N = 9$). Third row: $Re = 1800$ ($N = 20$). Black and color lines denote experimental observations and numerical simulations, respectively. For all cases, $Ha = 190$.

Figure 5.7: Time-series of the parameter $\mathcal{A}$. First row: $Re = 7200$ ($N = 5$). Second row: $Re = 4000$ ($N = 9$). Third row: $Re = 1800$ ($N = 20$). Black and color lines denote experimental observations and numerical simulations, respectively. For all cases, $Ha = 190$.
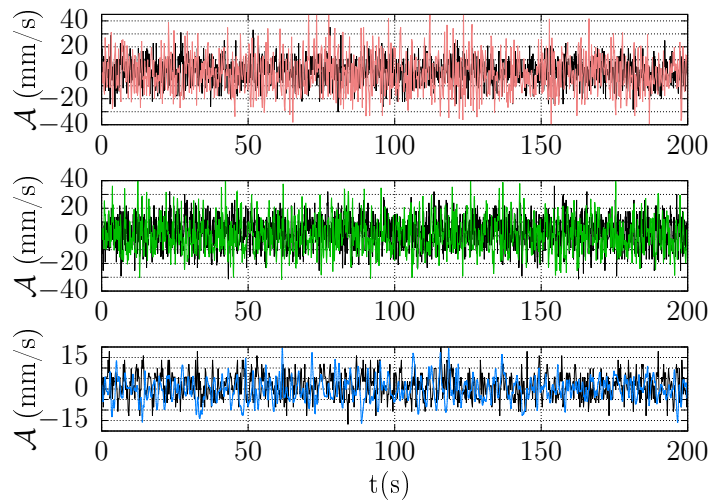
The fact that the curve first rises and then decreases in a finite range of Reynolds numbers is related to the amount of kinetic energy in the flow, which varies depending on the interaction of Lorentz, viscous, and inertial forces. At lower Reynolds numbers, the fluid exhibits lower kinetic energy due to the predominance of Lorentz forces, which act as an obstacle that the fluid surrounds, although there are localized effects of important MHD interactions occurring in the core of the magnetic obstacle, which are discussed later. However, as inertial forces gain importance and compete with Lorentz forces, at an interaction parameter of approximately $Re = 3000$ ($N = 12$), the parameter L^2 increases, indicating a transition to flow dynamics with greater fluid oscillations. A maximum is located around $Re = 5000$ ($N = 7$). As Re increases further, the Lorentz forces are overwhelmed by inertia, leading to reduced fluid oscillations reflected decreasing values of the L^2 parameter.

Additionally, the frequency of the velocity time-series was calculated via Fast Fourier Transform (FFT). Figure 5.8(b) shows both the frequency obtained numerically and experimentally at different Re numbers, where linear regression trend lines fitted to the results of each procedure are also presented. The correlation coefficient R^2 has a value greater than 0.9, indicating a strong correlation, and revealing that the frequency of the streamwise velocity in the fixed point grows in the range $0.2 - 1.5$ as the Re number increases. Even though the numerical model shows a global good agreement with the experimental results, there are slight differences between them. When direct comparisons are made between the numerical and experimental results, it is found that for $Re < 4000$, the comparison is quite close with a relative error of less than 10%. As can be seen by the trend lines in Figure 5.8, the separation between them becomes more pronounced as the Reynolds number increases which is attributed to the numerical code limitations.

Once the code has been successfully validated with realistic experimental data, the complex flow structure and detailed information concerning the dynamics of the flow past the magnetic obstacle can be reconstructed through visualization tools which cannot be achieved experimentally due limitations in measurement systems and data acquisition.
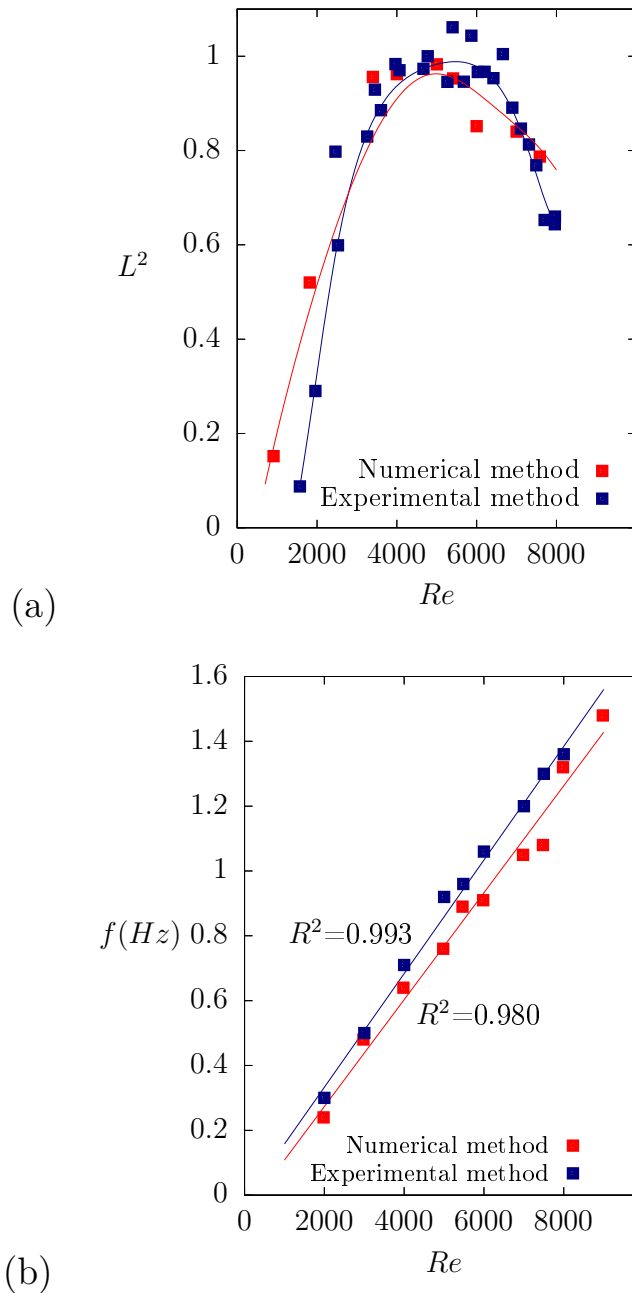
Figure 5.8: (a) Experimental and numerical values of the parameter L^2 as a function of the Reynolds number. (b) Frequency of the streamwise velocity obtained experimentally and calculated numerically as a function of the Reynolds number.

5.5   Three dimensional flow structures

In this Section, we examine the three-dimensional flow structures obtained numerically with similar conditions as those studied experimentally, that is, we keep the same geometry and the same applied magnetic field, therefore, in what follows the Hartmann number is still fixed at $Ha = 190$. We focus the attention at the inner magnetic region of the flow as well as the magnetic obstacle wake, in particular, how

flow patterns are affected when the balance between inertia and magnetic force is changed. Furthermore, since numerical simulation offers the advantage of discerning details that cannot be observed experimentally due to practical limitations, our goal is to compute additional relevant data such as the friction factor that may be of importance for a prospective work.

5.5.1   Magnetic obstacle flow structures

We will now show the three-dimensional flow structures that take place when the liquid metal flows in the duct under the localized magnetic field. With the aim of clarifying how the flow occurs, we first show projections on the mid-plane of the duct of the electric potential and the induced electric currents that originate the Lorentz force that slows down the oncoming flow. Fig. 5.9(a) shows the electric potential map in the mid-plane of the duct, $z = 0$, superimposed with the electric current density vector field for $N = 36$ and $Re = 1000$. Note that one current loop is formed upstream the localized magnetic field and two current loops are formed downstream of it, part of the loops being inside the "shadow" of the magnets. Note also that the main components of the current density point in the negative y-direction, so that they give rise to a Lorentz force that points mainly in the negative x-direction and brakes the flow. In Fig. 5.9(b), the vector field of the Lorentz force that opposes the flow is shown in the mid-plane $z = 0$, superposed to the colored scalar field of the magnitude of the streamwise velocity component, u. We can observe that the intensity of the force is relevant mainly in the area projected by the magnets which is about one third of the transversal area, that corresponds to a constrainment factor $\kappa = 0.36$. In turn, the map of the streamwise velocity component shows a negative velocity in the region where the Lorentz force opposes the oncoming flow, while at the edges of the magnetic obstacle the flow surrounds the region where the Lorentz force is stronger. Fig. 5.9(c) shows isolines of the electric potential in the neighborhood of the magnetic obstacle, where the closed contour paths can be identified.

Let us now look how the velocity profiles are affected due to the presence of the magnetic obstacle. Fig. 5.10 shows the profiles of the streamwise velocity component, u, at the mid-plane $z = 0$, for different Reynolds number, namely, $Re = 500, 3000$, and 4000. Fig. 5.10(a) shows the profile of u as a function of the spanwise coordinate y at a fixed axial position ($x = 0$). These M-shaped profiles manifest the action of the Lorentz force in the central region where a reduction in the velocity is observed. In fact, the lowest velocity is found for the smallest Reynolds number ($Re = 500$). However, as the Reynolds number increases, inertial forces become more relevant and the blockage effect caused by the magnetic obstacle becomes weaker. As a result of mass conservation, the fluid surrounds the magnetic obstacle and reaches higher velocities in regions where the Lorentz force is negligible. Fig. 5.10(b) shows the profile of u as a function of the streamwise coordinate, x, at the center line $y = 0$. A drastic reduction of the velocity is observed as it encounters the magnetic obstacle (centered at the origin) and even negative values of the velocity are found which implies a reverse flow. Further downstream, the velocity increases again in a smooth way for the
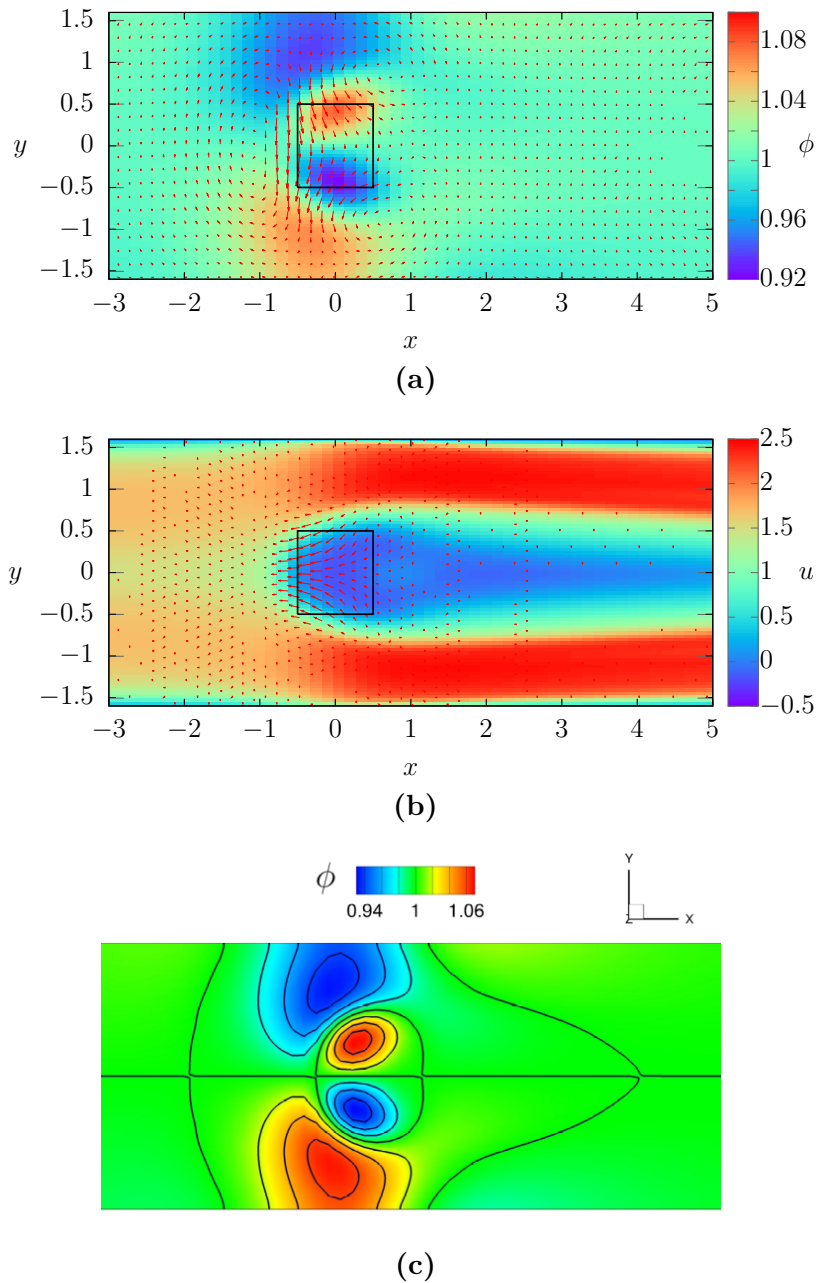
(a)

(b)

(c)

Figure 5.9: (a) Electric current vector direction and electric potential, overlapped at the mid-plane, $z = 0$, (b) Lorentz force blockage to the axial velocity and (c) isolines of electrical potential form closed loops within the core of the magnetic obstacle. $Re = 1000$, $N = 36$.

lowest Reynolds number ($Re = 500$) where the Lorentz force dominate. For larger Reynolds numbers the streamwise velocity oscillates as result of flow instability and vortex shedding. Notice that the highest amplitude of oscillation occurs at different x locations for $Re = 3000$ and 4000.
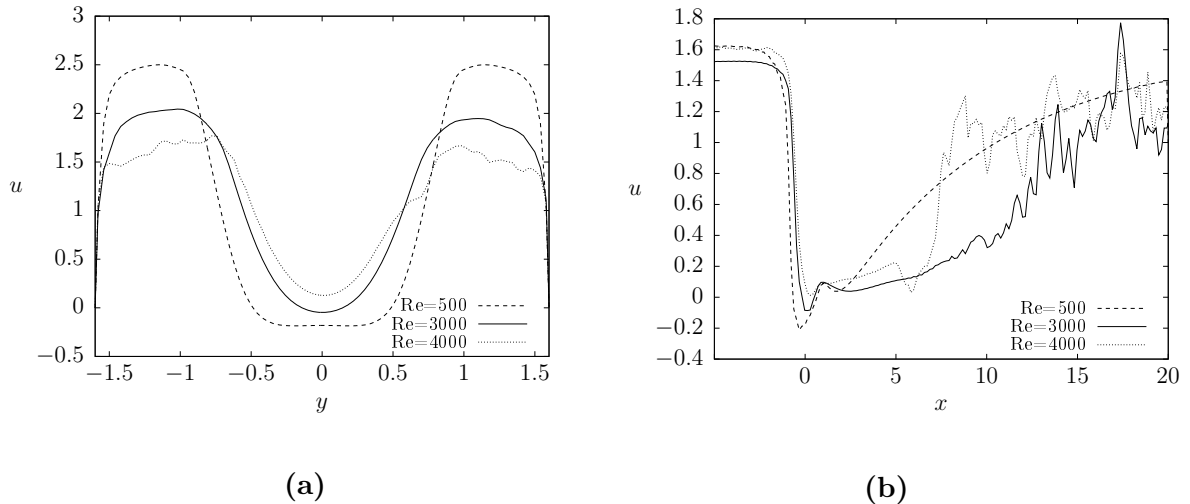

(a)   (b)

Figure 5.10: Velocity profiles of the streamwise component, u, at the mid-plane ($z = 0$) for different Reynolds numbers, (a) as a function of the spanwise coordiante, y, at $x = 0$, and (b) as a function of the streamwise coordiante, x, at $y = 0$. $Ha = 190$.

We now explore the three-dimensional flow patterns for different flow conditions. Due to the Lorentz force that brakes the flow when passing through the localized magnetic field, quasi-stagnation or recirculation regions are formed that give rise to different vortex patterns according to the flow conditions. In order to obtain a deeper insight of the flow pattern transition, we analyse the steady flows as the Reynolds number varies for a fixed Hartmann number, which is equivalent to vary the interaction parameter N. In Fig. 5.11 we show, in the first column, the three-dimensional path of the induced electric current, and in the second column, the isometric view of the streamlines colored with the magnitude of the streamwise velocity, calculated numerically for $Ha = 190$ and different Reynolds numbers, namely, $Re = 25$ ($N = 1444$), $Re = 300$ ($N = 120$), $Re = 600$ ($N = 60$), and $Re = 1000$ ($N = 36$). Note that in the four cases the three-dimensional paths of the induced electric currents are intricate, revealing a complex behavior that manifest the fact that the closing of electric current loops is necessarily three-dimensional and that the current can close through boundary layers attached to the walls [74]. In fact, upstream the magnetic obstacle a single electric current recirculation can be identified in all cases, while downstream two smaller current loops are observed in Fig. 5.11(b,c,d), and further downstream a kind of helical current paths are observed in these cases. For the smallest Reynolds number (Fig. 5.11(a)), the current paths present a pattern that differs from the other cases. Since the induced electric currents determine the magnetic forces by the interaction with the applied non-uniform magnetic field, it

may be expected that the three-dimensional Lorentz force distribution is also complex. Nevertheless, the flow patterns observed on the right column are not produced only by Lorentz forces but also by the action of viscous forces and most importantly by inertia. For the lower Reynolds number explored, $Re = 25$ ($N = 1444$), the flow past a magnetic obstacle produces two vortices that remind the attached vortices observed in the flow past a cylinder when Re is not too high. Curiously, the same pattern of two vortices is also found when the inertia is increased substantially, namely, $Re = 300$ ($N = 120$). As the convective effects are increased even further ($Re = 600$, $N = 60$), a second pair or vortices appears downstream of the first pair, forming a four vortex pattern. If the convective effects are increased even more ($Re = 1000$, $N = 36$), the so-called six vortices pattern is obtained. This is a complex behavior of the flow first reported in [29] with magnets of rectangular geometry, while in the case presented here, the same flow pattern was obtained with square magnets.

Continuing the evolution pattern shown previously, Figure 5.12 presents the three-dimensional path of the induced electric current in the first column and an isometric view of the streamlines colored by the magnitude of the streamwise velocity in the second column. These results are obtained numerically for $Ha = 190$ and Reynolds numbers of $Re = 3000$ ($N = 12$), $Re = 5400$ ($N = 7$), and $Re = 800$ ($N = 4.5$). Notably, the recirculation of electric current undergoes changes as inertial forces intensify, leading to a decrease in the closing effect of electric current loops which can be observed within the progression showcased in the left-hand column on Figure 5.12(e,f,g). The right-hand column shows flow patterns influenced by Lorentz, viscous, and inertia forces, indicating that as the interaction parameter decreases to $N = 12$, the pattern of two vortices is recovered, while for further decrease of N (increase of Re), the quasi-stationary patterns disappear, giving way to a flow transition characterized by wake oscillation without vortices.

5.5.2 Flow structure in the far wake

We now analyse the time-dependent flow patterns, comprising the near and far wakes, as the Reynolds number varies for a fixed Hartmann number. Figure 5.13 shows the instant streamtracers in a region including the beginning of the magnetic obstacle till the outlet of the duct, for four different Reynolds numbers, $Re = 500$, 2300, 3000 and 8000 (corresponding to $N = 72$, 16, 12 and 4.5, respectively), and $Ha = 190$. Through these patterns it is possible to explore the flow evolution as the inertia increases, while the strength of the Lorentz force remains constant. Figure 5.13(a), corresponding to $Re = 500$ ($N = 72$), displays a steady flow with vortices in the magnetic region and the near wake. Although it can not be discerned at this scale, a six vortex pattern is obtained, while the streamtracers display straight trajectories in the far wake. In this case, magnetic forces clearly dominate over inertia. As the Reynolds number increases to $Re = 3000$ ($N = 12$), Figure 5.13(b) shows that the flow is deflected in the spanwise direction, and oscillations are observed in the far wake. By increasing the Reynolds number to $Re = 5400$ ($N = 7$), in Figure 5.13(c) the oscillations of the streamtracers start in the near wake with a higher amplitude. However, for $Re = 8000$ ($N = 4.5$), Figure 5.13(d),
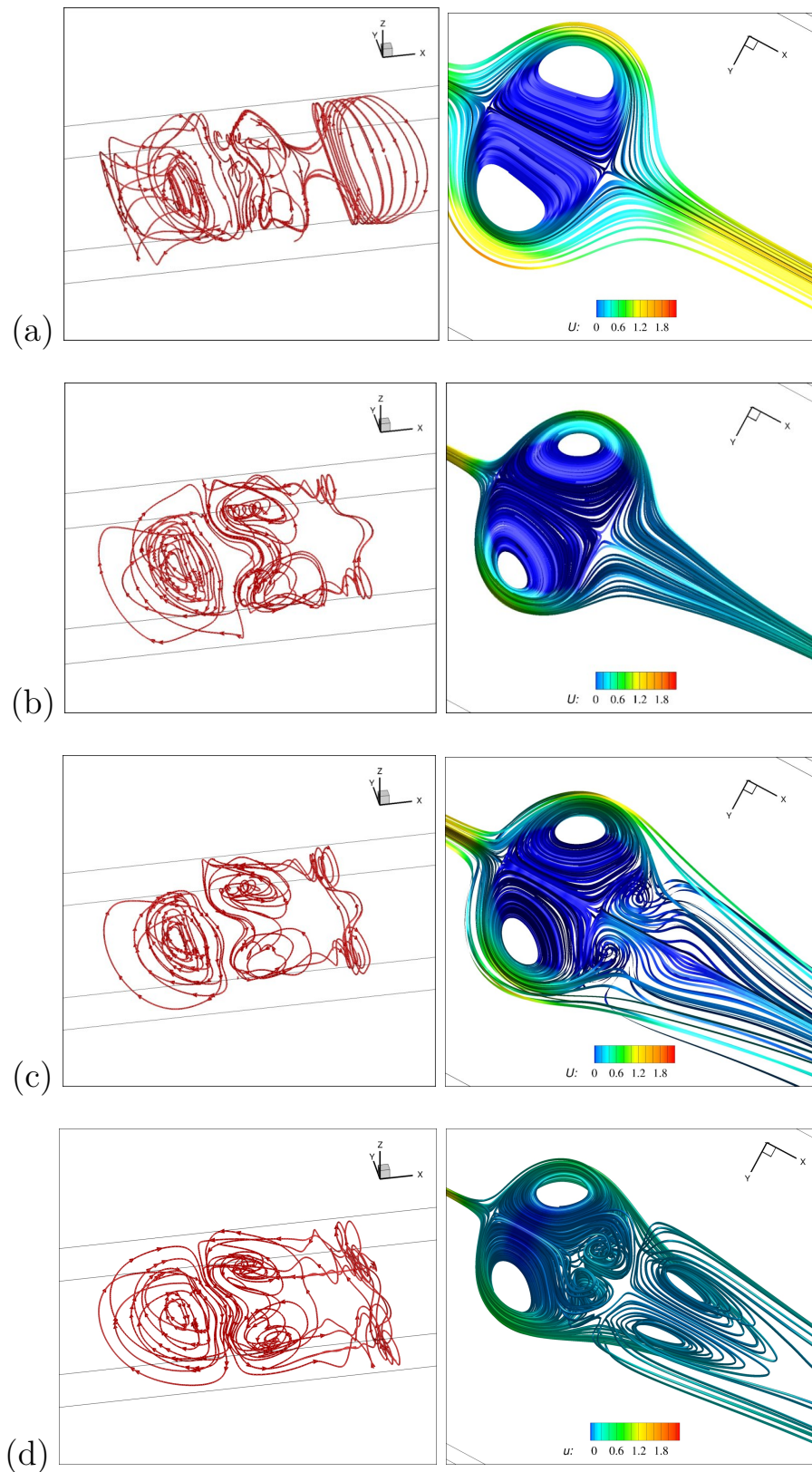
Figure 5.11: Isometric view of electrical current and instant streamlines of two flow patterns zoomed in the magnetic region for $Ha = 190$. (a) Two vortices patterns obtained for the parameters with values $Re = 25$ ($N = 1444$) and (b) $Re = 300$ ($N = 120$). (c) Four vortices pattern attained with $Re = 600$ ($N = 60$). (d) Six vortices pattern attained with $Re = 1000$ ($N = 36$).
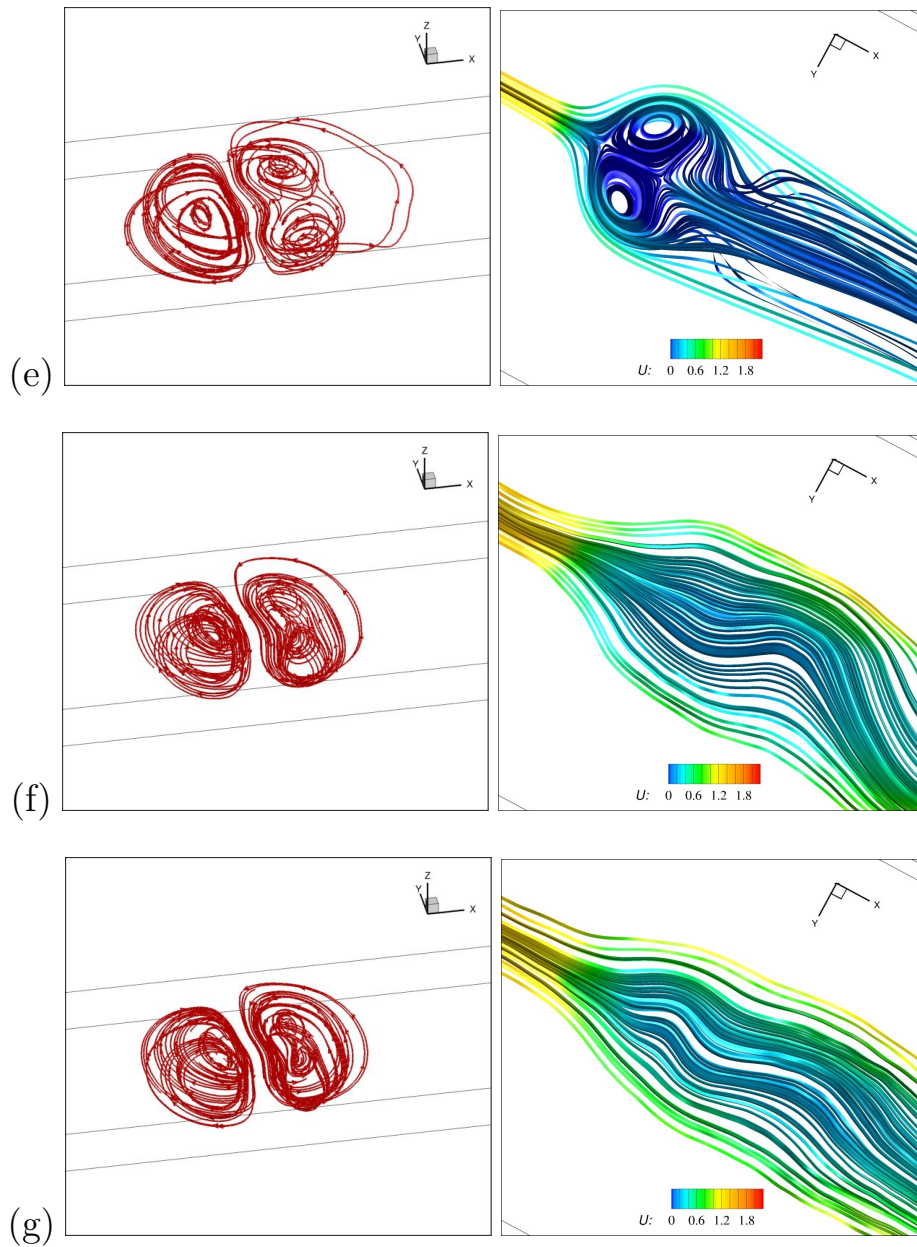
Figure 5.12: (e) Flow pattern obtained with $Re = 3000$ ($N = 12$). (f) Flow pattern obtained with $Re = 5400$ ($N = 7$), and (g) $Re = 8000$ ($N = 4.5$) colored with axial flow velocity.

the amplitude of oscillations reduces and the flow seems to be *relaminarized.* While in the latter case the inertia overwhelms the magnetic forces, for $Re = 5400$, the Lorentz forces compete with inertia and promote higher disturbances in the flow.

The evolution of the magnetic obstacle wake is shown in Figure 5.14 through the examination of the magnitude of the streamwise, u, and the spanwise, v, velocity components for different values of Re and N with $Ha = 190$. Figure 5.14(a) displays a symmetrical behavior of the streawise component with respect to the axis located at $y = 0$ for $Re = 1000$ and $N = 36$. In the case where the magnetic forces are important and the flow remains without oscillations in the wake. In turn, the streamwise velocity is reduced to a minimum in the center of the duct in the magnetic field region, which is a manifestation of the deceleration of velocity due to the magnetic blockage effect caused by the Lorentz force produced in the central part of the domain. In some cases, a reverse flow may also be produced. To comply with mass conservation, fluid jets with high velocity are formed at the sides of the start of the magnetic obstacle wake. The spanwise component has limited effect on the core of the magnetic obstacle, as can be seen in Figure 5.14(b). For $Re = 3000$, $N = 12$ (Figure 5.14(c,d)), intermittent regions for the velocity components are initiated at $x = 10$, and the spanwise velocity component (v) has higher intensity in the vicinity of the wake. As Re increases and N decreases, the wake begins to oscillate, reaching a maximum deflection for $N = 7$ (Figure 5.14(e,f)), where the flow is deflected in the spanwise direction causing the wake to oscillate. In the case of high Re and small N, 8000 and 4.5, respectively, see Figure 5.14(g,h), the wake begins to relaminarize and the oscillations are suppressed. The spanwise velocity component decreases along the duct as the Reynolds number increases, indicating a decrease in fluid agitation.

A similar flow development has been reported in other studies of flow past a magnetic obstacle, such as in [43], which demonstrates the formation of a core of the magnetic obstacle as N increases. On the other hand, in the experimental study by Sasami [42] with a dragging magnet that allows the visualization of the bulk flow in the free surface, shows that as the Reynolds number increases, vortex cores tend to disappear or, at least on this scale, vortices are no longer observable and only attached vortices remain. This behavior agrees with the streamtracers reported in Figure 5.13 from our numerical simulation, where the deflection of the streamtracers decreases from a critical point. It is noteworthy that the flow patterns shown in Figure 5.14 are not completely disrupted due to the dimensionless parameters used, even though the duct is relatively narrow in the z-direction and the constrainment factor, which relates lateral size of the magnet exposed to the oncoming flow to the size of the duct in the transverse section, is large, $\kappa \approx 1/3$. This suggests that friction plays a significant role in the formation of the wake. However, when the constrainment factor is larger, the flow near the walls tends to be more fluctuant and the vortex patterns become unstable, a phenomenon that can be attributed to shear stress [41]. Nevertheless, the results are in agreement with previous studies and support the finding that there is a critical value of N for a given magnetic field strength, beyond which the flow becomes increasingly agitated as the interaction
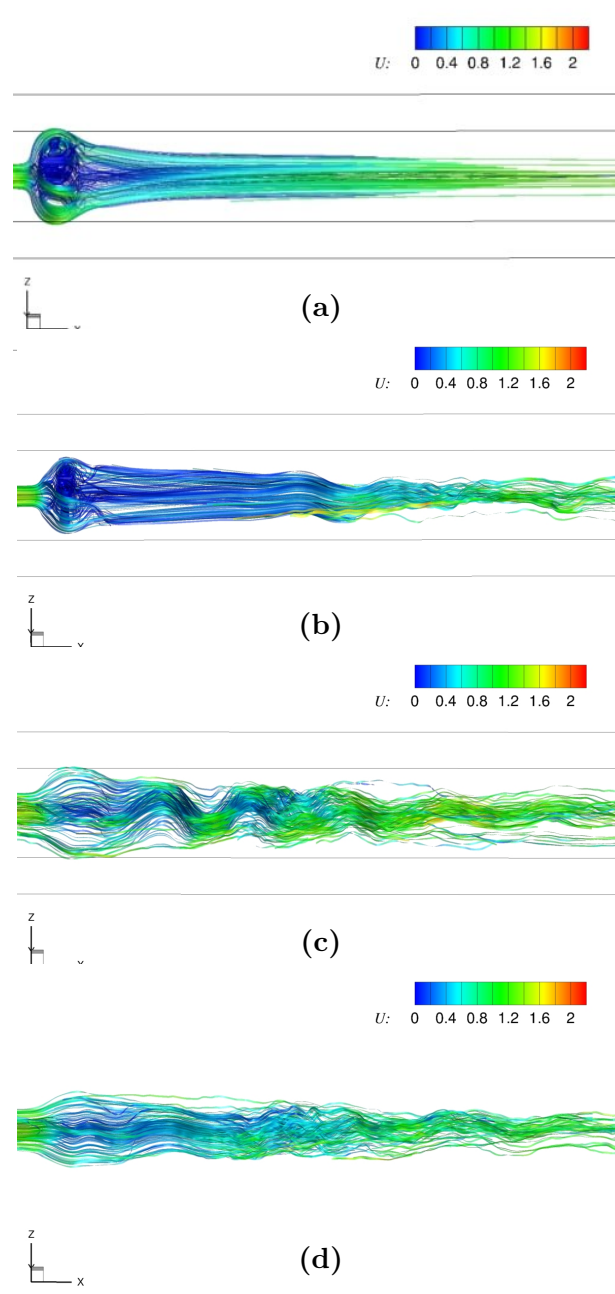
Figure 5.13: Instantaneous streamlines for fluid particles initially located upstream the magnetic obstacle at $x = -1.0$. (a) Three-dimensional view $Re = 500$, $N = 72$. (b) $Re = 3000$, $N = 12$, (c) $Re = 5400$, $N = 7$. (d) $Re = 8000$, $N = 5$.

parameter N decreases and the Reynolds number increases.

It is illustrative to calculate and explore the behavior of the friction factor since usually gives practical information in flows where solid obstacles are present, particularly when the obstacles are used for heat transfer enhancement [75]. The friction factor is the dimensionless expression of the shear stress on the obstacle and mathematically is defined as

$$f_c = \frac{2\tau_w}{\rho U^2}, \quad \tau_w = \rho\nu\frac{\partial u}{\partial n}, \tag{5.27}$$

where τ_w in the shear stress at the wall of the obstacle. The friction factor characterizes the drag force on a solid body. In fact, it is also possible to calculate this coefficient when the drag is due mainly to an electromagnetic force [76], and reported observations indicate that this coefficient is large when the flow feels a strong magnetic force while an increase of velocity flow leads to the reduction of the coefficient magnitude. A similar behavior is observed with the friction factor presented in Figure 5.15 where it was calculated at the mid-plane $z = 0$. Figure 5.15(a) shows the local friction factor along x-direction at $y = 0$ for different Reynolds number in a range $1400 < Re < 8000$ which correspond to $N = 25, 14, 12, 4.5$. Note that for $Re \leq 3000$, the magnetic force predominates in the region where the magnetic obstacle is located and a marked increase in f_c is obtained. When $Re = 8000$ and the inertia becomes more important, the increase in f_c in the region of the obstacle is not observed while further downstream the magnetic obstacle, the friction factor begins to oscillate. A time and space averaged friction factor in the plane $z = 0$ for 200 time units is shown in Figure 5.15(b) as a function of the Reynolds number to depict its effect in global terms. A clear tendency to decrease is obtained as Re increases, which shows the relevance of the magnetic force to substantially increase the friction factor for smaller values of Re, or equivalently, for smaller values of the interaction parameter N.

5.6   Final comments

In this chapter, we have presented numerical results obtained with the fully three-dimensional code based on the finite volume method developed in this thesis. In particular, we have compared the numerical results against data obtained in an experiment reported in [45] where the liquid metal flow past a magnetic obstacle was explored. In this experimental device, the constrainment factor of the obstacle was $\kappa \approx 1/3$, which has been shown in previous research to be large for the optimal development of a wake. In addition, the gap ratio was also $h \approx 1$, which is significant in terms of the influence of wall friction on the wake development. The first step was to validate the numerical simulation by comparing the results against the available experimental data that comprises the variation of the interaction parameter in the range $4.5 < N < 72$. In this comparison, the intensity of the magnetic field was held constant so that the Hartmann number was fixed, $Ha = 190$. In this
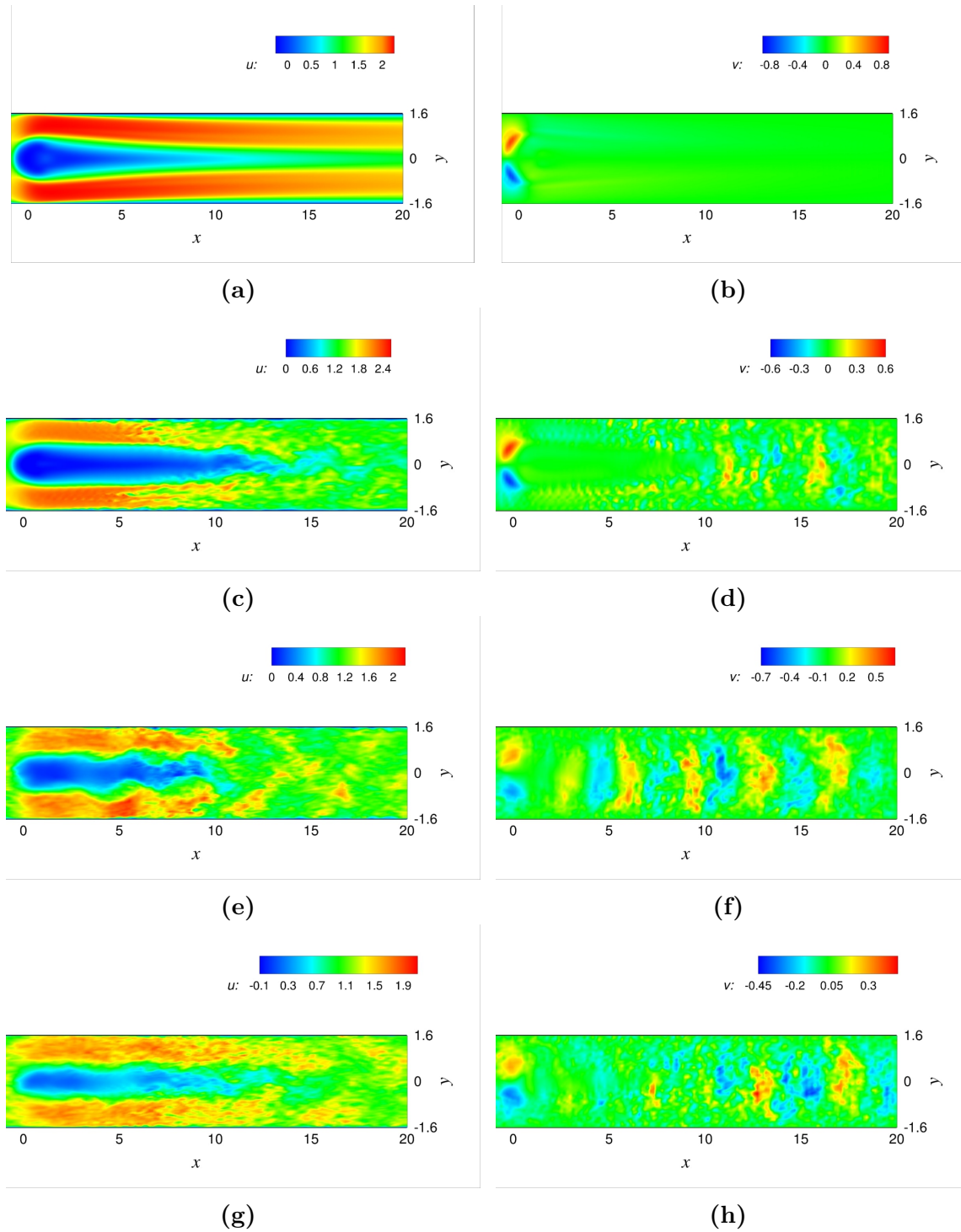
Figure 5.14: Instantaneous velocity maps of the streamwise, u (left column), and the spanwise, v (right column), velocity components at the central plane $z = 0$, for different values of the parameters Re and N: (a, b) for $Re = 1000$ and $N = 36$, (c,d) for $Re = 3000$ and $N = 12$, (e,f) for $Re = 5400$ and $N = 7$, (g,h) for $Re = 8000$ and $N = 4.5$.
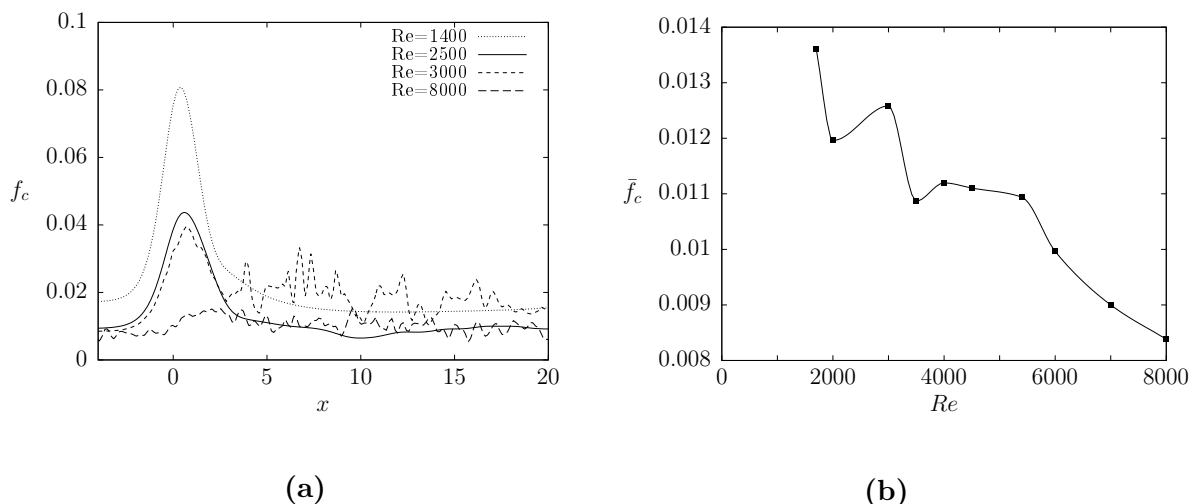
Figure 5.15: Profiles for the (a) local friction coefficient for different Reynolds numbers and (b) the global friction coefficient as a function of Reynolds number.

conditions, the variation of N corresponds to the variation of the Reynolds number in the range $500 \leq Re \leq 8000$. The simulation showed good agreement with the experimental data, as demonstrated by the comparison of time-series and the frequency of streamwise velocity oscillations, as well as the L^2 parameter, which provides information about the kinetic energy of the flow and the amplitude of the deflection of the streamwise velocity.

Taking into account that the error of the experimental measurements was of approximately 8%, the relative error between the numerical and experimental data is around 10.5%. This error decreases to around 4% for large values of N, but as N decreases, the relative error increases up to a maximum of 17%. Thus, the numerical code developed is able to accurately reproduce experimental results within the specified range.

The second objective of this chapter was to examine the three-dimensional characteristics of the flow through numerical simulations in order to gain a deeper understanding of the flow dynamics that cannot be observed experimentally. Our simulations revealed that the vortex patterns produced by the magnetic obstacle in the center of the duct are dependent on the Reynolds number or correspondingly on the interaction parameter. In fact, the transition of the flow patterns reveals a two-vortex pattern for the lower Reynolds number explored which evolved to patterns with four, six, and again two vortices as Re increases, and eventually flow patterns without vortices were obtained for sufficiently high Re. This transition reflects the interaction between inertia and Lorentz forces and the fact that the former overcomes the latter when Re is high enough. The transition in the flow patterns was complemented with the three-dimensional electric current paths that determine the magnetic force. A noteworthy fact is that the analytical solution performed is capable of reproducing some of these flow patterns. Our results also showed that the flow patterns can transit from stable to unstable, including turbulent burst patterns near the wake edge. As N decreased, we observed that the deflection of the flow di-

minished farther downstream due to the dominance of inertial forces. Furthermore, we identified a critical interaction parameter ($N \approx 7$) that results in a maximum deflection of the wake. We also showed that the friction coefficient is approximately inversely proportional to the Reynolds number.

Numerical simulation of heat transfer in MHD duct flows

In this chapter,[‡] we investigate the heat transfer characteristics of liquid metal duct flows using different configurations of magnetic obstacles placed near a wall under different thermal boundary conditions. In analogy with the use of solid obstacles [77], the effect on the heat transfer of the constrainment and gap ratios of the magnetic obstacles is explored. Results from a full 3D simulation are contrasted with two-dimensional and quasi-two-dimensional models.

6.1 Influence of different electric wall conditions in a 3D duct flow subjected to a heat flux

In this section, we investigate the influence of different electric wall conditions on heat transfer in a rectangular duct flow using Galinstan as working fluid, characterized by a Prandtl number of $Pr = 0.053$. The dimensions of the duct (in dimensionless units) in the $x - y - z$ directions are $35 \times 7.2 \times 1$. The study focuses on a flow with a Reynolds number of 700 through a specific magnet arrangement comprising three pairs of magnets positioned close to one of the side walls, as depicted in Figure 6.1. The square magnets are located at coordinates $(x = 10, y = 1.5)$, $(x = 13, y = 1.5)$ and $(x = 16, y = 1.5)$. A constant and uniform heat flux,$Q = 1$, is applied to the lateral wall.
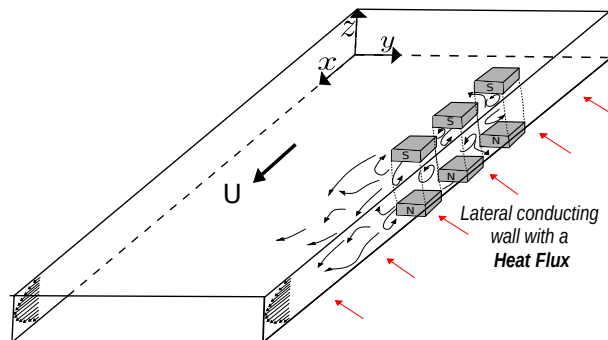

Figure 6.1: Sketch of the duct flow subjet to a heat flux at a lateral conducting wall.

[‡]Part of the content of this chapter is based on the paper: Solano-Olivares, V., Pérez-Barrera, J., Cuevas, S., & Figueroa, A. Numerical study of liquid metal MHD flows in ducts for heat transfer enhancement. Proc. 11th PAMIR International Conference - Fundamental and Applied MHD, pp. 12-16. July 1 − 5, 2019, Reims, France.

To determine the influence of the electrical conductivity of the walls on heat transfer, we analyze the temperature distribution on the wall subjected to a constant and uniform heat flux. Figure 6.2 shows the variation of wall temperature at the heated wall along the x coordinate at $z = 0.5$ and $y = 7.2$ for $Ha = 75$, $Re = 700$ ($N = 8$). The lines represent different electric wall conditions, namely, a duct with all four walls electrically conducting; combined walls, that is, the heated wall is electrically conducting and the other walls are electrically insulated; insulated walls where the four walls are electrically insulated; and the purely hydrodynamic case in absence of magnetic field where the electric conductivity of the walls is not relevant. Observations from this results show that the purely hydrodynamic case exhibits the lowest wall temperature, whereas the MHD cases with conducting walls, either combined or purely conducting, display higher temperatures, while the case with insulating walls presents wall temperatures slightly lower. This suggests that the presence of magnetic obstacles enhances the heat transfer compared to the hydrodynamic case without magnets. Given that the duct is slender and the Reynolds number relatively low, the magnetic obstacles cause deceleration of the fluid and flow recirculation in the region where they are located, leading to efficient heat transport in the axial direction.
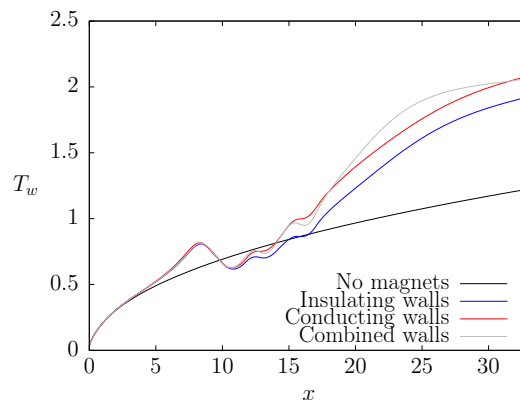

Figure 6.2: Temperature profiles on the heated wall with $Ha = 75$ and $Re = 700$ for different electric wall conditions.

In the following Section we aim to highlight the significance and reliability of different approximations, namely 2D, Q2D, and 3D models, for analyzing heat transfer in MHD flows with localized magnetic fields. We specifically investigate the differences between these approximations emphasizing strengths and limitations.

6.2   Effect of MHD flow dynamics on heat transfer in 2D, Q2D and 3D models

We now explore the flow of a liquid metal in an electrically insulating duct with high aspect ratio and uniform rectangular cross-section under different distributions of non-homogeneous magnetic field. Again, the working fluid is the eutectic alloy GaInSn ($Pr = 0.053$). At the entrance of the duct the liquid metal has a uniform velocity profile $u = 1$ and a constant temperature, T_0, while a constant heat flux is

applied along one of the side walls. To simulate the MHD flow through arrays of magnetic obstacles, 2D, Q2D and 3D numerical models are used in three particular cases. In all of them, magnets are located at the top and bottom of the duct near the heated wall and with their magnetization axis along the $z-$direction. In Case 1, only one pair of square magnets is considered, where the side length of the magnet is taken as the characteristic length, $L_c = M_x$. In Case 2 (see Figure 6.3), three pairs of square magnets of unit side length are used, spaced by a (dimensionless) distance $d = 2$ between their faces and separated a distance $G = 0.5$ from the heated wall. In Case 3, three pairs of rectangular magnets of dimensions 1×2 in the x and y directions are placed, with the same values of d and G, as in Case 2. In dimensionless units, the size of the duct is $35 \times 10 \times 0.4$ in the $x - y - z$ coordinates, respectively, and the center of the first magnet is located at $x = 10$. The constrainment factor and the gap ratio, defined as $k = M_y/L_y$ and $h = G/M_y$, respectively, are varied in the ranges $k = 0.1 - 0.2$, and $h = 0.25 - 0.5$. The 2D numerical model could be considered as a rough approximation of the flow of a very thin layer of fluid. The Q2D model improves the 2D model by considering the friction of the top and bottom walls introduced through an averaging of the dynamic equations along the $z-$direction. It is based on the assumption that the momentum transport is purely diffusive in that direction. Results of the 2D and Q2D approaches are compared with the fully 3D numerical model. The numerical solution of the MHD equations was carried out using ϕ-formulation.
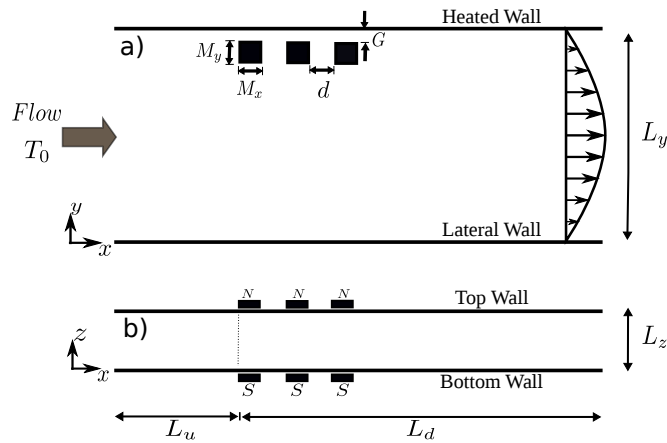

Figure 6.3: Sketch of the problem explored in Case 2. a) top view, b) lateral view.

The computational domain is divided in a uniform mesh of $220 \times 110 \times 200$. Four grid points are solved in the Hartmann layer which are sufficient for a reasonable resolution according to a study reported in [78]. At the duct walls no-slip condition is applied for the velocity and a constant value of the electric potential is set at all walls. At the entrance of the duct a uniform flow and temperature are imposed. At the outlet of the duct, the streamwise gradient of velocity and temperature are set to zero to satisfy fully developed conditions. A lateral wall is exposed to a

constant uniform heat flux whereas the other walls have a zero normal temperature gradient at the surface (thermally insulating walls). In all cases, the Péclet number and interaction parameter are fixed at $Pe = 7.95$ and $N = 16.6$, values chosen arbitrarily. The validation of the present code for the solution of the MHD flow and heat transfer problems has been performed by comparing against published numerical results under a local magnetic field and against analytical solutions [66]. Figure 6.4 shows the streamlines in the plane $x-y$ obtained in Case 3 for the different numerical models. For the 3D model streamlines are obtained at the central plane $z = 0.2$. The 2D model displays the largest mixing zone due to the absence of lower and upper wall confinement. Although clear differences are observed, Q2D and 3D models show similar flow patterns and, therefore, a close heat transfer behavior could be expected, although recirculation zones are less marked with the 3D model. In Figure 6.5(b) the velocity magnitude for the third case of the fully 3D model is shown with the parameters $Pe = 7.95$ and $Ha = 50$. In the region where the magnetic obstacles are present, the lowest velocity is found as can be observed in Figure 6.5(a) where the streamwise velocity component u is plotted as a function of y coordinate at positions $x = 8.98$ and $x = 15.03$. Figure 6.5(b) shows the magnitude of the velocity in the flow region where a considerable increase is observed in the area between the wall and the magnetic obstacles.

Figure 6.6 shows the temperature profile at the heated wall as a function of x coordinate at a long time instant ($t = 400$) for the three explored cases using the 2D, Q2D and 3D numerical models. Clear variations on heat transfer behavior among different models are observed. Although in all cases the temperature shows a steeper increase as the first obstacle is approached, the 2D model shows a continuous increase while Q2D and 3D models show a more localized temperature increment around the region where magnetic obstacles are placed. For the three models, the largest increase in temperature is found with Case 3 while the smallest one occurs for Case 1. Comparing the Q2D and 3D models, the maximum value for the wall temperature is approximately 26% higher in the Q2D model while at the end of the duct the difference is around 10%. It appears that the Q2D model tends to overestimate the friction effect of the walls and in the vicinity of the magnetic obstacles as well, causing a stronger braking in the flow and increasing the wall heat transfer. On the other hand, the 2D model greatly separates from the Q2D and 3D models. Although for Case 1 and 2 the constrainment factor and the gap ratio are the same ($k = 0.2$ and $h = 0.5$) the difference in the number of magnets in Case 2 causes a greater increase in the wall temperature. Case 3 where the constrainment factor is larger and the gap ratio smaller leads to very intense heat transfer manifested on the highest wall temperatures.

When considering conditions in which convective heat transfer effects are significant ($Pe = 7.95$) and Lorentz forces dominate over inertial effects ($N = 16.6$), the study revealed that higher constrainment factors and smaller gap ratios lead to enhanced heat transfer. The results suggest that the strategic use of localized magnetic obstacles, characterized by non-uniform magnetic fields, could potentially facilitate heat transfer enhancement.

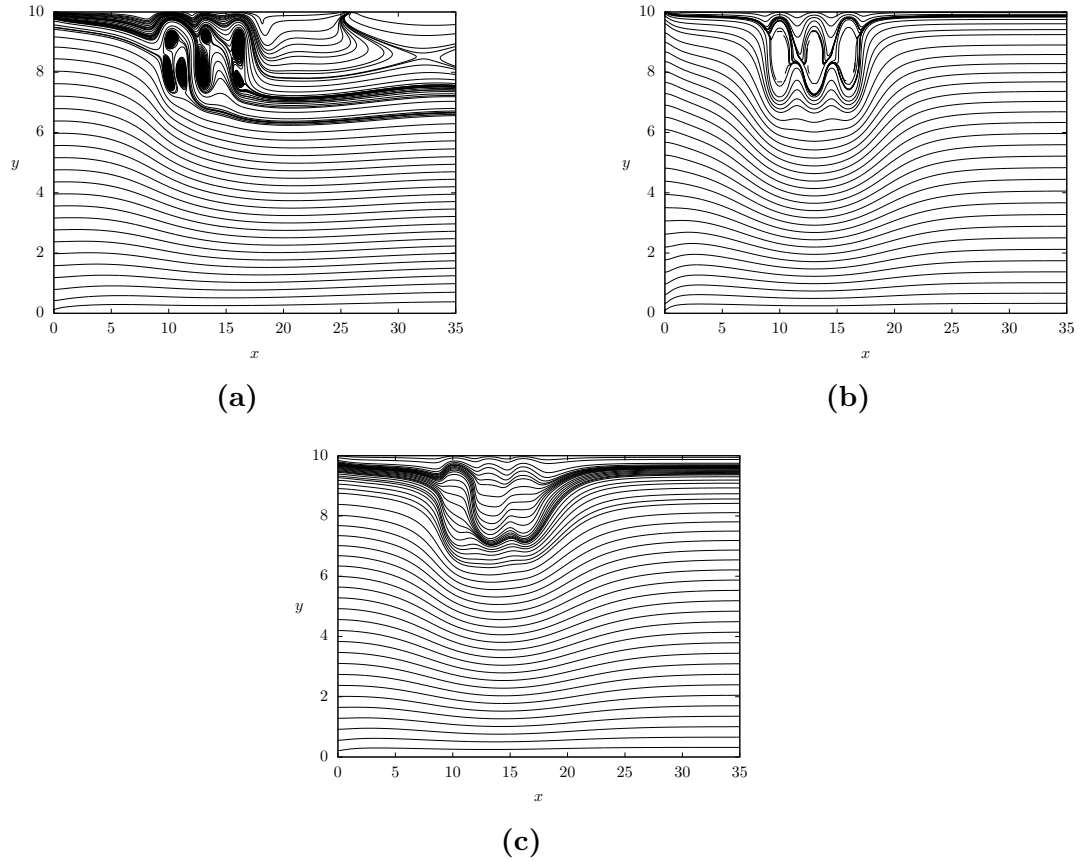In the next Section we lay the foundations for a complete study of heat transfer in

Figure 6.4: Instant streamlines obtained with (a) 2D, (b) Q2D and (c) 3D models for the magnet arrangement indicated for Case 3 with $Pe = 7.95$ and $Ha = 50$ at the central plane $z = 0.2$.
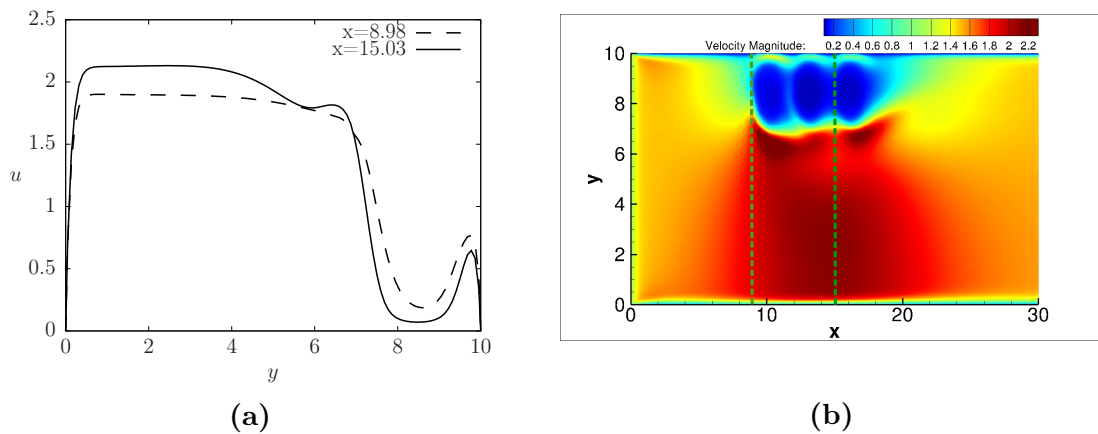

Figure 6.5: (a) Axial velocity profiles and (b) velocity magnitude for the fully 3D model of Case 3 with parameters $Pe = 7.95$ and $Ha = 50$.
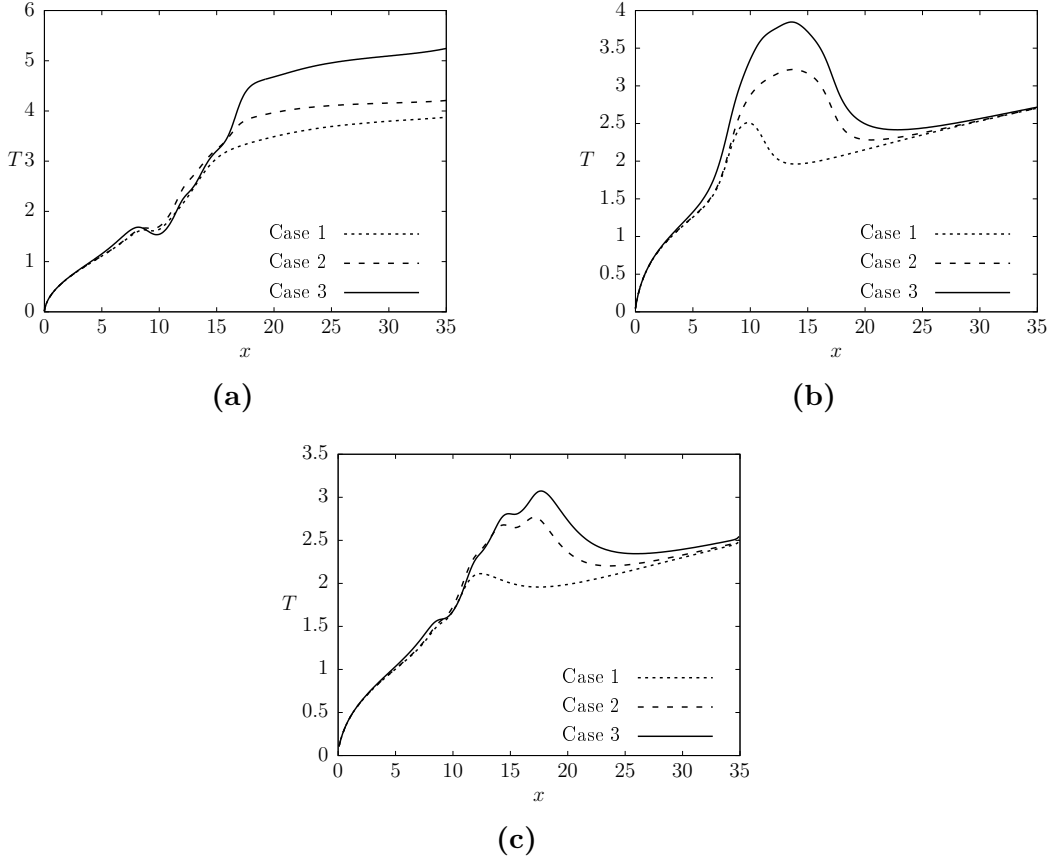
Figure 6.6: Temperature profiles on the heated wall as a function of the x coordinate for the three cases of magnet arrangements explored using (a) 2D, (b) Q2D and (c) 3D models.

a methodological way to optimize resources and obtain results with high reliability.

6.3   Heat transfer study in a MHD flow in a rectangular duct

To facilitate the computational process, we adopted a systematic approach in developing the numerical solution. Initially, we opted for a two-dimensional model, acknowledging its inherent limitations as discussed in a previous section. The significant increase in computational cost associated with a fully three-dimensional simulation further supported this decision. Notably, some modifications were implemented in this 2D approximation model compared to the previous case presented in Chapter 3, where we attempt to simulate a fin or baffle cut as typically used in heat exchangers but in a non intrusive way using a rectangular permanent magnet to produce a magnetic obstacle. To begin with, we use a square magnet to introduce additional arrays of magnetic obstacles within the domain to enhance heat transfer efficiency. One modification involved imposing a Poiseuille flow condition at the inlet of the duct as a boundary condition. This choice effectively reduced the computational domain required for resolving the transition from a plug flow $u = 1$. Furthermore, the implementation of Navier-Stokes solutions entailed the utilization of a non-uniform mesh, which allowed for enhanced refinement and therefore accuracy near the walls and the region containing the magnetic obstacle. The utilization of a non-uniform mesh needs the incorporation of a stretching function and the adjustment of discretized terms within the Navier-Stokes equations. Consequently, we embarked on the development of a refined 2D model as an initial step, and subsequently, we aimed to adapt the same problem to a comprehensive three-dimensional model.

6.3.1   First approximation with a refined 2D model

In this section, we investigate heat transfer in a liquid metal flow with a Prandtl number of $Pr = 0.053$. A duct with dimensions $x = 60$ and $y = 8$ is considered. A localized magnetic field is generated by a square-shaped permanent magnet, where $M_x = M_y$, with a unit length and a geometric center located at $x = 15, y = 1$. The magnet-wall distance is set to $G = 0.5$, as illustrated in Figure 6.7. The computational grid employed consists of 3.7×10^4 control volumes, with a spacing of $dx = 0.2$ and a minimum spatial step in the y coordinate of $dy = 0.03$ with a time step of $dt = 1 \times 10^{-3}$. The parameters used for this simulation are $Ha = 100$, $Re = 900$. With this resolution, considering the Shercliff layer thickness of $\delta_S = 0.1$, which is on the order of $Ha^{-1/2}$, four points are resolved.

We solve this problem using the Finite Volume Method with the ϕ-formulation. The dynamics of the flow are described by equations (2.23)-(2.26), which are solved to obtain the numerical solution. Perfectly conducting electrical walls are considered, with $\phi = 0$, meaning no variation in the electric field. The wall at $y = 0$ is subject to a constant temperature of $T = 1$. At the solid walls no-slip conditions are enforced,
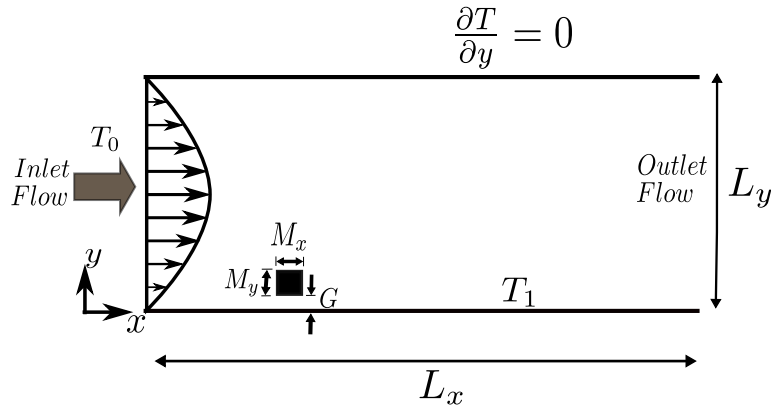
Figure 6.7: Sketch of the flow of liquid metal for the study of heat transfer with a two-dimensional approximation.

$u = 0$. At the duct inlet, a one-dimensional Poiseuille flow is imposed, which is obtained by solving the following equation:

$$0 = -\frac{dP}{dx} + \frac{1}{Re}\left(\frac{\partial^2 u}{\partial y^2}\right), \tag{6.1}$$

whose solution is

$$u(y) = -\frac{6}{L_y^2}(y^2 - L_y), \tag{6.2}$$

where L_y is the length of the duct in the y direction. This function yields a velocity profile with a flow rate of $Q = 1$. At the duct outlet, a zero-gradient condition for velocity is imposed, indicating a fully developed flow. For this study, a non-uniform grid is implemented in the y-direction to provide greater refinement in the region where the magnetic field is located (Figure 6.8). In this way, we increase the accuracy of the solution and capture in a better way details of the flow under study. The procedure for implementing this type of grid is described in the Appendix A.

We solve first the dynamics of the liquid metal flow with the parameters $Re = 900, Ha = 100$. Figure 6.9 shows the map of the v component of the velocity in the $x - y$ plane for this conditions. Due to the presence of the obstacle at $x = 15$, $y = 1$, near the wall located at $y = 0$, a marked variation of the spanwise velocity is observed from the point $x = 15$ and undergoes with drastic changes downstream the magnetic obstacle.
The Courant criterium that guarantees the numerical stability of the discretization schemes is defined as

$$CFL = u\frac{\Delta t}{\Delta x} < 1, \tag{6.3}$$

and imposes a constraint on the maximum time step, designed to ensure that the propagation velocity of disturbances within the mesh does not exceed one cell per time step. Deviation from this condition can result in the divergence of the
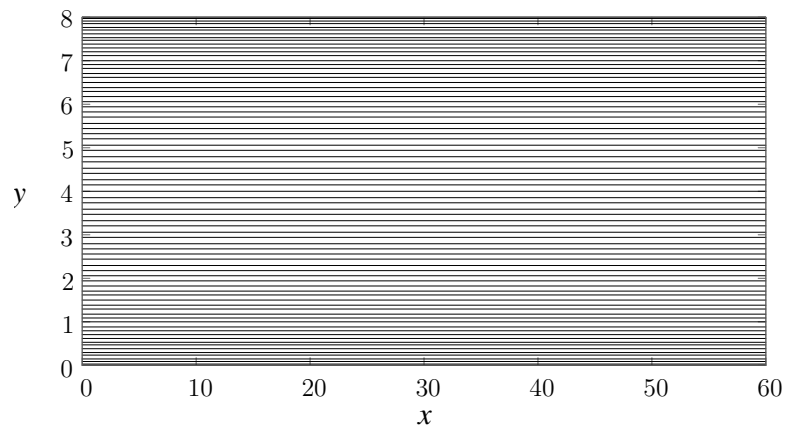
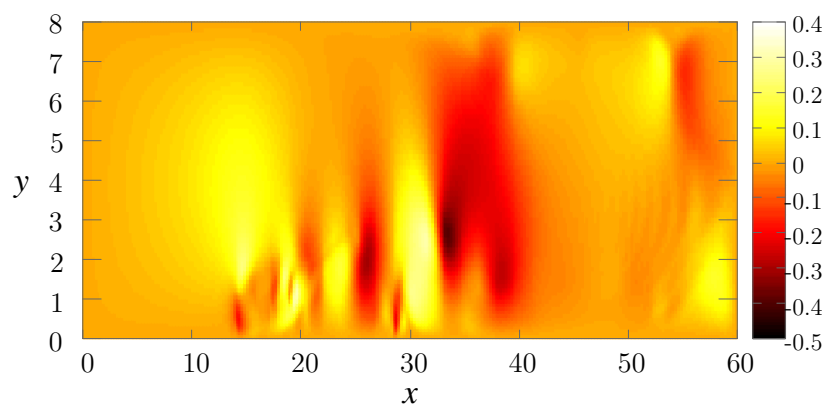Figure 6.8: Non-uniform spacing in the vertical direction used in the 2D grid for the numerical simulation.

Figure 6.9: Map of the v component of the velocity of a liquid metal flow in the presence of a localized magnetic field located at $x = 15$, $y = 1$ near the lateral wall at $y = 0$, obtained with the parameters $Re = 900, Ha = 100$.

numerical solution. The computed values of the Courant number confirm that in the $x - y$ plane at a given instant of time, maximum values of $CFL = 0.02$ are obtained in the intermediate region of the duct due to higher velocities. Near the walls, particularly the wall adjacent to the magnetic obstacle, the Courant number is lower. This is attributed to the no-slip condition and the deceleration of the flow imposed by the magnetic obstacle, resulting in lower velocities.

We now explore the friction coefficient, f_c, defined by (5.27), which is of interest for the global analysis of heat transfer enhancement [75]. In addition, we also analyse the local Nusselt number defined as

$$Nu_L(x,t) = \left. \frac{\partial T}{\partial y} \right|_w , \tag{6.4}$$

where the subindex w indicates evaluation at the wall. Figure 6.10 shows the local friction factor and the local Nusselt number at the wall ($y = 0$) at a given instant of time as a function of the x-coordinate, when the flow is subjected to the thermal boundary condition $T = 1$, for $Re = 900$ and $Ha = 100$. Both figures reveal the local variation that occur due to the presence of the magnetic obstacle. In Figure 6.10(a) the friction factor presents a positive peak value precisely at the location of the magnetic obstacle ($x = 15$), followed by oscillations with negative and positive values. In turn, Figure 6.10(b) shows an increase of the local Nusselt number at some positions which indicate a local heat transfer enhancement due to the stirring promoted by the obstacle.
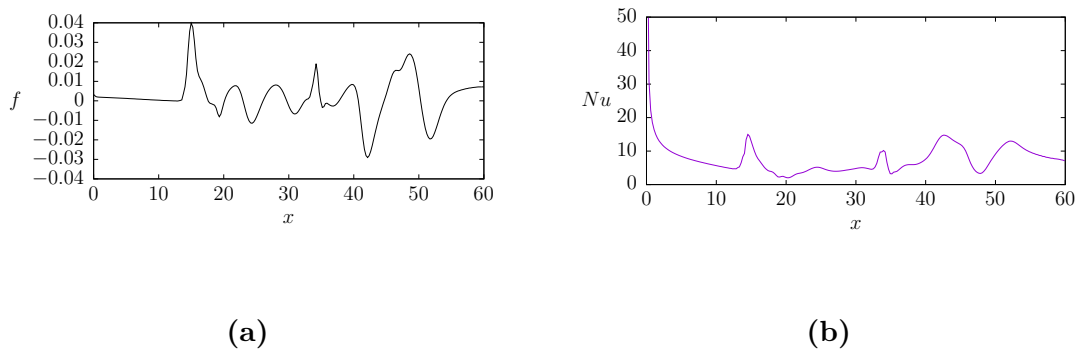

(a)   **(b)**

Figure 6.10: (a) Local friction coefficient and (b) local Nusselt number as a function of the x-coordinate for a flow under a constant temperature boundary condition, $T = 1$. $Re = 900$, $Ha = 100$.

Figure 6.11 presents a temperature map in the $x-y$ plane at the time instant $t = 500$, illustrating the influence of the velocity field on the temperature distribution with and without localized magnetic field. Figure 6.11(a) exhibits the numerical results for the purely hydrodynamic case with $Re = 900$, while Figure 6.11(b) depicts the numerical results for the MHD case obtained with parameters $Re = 900$ and $Ha = 100$. It is evident that the presence of a localized magnetic field induces fluid

agitation, resulting in enhanced heat transfer towards regions of lower temperature. By observing the color scale, it can be observed that a higher fluid temperature is achieved at a greater distance from the wall in the MHD case.
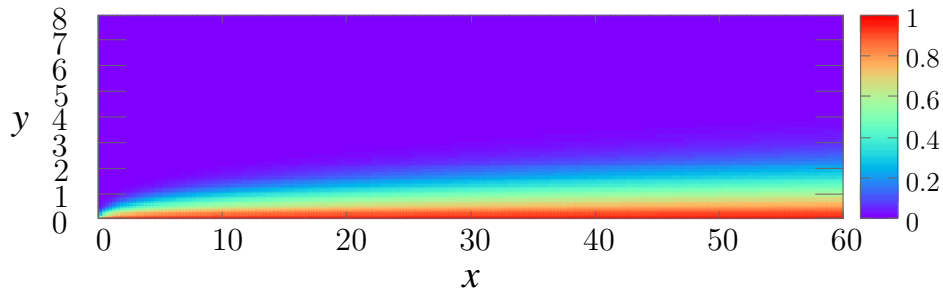
(a)
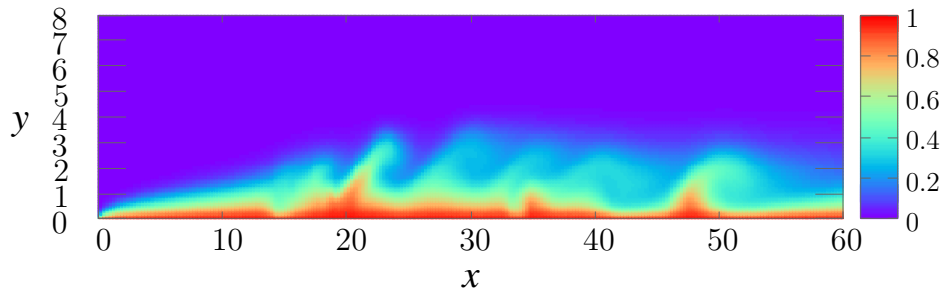
(b)

Figure 6.11: Temperature map at a given instant of time with a) $Re = 900$ and $Ha = 0$ b) $Re = 900$ and $Ha = 100$.

Time-series of temperature are shown in Figure 6.12 for the purely hydrodynamic case with $Re = 900$ and the MHD case with $Ha = 100$ and $Pe = 48$ at a fixed point located 10 units downstream of the magnetic obstacle, at $y = 1.5$, for 600 time units. It can be observed that the temperature exhibits oscillations in the MHD case, reaching values that are approximately twice the average temperature attained at that fixed point in the purely hydrodynamic case, which remains constant. This indicates that the fluid agitation caused by the presence of the magnetic obstacle enhances convective heat transfer. However, global parameters can provide more quantitative information in this regard. The global Nusselt number defined as

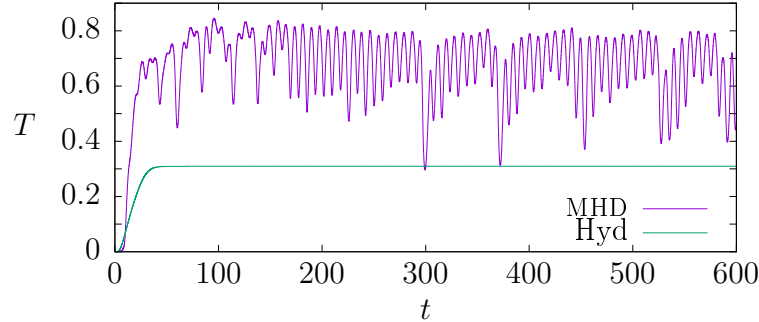$$Nu = \frac{1}{L} \int_0^L \overline{Nu}_L(x) dx, \tag{6.5}$$

Figure 6.12: Time-series of temperature at $x = 25$, $y = 1.5$ for (a) hydrodynamic case with $Pe = 48$ and (b) MHD case with $Ha = 100$ and $Pe = 48$.

obtained for the hydrodynamic case is $Nu_0 = 5.88$, while for the MHD case it is $Nu = 7.76$. Now, introducing these values in the thermal performance factor, η, as is usually done with mechanical swirl flow devices, defined as [52]

$$\eta = \frac{Nu/Nu_0}{(f_c/f_0)^{1/3}}, \tag{6.6}$$

where f_0 is the friction factor in the purely hydrodynamic case, we obtain $\eta = 1.25$ which represents a positive effect in heat transfer enhancement of 25% with the use of a localized magnetic obstacle. In the next section, we consider the extension of this problem to three dimensions.

6.3.2   Second approximation with a fully 3D model

In this Subsection, we address the same problem described in the previous section, but extended to three dimensions. The size of the rectangular duct in the $x - y - z$ dimensionless coordinates is $60 \times 8 \times 2$. A localized magnetic field is generated by two square-shaped permanent magnets $M_x = M_y$ with a unit length, externally to the walls, as shown in Figure 6.13. The thickness of the magnet in the z-direction is $M_z = 0.25$. The magnets have equal magnetization and a geometric center positioned at $x = 15, y = 1$, while the distance magnet-wall distance is set to $G = 0.5$. The computational grid used for this simulation consists of 3.7×10^4 control volumes, with a spatial step $dx = 0.15$, $dy = 0.1$, and $dz = 0.02$ with a time step of $dt = 1 \times 10^{-3}$. The parameters employed for this simulation are $Ha = 100$ and $Re = 900$ ($N = 11$). We use the Finite Volume Method to solve equations (2.23)-(2.26) (using the ϕ-formulation) that describe the dynamics of the flow. Perfectly conducting electrical walls are considered, with $\phi = 0$, assuming that the wall at $y = 0$ is subject to a constant temperature, $T = 1$. In addition, the no-slip condition is enforced in all solid walls. We assume a fully developed parabolic flow at the duct inlet to establish a more realistic condition and to reduce the numerical domain that would
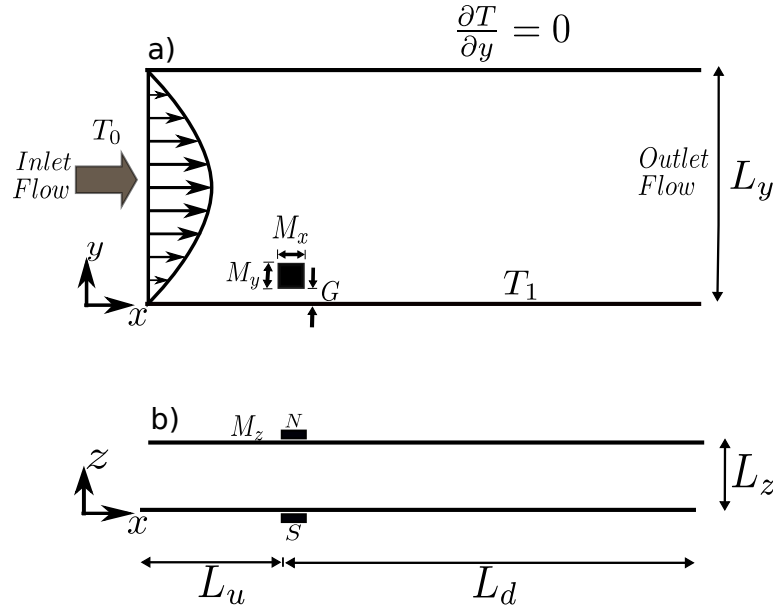
Figure 6.13: Sketch of the liquid metal flow in 3D.

imply to solve the development of the flow. Under the assumption of fully developed hydrodynamic steady flow in the $x-$direction, the Navier-Stokes equation is reduced to the form

$$0 = -\frac{dP}{dx} + \mu\left(\frac{\partial^2 u}{\partial y^2} + \frac{\partial^2 u}{\partial z^2}\right),$$

(6.7)

where u is the velocity component along the axis of the duct (x-direction). An analytical solution of (6.7) with no-slip conditions for a duct with a rectangular cross-section is given in reference [79] in the form

$$u(y,z) = \frac{-\pi^2 a}{2[-\pi a + 2h\tanh(\frac{\pi a}{2h})]}\Sigma_{n=0}^{\infty}(-1)^n\left\{1 - \frac{\cosh[(2n+1)\frac{\pi y}{h}]}{\cosh[(2n+1)\frac{\pi a}{2h}]}\right\}\frac{\cos[(2n+1)\frac{\pi z}{h}]}{(2n+1)^3},$$

(6.8)

where $-a/2 < y < a/2$ and $-h/2 < z < h/2$, a and h being the width and height of the duct.

Figure 6.14 shows an instant map of the magnitude of the v velocity component at the mid-plane $z = 1$, that corresponds to the flow of a liquid metal subjected to a localized magnetic field at the position $x = 15$, $y = 1$, near a side wall maintained at a constant temperature, $T = 1$. The results are obtained with the parameters $Re = 900$ and $Ha = 100$. The map of the v component of the velocity shows that the presence of the magnetic obstacle significantly alters the flow behavior, leading to increased agitation downstream the magnetic obstacle. The calculated velocity field is subsequently utilized to solve the energy equation and address the heat transfer problem.

The Courant number is also computed in our study, providing valuable insights. The
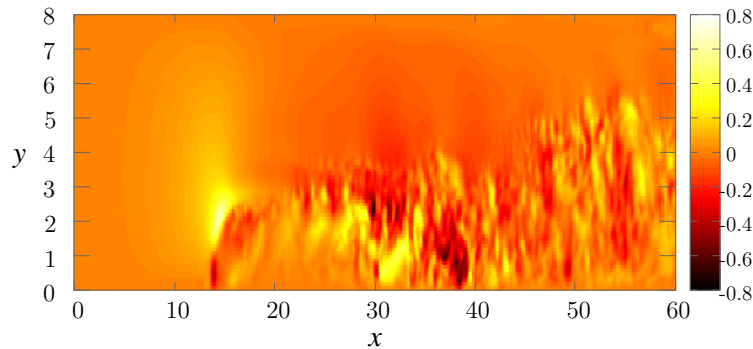
Figure 6.14: Map of the v component of the velocity at mid-plane of z coordinate with the parameters $Re = 900, Ha = 100$.

maximum values of the Courant number are observed in the center of the duct due to the high velocity prevailing in that region. Conversely, near the walls, the Courant number remains small due to the no-slip condition at solid walls. Additionally, significant velocity gradients occur in the interface between the magnetic zone and the free flow.

Figure 6.15(a) displays the local friction factor, while Figure 6.15(b) presents the local Nusselt number obtained with parameters $Re = 900$ and $Ha = 100$, at the side wall subject to a constant temperature. In contrast to the previous section, where a two-dimensional approximation was employed, the current study involves a three-dimensional solution, resulting in a surface plot in the $x - z$ plane. Numerical results correspond to the wall closest to the magnetic obstacle. Notably, there are pronounced peaks or oscillations that begin precisely at $x = 15$, corresponding to the location of the magnetic obstacle. As previously mentioned, these two parameters have a crucial role in obtaining global information regarding the heat transfer performance of the liquid metal flow under the influence of a localized magnetic field.

Figure 6.16(a) displays a temperature map in the $x - y$ plane at the mid-plane $z = 1$, for the purely hydrodynamic case with $Re = 900$ while Figure 6.16(b) shows the MHD case obtained with parameters $Re = 900$ and $Ha = 100$. Qualitatively, it can be observed that in the hydrodynamic case, the temperature profile displays a uniform development, whereas in the MHD case, clear temperature variations are observed, as a result of the fluid agitation caused by the presence of the magnetic obstacle, which promotes higher temperatures in regions further away from the wall subjected to constant temperature. In fact, these temperature variations are related with the peak values of the local Nusselt number shown in Figure 6.16(b). An overall evaluation yields a global Nussel number $Nu = 7.3$ for the hydrodynamic case and $Nu = 7.5$ for the MHD case. Given that the percentage increment of overall heat transfer is not significant, it is convenient to explore distinct configurations of localized magnetic fields.
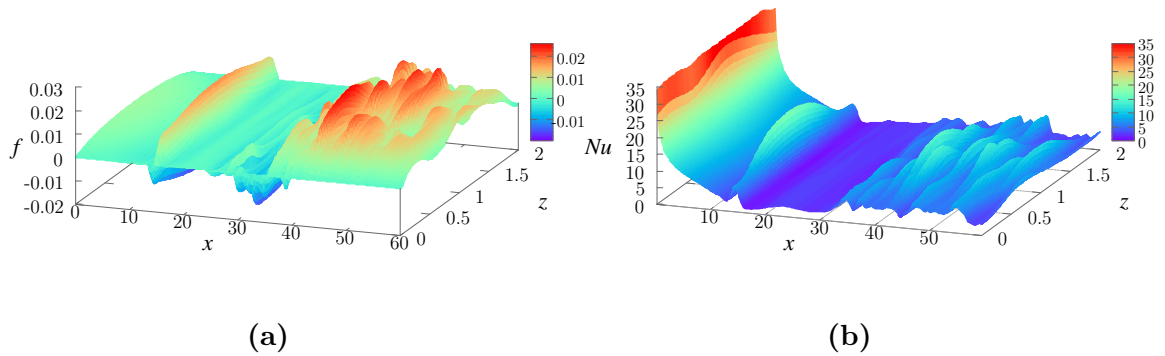
Figure 6.15: (a) Local friction factor, and (b) local Nusselt number obtained for $Re = 900$ and $Ha = 100$ at the side wall subject to a constant high temperature.
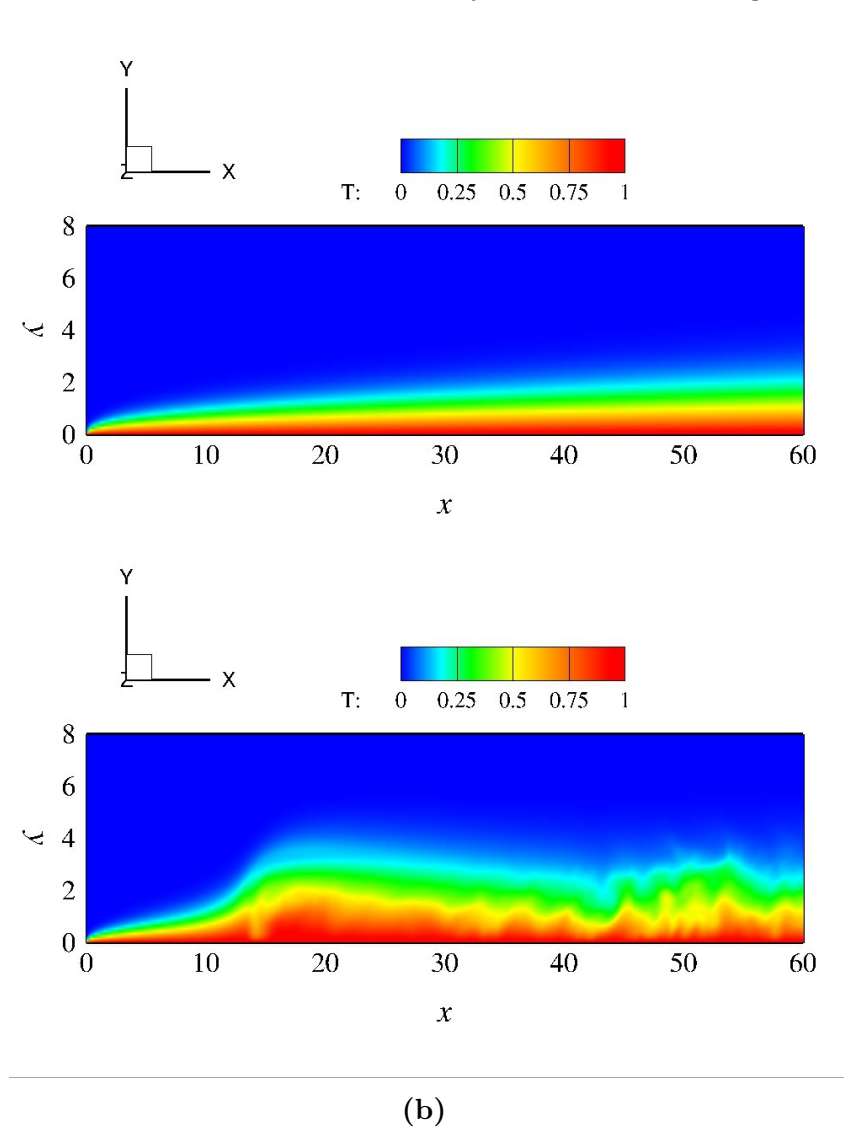

(b)

Figure 6.16: Temperature map for $Re = 900$ at the mid-plane $z = 1$. (a) Purely hydrodynamic case, $Ha = 0$, and (b) $Ha = 100$.
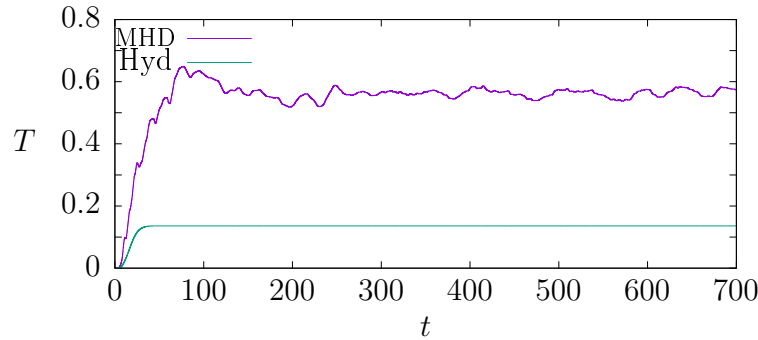
Figure 6.17: Time-series of temperature for 700 dimensionless time units at the fixed point $y = 1.5$, and $z = 1$, 10 units downstream from the center of the magnetic obstacle for (a) the purely hydrodynamic case $Re = 900$, $Ha = 0$ and (b) the MHD case $Re = 900$ and $Ha = 100$.
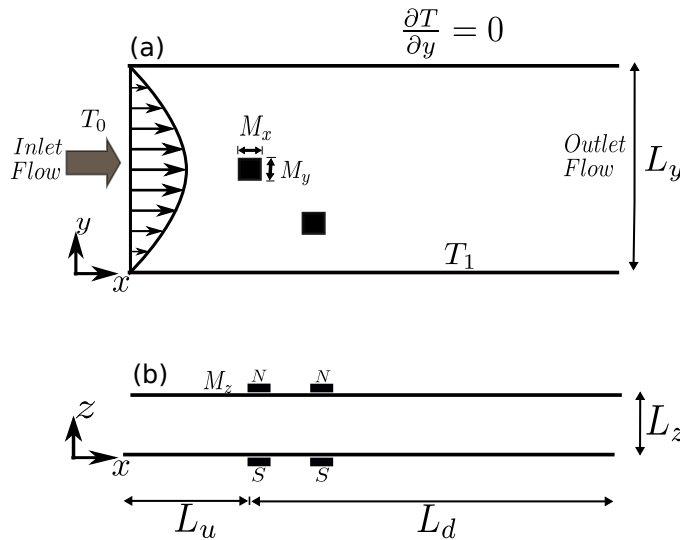

Figure 6.18: Schematic of the 3D liquid metal flow within an array of two magnets.

In Figure 6.17, time-series of temperature are shown for the purely hydrodynamic case with $Re = 900$ (green color) and for the MHD case with $Re = 900$ and $Ha = 100$ (violet color). The data is obtained at a fixed point located 10 units downstream from the center of the magnetic obstacle, $y = 1.5$ and $z = 1$. We observe that the temperature remains nearly constant in the hydrodynamic case, reaching an average value of $T = 0.15$. In the MHD case, due to the agitation caused by the magnetic obstacle, the average temperature reached at that point is about four times higher than in the hydrodynamic case, with a value of $T = 0.6$.

Two different configurations of magnets are examined. Figure 6.18 shows a schematic of the 3D liquid metal flow within an array of two pairs of magnets. In this configuration, two magnetic obstacles are generated by square magnets placed at the geometric centers $(14,4)$ and $(18,2)$ in the $x - y$ plane. In Figure 6.19, the duct flow is depicted within an array of three pairs of magnets positioned at the geometric centers corresponding to coordinates $(14,6)$, $(17,4)$, and $(20,1.5)$ in the $x - y$ plane.
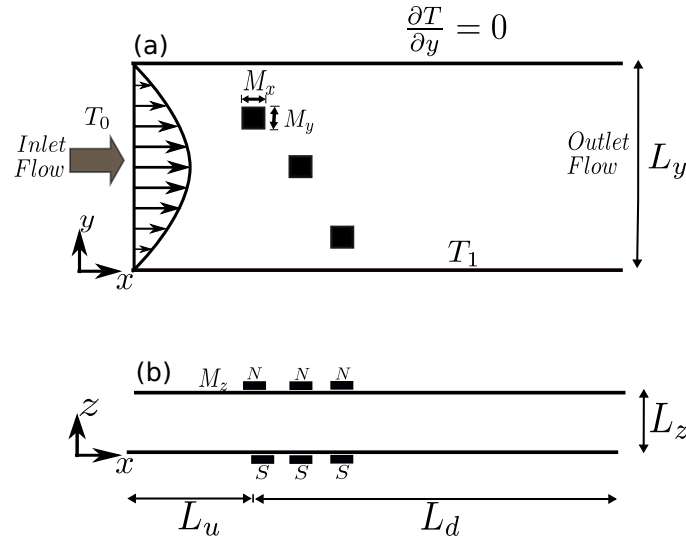
Figure 6.19: Schematic of the 3D liquid metal flow within an array of three magnets.

Figure 6.20(a,b) show the map of the streamwise velocity and temperature, respectively, at a specific instant $t = 200$, considering two magnetic obstacles, $Re = 900$ and $Ha = 100$ at the mid-plane $z = 1$. Fig. 6.20(c,d) shows the map of the streamwise velocity and temperature for a system involving three magnetic obstacles. As can be noticed, the number of localized magnetic fields considered leads to clear modifications in the flow pattern. Each flow pattern promote a distinct effect on heat transfer. The heat transfer analysis of the MHD flow with two square magnets reveals a global Nusselt number of $Nu = 9.1$, while the configuration involving a set of three magnets yields a Nusselt number of $Nu = 9.5$. Although these values exhibit slight differences, they are significant compared to the hydrodynamic case with $Nu = 7.3$. The performance factor values obtained are $f_c = 0.9$ and $f_c = 0.87$ for the system with two and three magnets, respectively. This leads to an increase in pressure drop due to the presence of the localized magnetic field. On the other hand, the percentage increment of overall heat transfer is $HI = 24.3\%$ and $HI = 28.9\%$ for the system with two and three magnets, respectively, compared to the purely hydrodynamic case. While these results provide some encouraging evidence of heat transfer enhancement, further studies are needed to explore conditions that optimize heat transfer. This is a task for future work.
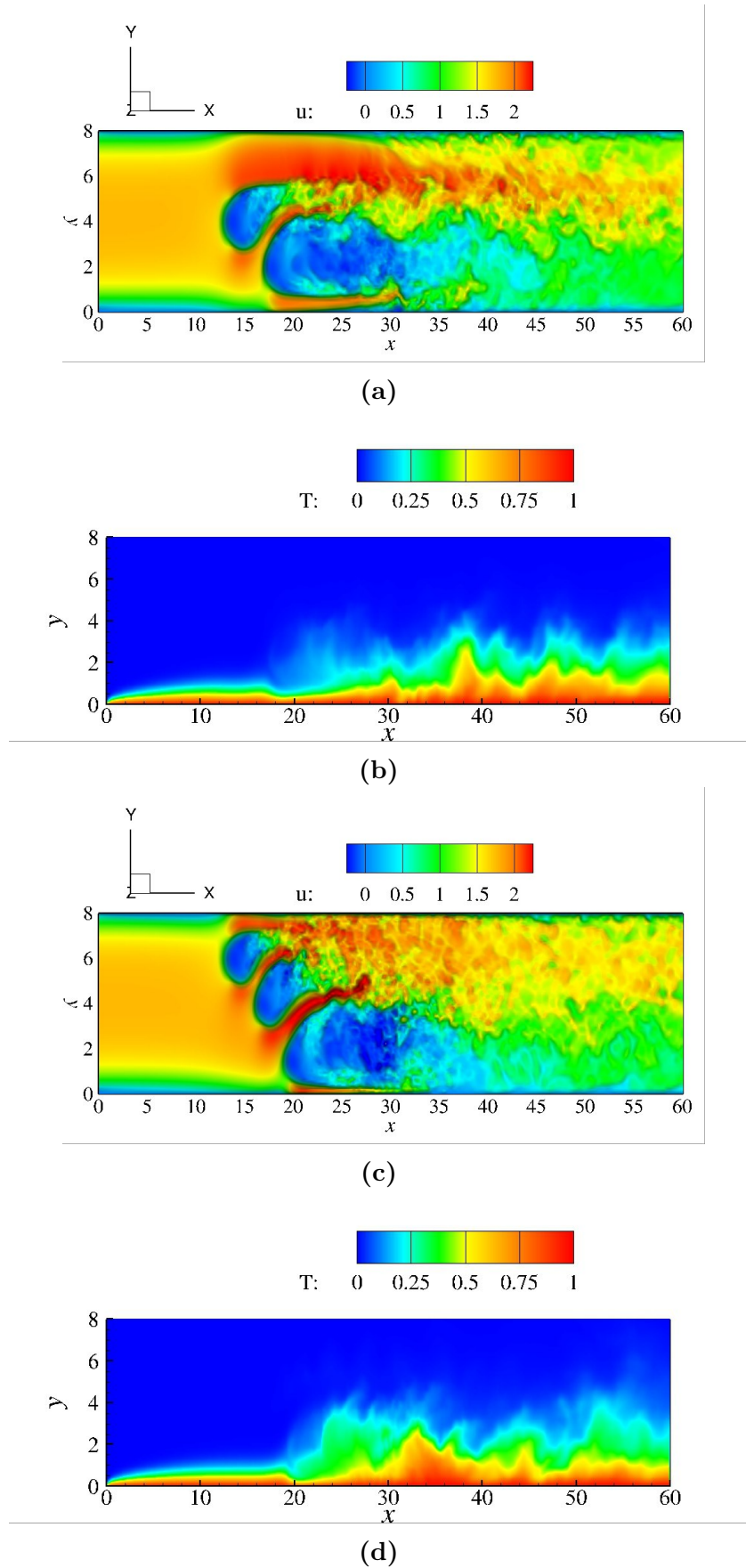
(a)

(b)

(c)

(d)

Figure 6.20: Instant map of the magnitude of the streamwise velocity and temperature for $Re = 900$ at the mid-plane $z = 1$. For an MHD flow with (a,b) two magnetic obstacles and (c,d) three magnetic obstacles.

Concluding remarks

In this thesis, a numerical study of the dynamics and heat transfer characteristics of liquid metal flows in ducts under applied magnetic fields was performed. The study involved examining the effects of both uniform and non-uniform magnetic fields generated by permanent magnets. To carry out the research, computing codes based on the Finite Volume Method were developed by the author using the Fortran programming language. The accuracy and reliability of these codes were rigorously validated through comparisons with analytical solutions in proper limits and experimental data, yielding robust agreement. The investigation aims to provide a comprehensive understanding of the dynamical behavior of liquid metal flows under the influence of magnetic fields and their impact on heat transfer. For the mathematical modeling of liquid metal MHD duct flows, the governing equations were formulated using either the B or ϕ-formulation. Numerical simulations were conducted employing different approaches, including two-dimensional, quasi-two-dimensional, and three-dimensional models. The geometry of the duct consistently involved a rectangular cross-section. Dimensionless parameters that govern MHD flows, namely the Reynolds number and the interaction parameter (or alternatively the Hartmann number) were systematically varied to cheracterize the behavior of the liquid metal MHD flows. The work also explores how the electrical conductivity of the duct walls, the size of the duct, and the arrangement of the magnet influence flow patterns and subsequently heat transfer.

For simplicity, we initially focused on a two-dimensional approximation of a liquid metal duct flow in Chapter 3. This allows for a numerical characterization of heat transfer performance in the presence of a *magnetic fin*, mimicking the configuration of a heat exchanger with solid obstacles or baffle cuts. The study encompasses a wide range of Hartmann numbers and three fixed Reynolds numbers. Although this approximation imposes limitations on the scope of our approach, it still captures essential physical aspects of the flow. When the coupling between electromagnetic and inertial forces is strong enough, vortex shedding occurs, leading to enhanced stirring and increased heat transfer from the heated wall. It was found that optimal heat transfer is achieved at a specific ratio of Lorentz to inertial forces. This finding highlights the importance of balancing these two forces in achieving efficient heat transfer in the liquid metal duct flow system. An optimal global performance was found for a fixed Reynolds number that leads to a significant heat transfer enhancement compared to the purely hydrodynamic case. Although the 2D analysis points to the efficacy of magnetic fins as a non-intrusive method for enhancing heat transfer in liquid metal duct flows, it made clear the need for investigating more realistic models based on fully three-dimensional simulations.

We developed a 3D numerical code based on the ϕ-formulation and, in order to validate it, in Chapter 4, we obtained an exact analytical solution for the fully developed MHD flow of a liquid metal in a rectangular duct which, along with other available solutions, were compared in the proper limits with 3D numerical solutions, finding a very good agreement.

A very important step of this work was to perform a numerical analysis of a realistic liquid metal MHD duct flow utilizing experimental data from a study conducted by Domínguez *et al.* [45]. The experimental conditions were replicated in a numerical simulation of the time-dependent MHD flow. To validate the numerical simulation, the results were compared with experimental data within the interaction parameter range $4.5 < N < 72$, (or alternatively $500 < Re < 8000$) while maintaining a constant magnetic field strength, so that the Hartmann number remained constant ($Ha = 190$). The simulation exhibited good agreement with the experimental data, demonstrated through comparisons of time series of the streamwise velocity component as well as oscillation frequencies of this component. In addition, the parameter L^2 that provides information about the kinetic energy of the flow and that was calculated from experimental data in [45] as a function of the Reynolds number, was reproduced numerically with a good agreement. This analysis also provides insight into the interplay between intertia and the Lorentz force which mainly determines the flow patterns observed in the flow past a magnetic obstacle. In fact, unlike what is observed in the wake of a solid obstacle, an increase of the Reynolds number for a fixed magnetic field strenght does not lead to a more disordered an eventually turbulent flow but, instead, the flow tends to return to the steady state.

Despite inherent measurement errors of approximately 8% in the experimental data, the relative error between the numerical and experimental results was around 10.5%. This error decreased to approximately 4% for larger values of N, but increased up to a maximum of 17% as N decreased. Thus, it can be concluded that the numerical code adequately simulates the experimental results within the specified parameter range. A second objective of this study was to explore the three-dimensional characteristics of the flow through numerical simulations, aiming to gain a deeper understanding of flow dynamic characteristics that cannot be easily observed experimentally. The simulations revealed the evolution of flow patterns as the Reynolds number increases with a constant Hartmann number, starting at a pattern with two vortices, moving to patterns with four, six, again two and finally flow patterns with no vortices, obtained for Re high enough. In fact, steady and unsteady patterns were found. Moreover, it was shown that the friction coefficient was approximately inversely proportional to the Reynolds number.

Reliability of different approximations, namely 2D, Q2D, and 3D models for analyzing the heat transfer in flows with localized magnetic fields in a slender duct was also explored. Due to the computational expense of numerical simulations, it is crucial to estimate the accuracy of these approximations. Comparisons were made from a fully 3D model and it was observed that the Q2D model tended to overestimate the friction effect of the walls and magnetic obstacles, resulting in stronger flow braking and increased wall heat transfer. Conversely, the 2D model exhibited significant deviations from the Q2D and 3D models, particularly in the context of a slender

duct flow. Under conditions where convective heat transfer effects were significant, and Lorentz forces dominated over inertial effects, higher constrainment factors and smaller gap ratios contributed to enhanced heat transfer. These findings suggest that the strategic use of localized magnetic fields has the potential to enhance heat transfer through the promotion of increased stirring. This was shown from the analysis of the global Nusselt number and the global friction coefficient from which the the thermal performance factor, commonly used in the analysis of mechanical swirl flow devices, was calculated, indicating an encouraging improvement in the heat transfer. However, although some modifications were implemented to improve the accuracy and efficiency of the analysis such as the use of a non-uniform mesh with a stretching function to enhance mesh refinement near the walls and the region containing the magnetic obstacle, the full assessment of the three-dimensional heat transfer remains an ongoing task.

Other tasks that need to be addressed in the future are optimizing the performance 3D numerical codes to reduce computation time, as well as exploring different magnet configurations for heat transfer enhancement. Furthermore, the inclusion of natural convection effects is an important aspect that must be considered for better physical understanding of the analyzed phenomena.

Non-uniform grid generation

In numerical simulations in duct flows, mesh clustering near walls or regions where large gradients appear is often necessary. It is commonly implemented in numerical simulations to increase the accuracy of the solution and capture details of the flow under study. Moreover, to reduce computational costs, it is desirable to use a coarser mesh to spread out the numerical calculation in areas with small gradients and a finer mesh in areas with large gradients that cause a variable to grow or diminish rapidly. To achieve this, a stretching function can be implemented, as described in detail in [80]. We present the mesh clustering following the proposal of references [81], [80], namely,

$$x_i = L \left[\frac{1 + \tanh K_x \left\{ \left(\frac{2i-2}{N_x-2} \right) - 1 \right\}}{2 \tanh K_x} \right], \tag{A.1}$$

$$y_i = c \left[1 + \frac{\sinh \left\{ K_x \left(\frac{i}{N_x} - \frac{1}{2K_x} \right) \right\}}{\sinh \left\{ K_x \left(\frac{1}{2K_x} \ln \left[\frac{1 + \frac{c}{L}(\mathrm{e}^{K_x}-1)}{1 + \frac{c}{L}(\mathrm{e}^{-K_x}-1)} \right] \right) \right\}} \right], \tag{A.2}$$

where x_i is and y_i are arbitrary variables since the stretching functions can be implemented in any of the three coordinates x, y, z according to the requirements of the problems, N_x total number of nodes, K_x stretching factor which determines the level of clustering, L spacing between parallel walls and c point where mesh is clustered. We present two function, the first is given by (A.1) which allows clustering toward walls or specific regions with large gradients, and the other function (A.2) allows clustering toward the interior of the numerical domain. For viewing purposes, Figure A.1(a) shows the mesh produced by including a clustering function toward walls while Figure A.1(b) shows the mesh produced by using a function that cluster toward the interior of the numerical domain.

To make sure about the proper implementation and operation of a clustered mesh in our numerical codes. We first implement a numerical simulation of a bidimensional Poisson equation using a clustered mesh and numerical results are compared with an analytical solutions of the problem. The equation to be solved is

$$\frac{\partial^2 u}{\partial x^2} + \frac{\partial^2 u}{\partial y^2} = -52 \cos(4x + 6y). \tag{A.3}$$
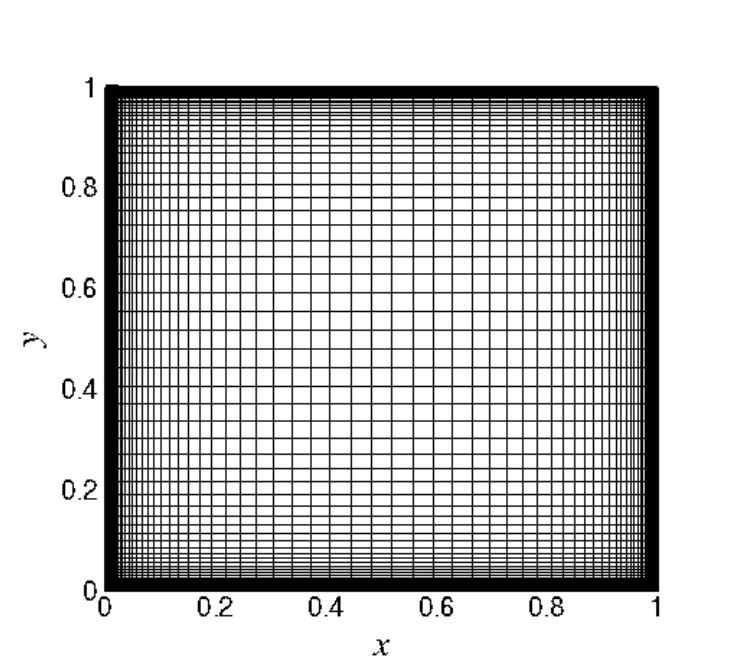
(a)
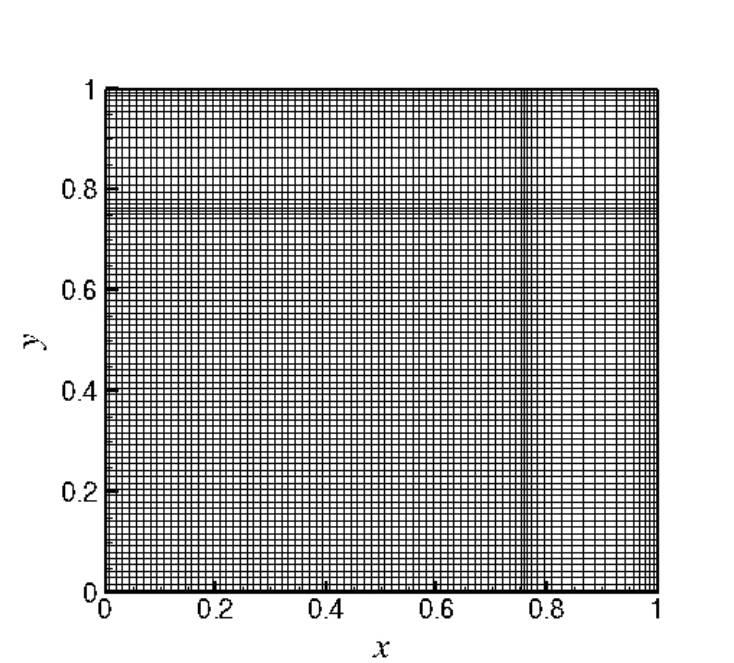
(b)

Figure A.1: Numerical non-uniform structured mesh clustered (a) near the walls and, (b) in a localized zone, in the $x - y$ plane.

The equation is subject to boundary conditions of first type, second type, and third type as follows

$$u(x,0) = \cos(4x), \quad \frac{1}{6}\frac{\partial u}{\partial y}(x,1) + u(x,1) = \cos(4x+6) - \sin(4x+6),$$

$$\frac{\partial u}{\partial x}(0,y) = -4\sin(6y), \quad \frac{\partial u}{\partial x}(1,y) = -4\sin(4+6y).$$

Whose analytical solution is given by

$$u(x,y) = \cos(4x+6y). \tag{A.4}$$

The estimated error corresponds to the difference between both solutions, numerical and analytical and is shown in Figure A.2. As can be observed, the discrepancy between both solutions diminishes as the clustering increases.
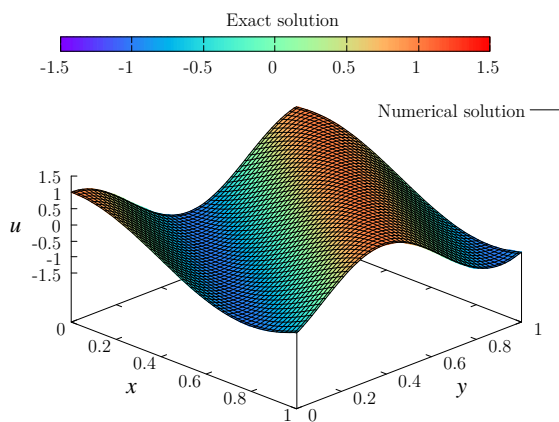
Another validation of the implementation of a clustered mesh is carried out through the comparison of numerical results of the classical problem Lid-Driven Cavity Flow using a uniform mesh and a clustered mesh. Figure A.3 shows the scheme of the problem to be solved. The numerical solution has been validated by comparing with [82] and obtaining good agreement between both results. Figure A.4 shows the comparison of the velocity profiles obtained with FVM using a clustered mesh and those reported by Ghia *et al.* (1982) along the central lines for $Re = 100$. Complementarily, velocity profiles of the flow inside a square cavity generated by the sliding of one of its walls are shown in Figure A.5, where various refinement strategies have been implemented, including the use of a clustered mesh in the middle of the domain, near the walls, or a combination of both. Additionally, uniform and non-uniform meshes can be applied in different sections of the domain.

The balance equations that model the phenomenon are
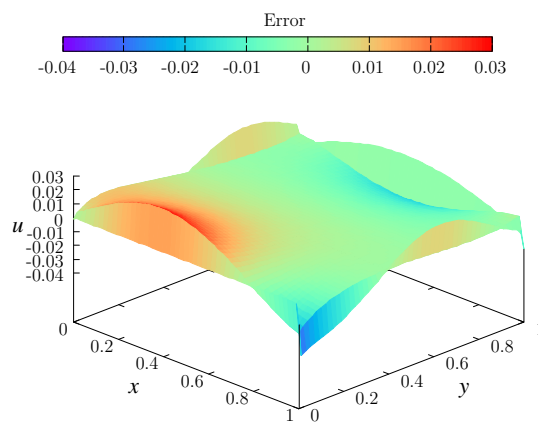
$$\nabla{\cdot}\mathbf{u} = 0, \tag{A.5}$$

$$\frac{\partial u}{\partial t} + (\mathbf{u}{\cdot}\nabla)\,u = -\frac{\partial p}{\partial x} + \frac{1}{Re}\nabla^2 u, \tag{A.6}$$

$$\frac{\partial v}{\partial t} + (\mathbf{u}{\cdot}\nabla)\,v = -\frac{\partial p}{\partial y} + \frac{1}{Re}\nabla^2 v, \tag{A.7}$$

(a) Comparison of exact and numerical resuts using an uniform mesh.

(b) Error obtained using an uniform mesh.
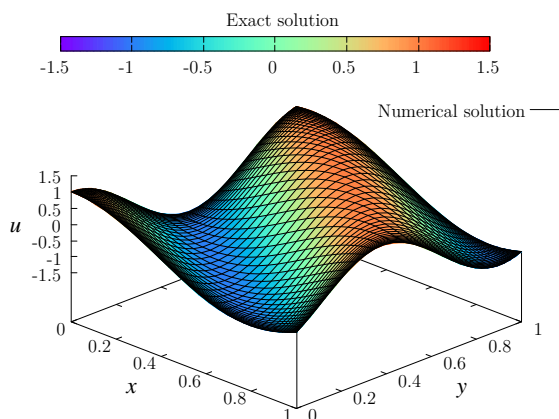
(c) Comparison of exact and numerical resuts with a clustered mesh toward walls in x,y-directions.
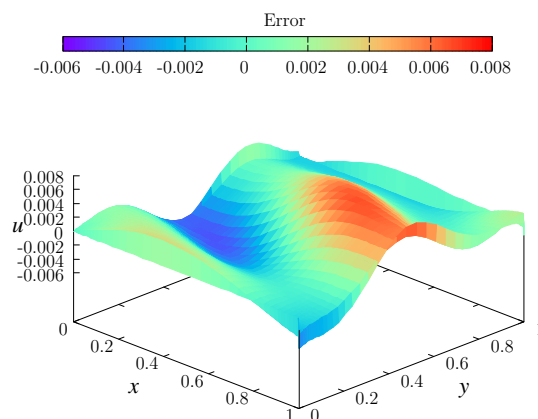
(d) Error obtained using a clustered mesh toward walls.
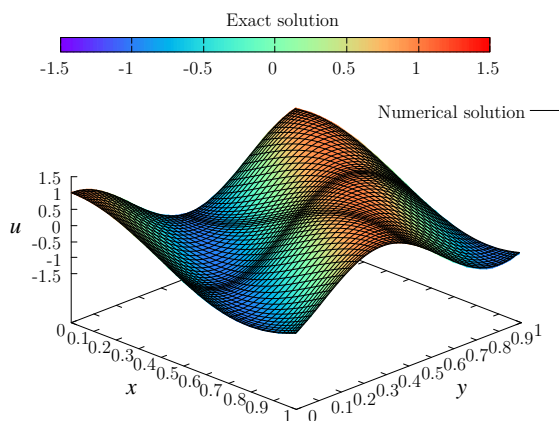
(e) Comparison of exact and numerical resuts with a clustered mesh toward walls and middle of domain.
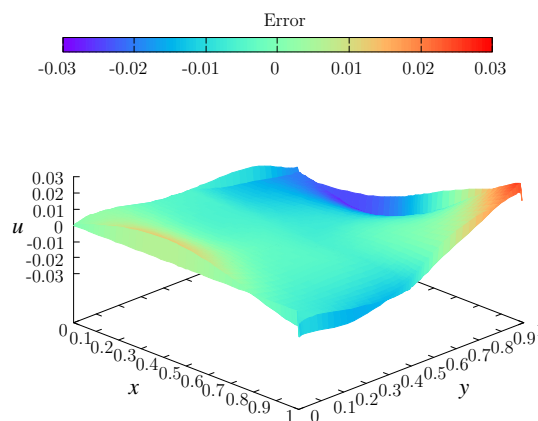
(f) Error obtained using a clustered mesh toward walls and middle of domain.

Figure A.2: Numerical solution using a clustered mesh.
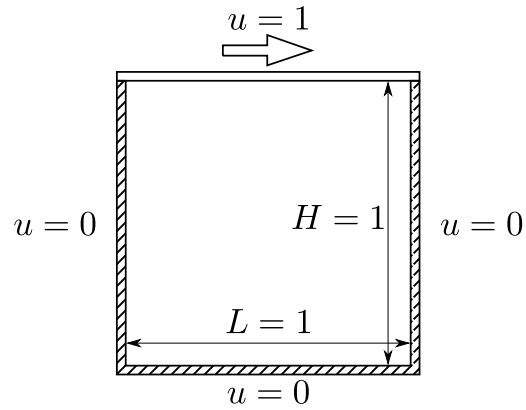
Figure A.3: Scheme of the "lid-driven cavity flow".
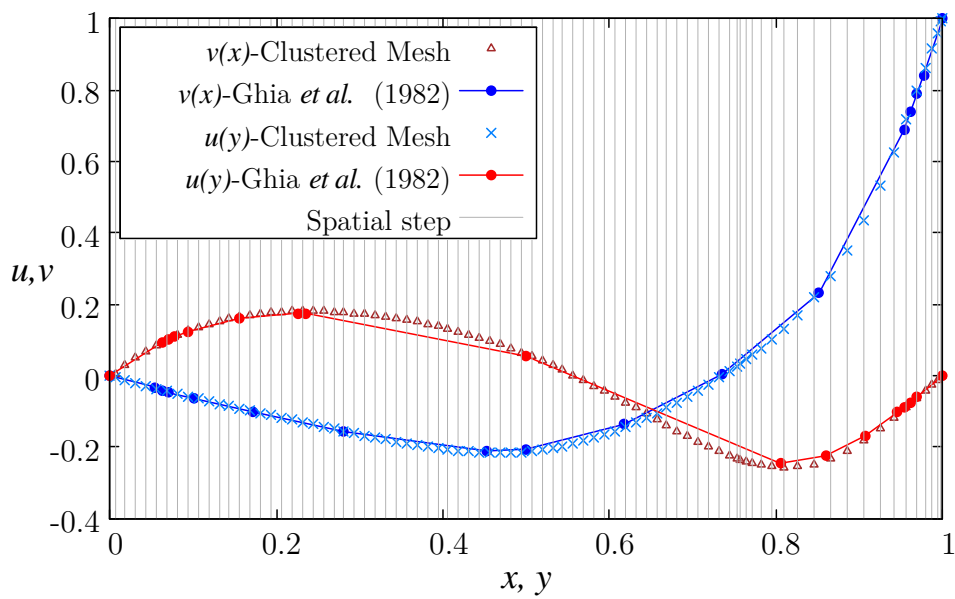
Figure A.4: Comparison of the velocity profiles obtained with FVM using a clustered mesh and those reported by Ghia et al. (1982) along the central lines for $Re = 100$.
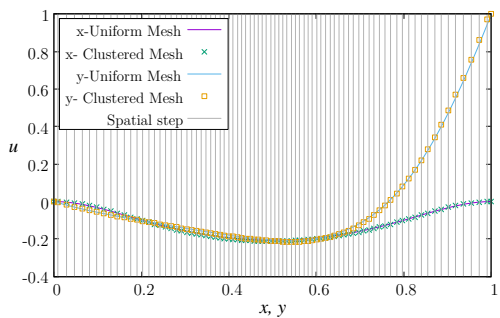
(a) Clustered mesh toward middle of domain.
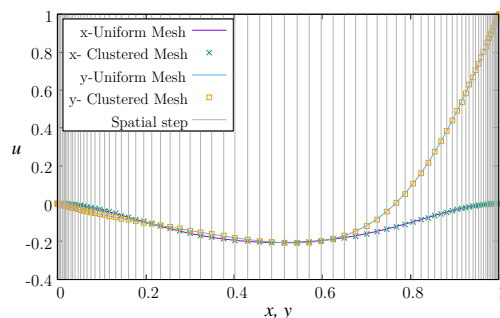
(b) Clustered mesh toward walls.
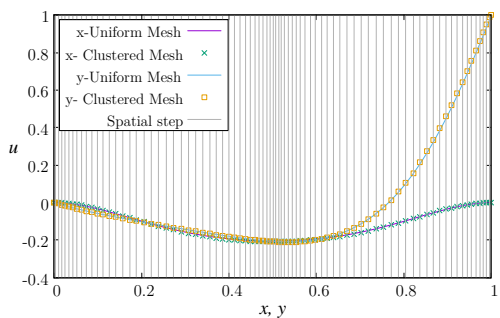
(c) Clustered mesh toward walls and middle of domain.
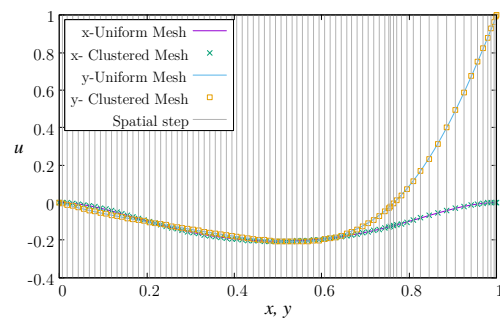
(d) Combining uniform and clustered mesh in a section of domain.
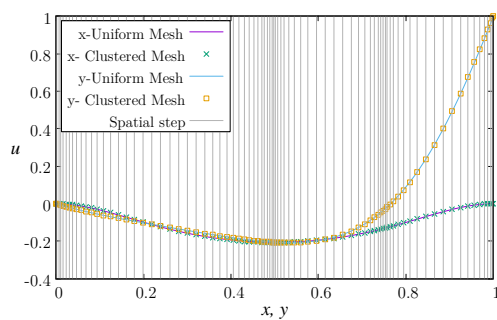
(e) Clustered mesh toward walls and two localized zones within the domain.

Figure A.5: Numerical solution using clustered meshes.

Finite Volume discretization

The FVM involves converting the original partial differential equation into a system of linear equations. The methodology to solve the general advection-diffusion equation used to model various physical phenomena of interest as well as the conservation of momentum equation for an incompressible fluid is described in this section. For practicality, we begin with the implementation of the FVM, focusing on the treatment of the general advection-diffusion equation. This approach involves approximating the solution of the differential equation by integrating it over each control volume of the numerical domain,

$$\int_{\Delta V} \frac{\partial \phi}{\partial t} dV + \int_{\Delta V} (\nabla \cdot \boldsymbol{u} \phi) \, dV = \int_{\Delta V} \nabla \cdot (\Gamma \nabla \phi) \, dV + \int_{\Delta V} S dV, \qquad (B.1)$$

with the aim of finding a function $\phi(x, y, z, t)$ that satisfies (2.29) subject to a set of initial and boundary conditions. Upon integrating each term, the discrete form of the advection-diffusion equation is obtained

$$\overbrace{\frac{\phi_P - \phi_P^0}{\Delta t} \Delta V}^{\text{Temporal term}} + \overbrace{\frac{u_e S_e}{2} \phi_E - \frac{u_w S_w}{2} \phi_W + \frac{v_n S_n}{2} \phi_N - \frac{v_s S_s}{2} \phi_S}^{\text{Convective term}} =$$

$$\underbrace{\Gamma_e S_e \frac{\phi_E - \phi_P}{\Delta x} - \Gamma_w S_w \frac{\phi_P - \phi_W}{\Delta x} + \Gamma_n S_n \frac{\phi_N - \phi_P}{\Delta y} - \Gamma_s S_s \frac{\phi_P - \phi_S}{\Delta y}}_{\text{Difusive term}} + \underbrace{\bar{S}_P \Delta V}_{\text{Source term}} \; .$$

$$(B.2)$$

By grouping and ordering the terms containing the dependent variable, it is possible to express the previous equation in the form

$$a_P \phi_P = a_E \phi_E + a_W \phi_W + a_N \phi_N + a_S \phi_S + S_P, \qquad (B.3)$$

where the coefficients of this equation are given by

$$a_E = \frac{\Gamma_e S_e}{\Delta x} - \frac{u_e S_e}{2}; \quad a_W = \frac{\Gamma_w S_w}{\Delta x} + \frac{u_w S_w}{2}, \qquad (B.4)$$

$$a_N = \frac{\Gamma_n S_n}{\Delta y} - \frac{v_n S_n}{2}; \quad a_S = \frac{\Gamma_s S_s}{\Delta y} + \frac{v_s S_s}{2}, \qquad (B.5)$$

$$a_P = a_E + a_W + a_N + a_S + \frac{\Delta V}{\Delta t}; \quad S_P = \bar{S}_P \Delta V + \phi_P^0 \frac{\Delta V}{\Delta t}. \qquad (B.6)$$

A system of linear equations is obtained, with the values of ϕ at the corresponding points of the chosen mesh as variables.

Pressure−Velocity Decoupling

To solve the conservation of momentum equation for an incompressible fluid, it is necessary to determine the pressure field. With this purpose, the discrete form of the equation for the u component of the velocity is shown below

$$a_P u_P = a_E u_E + a_W u_W + a_N u_N + a_S u_S + S_P, \tag{B.7}$$

where

$$a_E = \frac{\Gamma_e S_e}{\Delta x} - \frac{u_e S_e}{2}, \quad a_W = \frac{\Gamma_e S_e}{\Delta x} + \frac{u_w S_w}{2}, \tag{B.8}$$

$$a_N = \frac{\Gamma_n S_n}{\Delta y} - \frac{v_n S_n}{2}, \quad a_S = \frac{\Gamma_s S_s}{\Delta y} + \frac{v_s S_s}{2}, \tag{B.9}$$

$$a_P = a_E + a_W + a_N + a_S + \frac{\Delta V}{\Delta t}, \tag{B.10}$$

$$S_P = \bar{S}_P \Delta V - \left(\frac{\partial p}{\partial x}\right)_P \Delta V + u_P^0 \frac{\Delta V}{\Delta t} \;=\; \bar{S}_P - \frac{(p_E - p_P)}{\Delta x}\Delta V + u_P^0 \frac{\Delta V}{\Delta t}. \tag{B.11}$$

Thus, (B.7) can be rewritten as follows,

$$a_P u_P = \sum_f a_f u_f + b - (p_E - p_P)\, A_e, \tag{B.12}$$

being

$$b = \bar{S}_P \Delta V + u_P^0 \frac{\Delta V}{\Delta t}, \quad A_e = \frac{\Delta V}{\Delta x} = \Delta y = S_e, \tag{B.13}$$

and the subscript f indicates that the summation is performed considering all faces of the control volume.

Given that (B.12) governs the behavior of the u component of the velocity, the remaining task to solve it is to determine the pressure and incorporate it into the source term. Since the pressure is not known, we assume a pressure p^*, leading the momentum equations in two-dimensions to take the form of

$$a_P u_P^* = \sum_f a_f u_f^* + b - (p_E^* - p_P^*)\, A_e, \tag{B.14}$$

$$a_P v_P^* = \sum_f a_f v_f^* + b - (p_N^* - p_P^*)\, A_n. \tag{B.15}$$

The solution yields a velocity field $\boldsymbol{u}^*$ that does not satisfy the continuity equation. To ensure a physically accurate velocity field, adjustments can be made to the assumed pressure field and the velocity obtained through the equations.

$$\boldsymbol{u} = \boldsymbol{u}^* + \boldsymbol{u}', \quad p = p^* + p', \tag{B.16}$$

where the primed variables $\boldsymbol{u}', p'$ represent small corrections to the respective variables.

By subtracting (B.14) from (B.12), we arrive at the expression of corrections

$$
a_P \overbrace{(u_P - u_P^*)}^{u_P'} = \sum_f a_f \overbrace{\left(u_f - u_f^*\right)}^{u_f'} - \left(\overbrace{(p_E - p_E^*)}^{p_E'} - \overbrace{(p_P - p_P^*)}^{p_P'} \right) A_e, \tag{B.17}
$$

or alternatively

$$
a_P u_P' = \sum_f a_f u_f' - (p_E' - p_P') A_e. \tag{B.18}
$$

A simplification is performed on the summation term, considering that the difference between the velocity corrections at the center of the control volume and its neighbors is small (SIMPLEC method, where C stands for Corrected). The summation term can be neglected, and by solving for the velocity correction, we obtain that the corrections for the u component of velocity are given by

$$
u_P' = -\frac{A_e}{a_P - \sum a_f}(p_E' - p_P') = de(p_P' - p_E'). \tag{B.19}
$$

Similarly, by following the same procedure for the v component, we can conclude that the corrections for the v component of velocity are given by

$$
v_P' = -\frac{A_n}{a_P - \sum a_f}(p_N' - p_P') = dn(p_P' - p_N'). \tag{B.20}
$$

Considering the two equations above, the velocity components are corrected according to

$$
u_P = u_P^* + de(p_P' - p_E'), \tag{B.21}
$$

$$
v_P = v_P^* + dn(p_P' - p_N'), \tag{B.22}
$$

where de and dn coefficients used to obtain the pressure corrections. In order to correct the velocity, it is necessary to know the corrections for the pressure field, for which the discretized continuity equation is used.

$$
u_e S_e - u_w S_w + v_n S_n - v_s S_s = 0. \tag{B.23}
$$

The computation of the divergence of $\boldsymbol{u}$ is carried out at the control volume centers to evaluate the pressure field, considering the staggered grid arrangement. Furthermore, the velocities corresponding to the faces of the control volume for pressure are determined by employing (B.21) and (B.22), which are appropriately handled to be substituted into the continuity equation, and after simplifications, the terms can be written in the form

$$
a_P p_P' = a_E p_E' + a_W p_W' + a_N p_N' + a_S p_S' + S_P, \tag{B.24}
$$

where

$$a_E = (de)_e S_e, \quad a_W = (de)_w S_w, \quad a_N = (dn)_n S_n, \quad a_S = (dn)_s S_s, \tag{B.25}$$

$$a_P = a_E + a_W + a_N + a_S, \quad S_P = - \left(u_e^* S_e - u_w^* S_w + v_n^* S_n - v_s^* S_s \right) = -\nabla \cdot \boldsymbol{u}^*. \tag{B.26}$$

It is important to note that (B.24) has the same structure as the discrete form of a transport equation.

Figure B.1 shows a flowchart with the algorithm for seeking a numerical solution with the FVM.

1. The flowchart begins by initializing variables, mesh creation,, the placement of magnetic fields and establishment of initial and boundary conditions.

2. Start temporal cycle

3. Start SIMPLEC cycle. The methodology to solve the Navier-Stokes equations to determine the velocity field can establish as

   - Assume a pressure field p.
   - With the assumed pressure field, obtain the velocity field $\boldsymbol{u}^*$ by solving (B.14) and (B.15).
   - Knowing $\boldsymbol{u}^*$, calculate the source term $(-\nabla \cdot \boldsymbol{u}^*)$ for the pressure corrections and solve (B.24) to obtain p'.
   - The pressure field is corrected as $p = p^* + p'$.
   - Correct the velocities using (B.21) and (B.22).
   - Iterate until the convergence criteria are satisfied.

4. The velocity field is updated based on the corrected pressure field.

5. Iterate until reach a desired level of accuracy.

6. The algorithm ends, and the final velocity field is obtained

START

Declaration of variables
Mesh creation
Placement of magnetic fields
Establishment of initial and boundary conditions

Start temporal cycle

Advection-diffusion equation for temperature
$$a_p \phi_p = \sum a_f \phi_f + b$$
Boundary correction

Start SIMPLEC cycle

Set
$$P* = P$$
$$\boldsymbol{u}* = \boldsymbol{u}$$

Solve discretized momentum equation
to obtain approximate velocity fields
$$a_p u_p^* = \sum a_f u_f^* + b + A_e \left(P_p^* - P_E^* \right)$$
Boundary correction

Determine the correction equation for pressure
$$a_p P_p' = \sum a_f P_f' + b$$

Set
$$P* = P$$
$$\boldsymbol{u}* = \boldsymbol{u}$$

Correct pressure and velocity
$$P = P^* + P'$$
$$\boldsymbol{u}_p = \boldsymbol{u}_p^* + df \left(P_p' - P_f' \right)$$

No ⟨ Converged? ⟩

Yes

Stop SIMPLEC cycle

Next time step t=t+1

**STOP
temporal cycle**
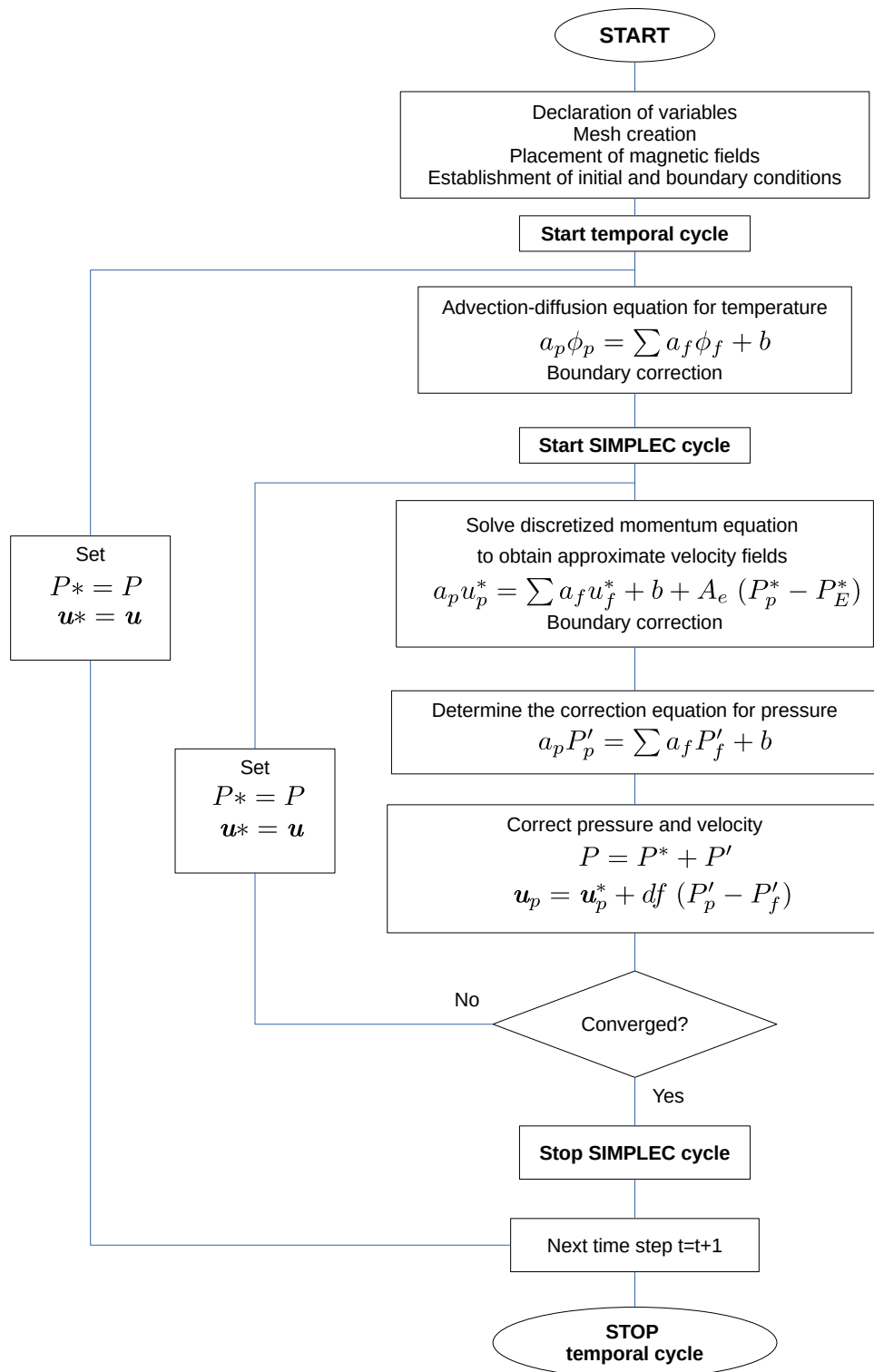
Figure B.1: The algorithm for seeking a numerical solution with the FVM.

Bibliography

[1] P. H. Roberts, "An introduction to magnetohydrodynamics," 1967.

[2] S. Molokov, R. Moreau, K. Moffatt, and L. Bühler, "Liquid metal magnetohydrodynamics for fusion blankets," *Magnetohydrodynamics: Historical Evolution and Trends*, pp. 171–194, 2007.

[3] J. Hartman, "Theory of the laminar flow of an electrically conducting liquid in a homogeneous magnetic field, math," *Fys. Medd*, vol. 15, no. 6, 1937.

[4] J. Hartmann and F. Lazarus, "Hg-dynamics ii. experimental investigations on the flow of mercury in a homogeneous magnetic field," *Mathematisk-fysiske Meddelelser. XV*, vol. 15, p. 7, 1937.

[5] W. F. Hughes and F. J. Young, *The electromagnetodynamics of fluids.* New York: Wiley, 1966.

[6] U. Müller and L. Bühler, *Magnetofluiddynamics in channels and containers.* Springer Science & Business Media, 2001.

[7] J. Shercliff, "Steady motion of conducting fluids in pipes under transverse magnetic fields," in *Mathematical Proceedings of the Cambridge Philosophical Society*, vol. 49, pp. 136–144, Cambridge University Press, 1953.

[8] J. Hunt, "Magnetohydrodynamic flow in rectangular ducts," *Journal of fluid mechanics*, vol. 21, no. 4, pp. 577–590, 1965.

[9] J. Hunt and K. Stewartson, "Magnetohydrodynamic flow in rectangular ducts. ii," *Journal of fluid mechanics*, vol. 23, no. 3, pp. 563–581, 1965.

[10] J. Walker and G. Ludford, "Mhd flows in variable-area rectangular ducts with mixed wall conductivities," in *Southeastern Conference on Theoretical and Applied Mechanics, 7 th, Washington, D. C*, pp. 45–60, 1974.

[11] J. Walker, G. Ludford, and J. Hunt, "Three-dimensional mhd duct flows with strong transverse magnetic fields. part 2. variable-area rectangular ducts with conducting sides," *Journal of Fluid Mechanics*, vol. 46, no. 4, pp. 657–684, 1971.

[12] J. Walker, "Magnetohydrodynamic flows in rectangular ducts with thin conducting walls. i: Constant-area and variable-area ducts with strong uniform magnetic fields," 1981.

[13] S. Smolentsev, N. Vetcha, and M. Abdou, "Effect of a magnetic field on stability and transitions in liquid breeder flows in a blanket," *Fusion Engineering and Design*, vol. 88, no. 6-8, pp. 607–610, 2013.

[14] T. Arlt, J. Priede, and L. Bühler, "The effect of finite-conductivity hartmann walls on the linear stability of hunt's flow," *Journal of Fluid Mechanics*, vol. 822, pp. 880–891, 2017.

[15] S. Cuevas, B. Picologlou, J. Walker, and G. Talmage, "Liquid-metal mhd flow in rectangular ducts with thin conducting or insulating walls: laminar and turbulent solutions," *International journal of engineering science*, vol. 35, no. 5, pp. 485–503, 1997.

[16] M. J. Bluck and M. J. Wolfendale, "An analytical solution to the heat transfer problem in thick-walled hunt flow," *International Journal of Heat and Fluid Flow*, vol. 64, pp. 103–111, 2017.

[17] M.-J. Ni, R. Munipalli, N. B. Morley, P. Huang, and M. A. Abdou, "Validation case results for 2d and 3d mhd simulations," *Fusion Science and Technology*, vol. 52, no. 3, pp. 587–594, 2007.

[18] T. Zhou, Z. Yang, M. Ni, and H. Chen, "Code development and validation for analyzing liquid metal mhd flow in rectangular ducts," *Fusion Engineering and design*, vol. 85, no. 10-12, pp. 1736–1741, 2010.

[19] J. Mao and H. Pan, "Three-dimensional numerical simulation for magnetohydrodynamic duct flows in a staggered grid system," *Fusion Engineering and Design*, vol. 88, no. 3, pp. 145–150, 2013.

[20] S. Sahu and R. Bhattacharyay, "Validation of comsol code for analyzing liquid metal magnetohydrodynamic flow," *Fusion Engineering and Design*, vol. 127, pp. 151–159, 2018.

[21] R. J. Holroyd and J. S. Walker, "A theoretical study of the effects of wall conductivity, non-uniform magnetic fields and variable-area ducts on liquid-metal flows at high hartmann number," *Journal of Fluid Mechanics*, vol. 84, no. 3, pp. 471–495, 1978.

[22] A. Sterl, "Numerical simulation of liquid-metal mhd flows in rectangular ducts," *Journal of Fluid Mechanics*, vol. 216, pp. 161–191, 1990.

[23] R. Moreau, S. Smolentsev, and S. Cuevas, "Mhd flow in an insulating rectangular duct under a non-uniform magnetic field," *PMC Physics B*, vol. 3, no. 1, pp. 1–43, 2010.

[24] I. M. Gelfgat, D. Peterson, and E. Shcherbinin, "Velocity structure of flows in nonuniform constant magnetic fields. i-numerical calculations," *Magnitnaia Gidrodinamika*, vol. 14, no. 1, pp. 66–72, 1978.

[25] Y. Gelfgat and S. Olshanskii, "Velocity structure of flows in non-uniform constant magnetic fields. ii. experimental results," *Magnetohydrodynamics*, vol. 14, no. 2, pp. 23–26, 1978.

[26] S. Cuevas, S. Smolentsev, and M. A. Abdou, "On the flow past a magnetic obstacle," *Journal of Fluid Mechanics*, vol. 553, pp. 227–252, 2006.

[27] S. Cuevas, S. Smolentsev, and M. Abdou, "Vorticity generation in creeping flow past a magnetic obstacle," *Physical Review E*, vol. 74, no. 5, p. 056301, 2006.

[28] E. Votyakov and S. C. Kassinos, "Core of the magnetic obstacle," *Journal of Turbulence*, no. 11, p. N49, 2010.

[29] E. Votyakov, Y. Kolesnikov, O. Andreev, E. Zienicke, and A. Thess, "Structure of the wake of a magnetic obstacle," *Physical review letters*, vol. 98, no. 14, p. 144504, 2007.

[30] E. V. Votyakov, E. Zienicke, and Y. B. Kolesnikov, "Constrained flow around a magnetic obstacle," *Journal of Fluid Mechanics*, vol. 610, pp. 131–156, 2008.

[31] A. Thess, E. V. Votyakov, and Y. Kolesnikov, "Lorentz force velocimetry," *Physical Review Letters*, vol. 96, no. 16, p. 164501, 2006.

[32] A. Thess, E. Votyakov, B. Knaepen, and O. Zikanov, "Theory of the lorentz force flowmeter," *New Journal of Physics*, vol. 9, no. 8, p. 299, 2007.

[33] X. Wang, Y. Kolesnikov, and A. Thess, "Numerical calibration of a lorentz force flowmeter," *Measurement Science and Technology*, vol. 23, no. 4, p. 045005, 2012.

[34] C. Heinicke, "Spatially resolved measurements in a liquid metal flow with lorentz force velocimetry," *Experiments in fluids*, vol. 54, pp. 1–8, 2013.

[35] G. Pulugundla, C. Heinicke, C. Karcher, and A. Thess, "Lorentz force velocimetry with a small permanent magnet," *European Journal of Mechanics-B/Fluids*, vol. 41, pp. 23–28, 2013.

[36] D. Jian and C. Karcher, "Electromagnetic flow measurements in liquid metals using time-of-flight lorentz force velocimetry," *Measurement science and technology*, vol. 23, no. 7, p. 074021, 2012.

[37] A. Wegfrass, C. Diethold, M. Werner, C. Resagk, T. Fröhlich, B. Halbedel, and A. Thess, "Flow rate measurement of weakly conducting fluids using lorentz force velocimetry," *Measurement Science and Technology*, vol. 23, no. 10, p. 105307, 2012.

[38] S. Vasilyan and T. Froehlich, "Direct lorentz force compensation flowmeter for electrolytes," *Applied Physics Letters*, vol. 105, no. 22, p. 223510, 2014.

[39] S. Vasilyan, R. Ebert, M. Weidner, M. Rivero, B. Halbedel, C. Resagk, and T. Fröhlich, "Towards metering tap water by lorentz force velocimetry," *Measurement Science and Technology*, vol. 26, no. 11, p. 115302, 2015.

[40] C. Lara, A. Figueroa, and S. Cuevas, "Nested dipolar vortices driven by electromagnetic forces in a thin liquid metal layer.," *Magnetohydrodynamics (0024-998X)*, vol. 53, no. 1, 2017.

[41] X.-D. Zhang and H.-L. Huang, "Blockage effects on viscous fluid flow and heat transfer past a magnetic obstacle in a duct," *Chinese Physics B*, vol. 22, no. 7, p. 075202, 2013.

[42] F. Samsami, Y. Kolesnikov, and A. Thess, "Vortex dynamics in the wake of a magnetic obstacle," *Journal of Visualization*, vol. 17, pp. 245–252, 2014.

[43] E. Votyakov and S. C. Kassinos, "On the analogy between streamlined magnetic and solid obstacles," *Physics of Fluids*, vol. 21, no. 9, p. 097102, 2009.

[44] S. Prinz, V. Bandaru, Y. Kolesnikov, D. Krasnov, and T. Boeck, "Numerical simulations of magnetohydrodynamic flows driven by a moving permanent magnet," *Physical Review Fluids*, vol. 1, no. 4, p. 043601, 2016.

[45] D. Domınguez, A. Beltrán, J. Román, S. Cuevas, and E. Ramos, "Experimental and theoretical study of the dynamics of wakes generated by magnetic obstacles," *Magnetohydrodynamics*, vol. 51, no. 2, pp. 215–224, 2015.

[46] O. Zikanov, D. Krasnov, T. Boeck, A. Thess, and M. Rossi, "Laminar-turbulent transition in magnetohydrodynamic duct, pipe, and channel flows," *Applied Mechanics Reviews*, vol. 66, no. 3, 2014.

[47] V. Bandaru, T. Boeck, and J. Schumacher, "Turbulent magnetohydrodynamic flow in a square duct: Comparison of zero and finite magnetic reynolds number cases," *Physical Review Fluids*, vol. 3, no. 8, p. 083701, 2018.

[48] S. Kenjereš, S. Ten Cate, and C. Voesenek, "Vortical structures and turbulent bursts behind magnetic obstacles in transitional flow regimes," *International journal of heat and fluid flow*, vol. 32, no. 3, pp. 510–528, 2011.

[49] S. Kenjereš, "Energy spectra and turbulence generation in the wake of magnetic obstacles," *Physics of Fluids*, vol. 24, no. 11, p. 115111, 2012.

[50] Y. Cuypers, A. Maurel, and P. Petitjeans, "Vortex burst as a source of turbulence," *Physical review letters*, vol. 91, no. 19, p. 194502, 2003.

[51] S. Tympel, T. Boeck, and J. Schumacher, "Laminar and transitional liquid metal duct flow near a magnetic point dipole," *Journal of fluid mechanics*, vol. 735, pp. 553–586, 2013.

[52] M. Sheikholeslami, M. Gorji-Bandpy, and D. D. Ganji, "Review of heat transfer enhancement methods: Focus on passive methods using swirl flow devices," *Renewable and Sustainable Energy Reviews*, vol. 49, pp. 444–469, 2015.

[53] O. G. Cassells, W. K. Hussam, and G. J. Sheard, "Heat transfer enhancement using rectangular vortex promoters in confined quasi-two-dimensional magnetohydrodynamic flows," *International Journal of Heat and Mass Transfer*, vol. 93, pp. 186–199, 2016.

[54] M. Modestov, E. Kolemen, A. Fisher, and M. Hvasta, "Electromagnetic control of heat transport within a rectangular channel filled with flowing liquid metal," *Nuclear Fusion*, vol. 58, no. 1, p. 016009, 2017.

[55] A. H. Hamid, W. K. Hussam, and G. J. Sheard, "Combining an obstacle and electrically driven vortices to enhance heat transfer in a quasi-two-dimensional mhd duct flow," *Journal of Fluid Mechanics*, vol. 792, pp. 364–396, 2016.

[56] M. Gallo, H. Nemati, B. Boersma, R. Pecnik, P. Attrotto, and P. Colonna, ""magnetic-ribs" in fully developed laminar liquid–metal channel flow," *International Journal of Heat and Fluid Flow*, vol. 56, pp. 198–208, 2015.

[57] X. Zhang and H. Huang, "Effect of local magnetic fields on electrically conducting fluid flow and heat transfer," *Journal of heat transfer*, vol. 135, no. 2, 2013.

[58] X. Zhang and H. Huang, "Heat transfer enhancement of mhd flow by a row of magnetic obstacles," *Heat Transfer Research*, vol. 46, no. 12, 2015.

[59] I. G. Currie, *Fundamental mechanics of fluids.* CRC press, 2016.

[60] J. D. Jackson, *Classical electrodynamics.* John Wiley & Sons, 2021.

[61] P. A. Davidson, *An introduction to magnetohydrodynamics.* Cambridge, 2001.

[62] S. Smolentsev, S. Cuevas, and A. Beltrán, "Induced electric current-based formulation in computations of low magnetic reynolds number magnetohydrodynamic flows," *Journal of Computational Physics*, vol. 229, no. 5, pp. 1558–1572, 2010.

[63] R. J. Moreau, *Magnetohydrodynamics*, vol. 3. Springer Science & Business Media, 1990.

[64] H. K. Versteeg and W. Malalasekera, *An introduction to computational fluid dynamics: the finite volume method.* Pearson education, 2007.

[65] E. P. Furlani, *Permanent magnet and electromechanical devices: materials, analysis, and applications.* Academic press, 2001.

[66] V. Solano-Olivares, "Estudio numérico de flujos magnetohidrodinámicos de metal líquido en ductos para el mejoramiento de la transferencia de calor.," Master's thesis, Universidad Nacional Autónoma de México, México., 2018.

[67] J. Pérez-Barrera, *Experimental and numerical study of magnetohydrodynamic flow instabilities in a cylindrical cavity.* PhD thesis, Universidad Nacional Autónoma de México, México., 2017.

[68] M.-J. Ni, R. Munipalli, N. B. Morley, P. Huang, and M. A. Abdou, "A current density conservative scheme for incompressible mhd flows at a low magnetic reynolds number. part i: On a rectangular collocated grid system," *Journal of Computational Physics*, vol. 227, no. 1, pp. 174–204, 2007.

[69] M.-J. Ni, R. Munipalli, P. Huang, N. B. Morley, and M. A. Abdou, "A current density conservative scheme for incompressible mhd flows at a low magnetic reynolds number. part ii: On an arbitrary collocated mesh," *Journal of Computational Physics*, vol. 227, no. 1, pp. 205–228, 2007.

[70] V. Solano-Olivares, S. Cuevas, and A. Figueroa, "Liquid metal mhd flow and heat transfer in a rectangular duct with perfectly conducting walls perpendicular to the applied magnetic field," *Suplemento de la Revista Mexicana de Física*, vol. 1, no. 2, pp. 38–44, 2020.

[71] L. Bühler, "Instabilities in quasi-two-dimensional magnetohydrodynamic flows," *Journal of Fluid Mechanics*, vol. 326, pp. 125–150, 1996.

[72] P. Davidson, *An introduction to Magnetohydrodynamics*, vol. 25. Cambridge University Press, 2017.

[73] A. Figueroa, S. Cuevas, and E. Ramos, "Lissajous trajectories in electromagnetically driven vortices," *Journal of Fluid Mechanics*, vol. 815, pp. 415–434, 2017.

[74] E. V. Votyakov and E. Zienicke, "Numerical study of liquid metal flow in a rectangular duct under the influence of a heterogenous magnetic field," *arXiv preprint arXiv:0705.0633*, 2007.

[75] R. L. Webb, "Performance evaluation criteria for use of enhanced heat transfer surfaces in heat exchanger design," *international journal of heat and mass transfer*, vol. 24, no. 4, pp. 715–726, 1981.

[76] C. Heinicke, S. Tympel, G. Pulugundla, I. Rahneberg, T. Boeck, and A. Thess, "Interaction of a small permanent magnet with a liquid metal duct flow," *Journal of Applied Physics*, vol. 112, no. 12, p. 124914, 2012.

[77] W. K. Hussam and G. J. Sheard, "Heat transfer in a high hartmann number mhd duct flow with a circular cylinder placed near the heated side-wall," *International Journal of Heat and Mass Transfer*, vol. 67, pp. 944–954, 2013.

[78] M.-J. Ni, R. Munipalli, N. B. Morley, P. Huang, and M. A. Abdou, "A current density conservative scheme for incompressible mhd flows at a low magnetic reynolds number. part i: On a rectangular collocated grid system," *Journal of Computational Physics*, vol. 227, no. 1, pp. 174–204, 2007.

[79] G.-B. Lee, C.-C. Chang, S.-B. Huang, and R.-J. Yang, "The hydrodynamic focusing effect inside rectangular microchannels," *Journal of Micromechanics and Microengineering*, vol. 16, no. 5, p. 1024, 2006.

[80] K. A. Hoffmann and S. T. Chiang, "Computational fluid dynamics volume i," *Engineering education system*, 2000.

[81] M. Vinokur, "On one-dimensional stretching functions for finite-difference calculations," *Journal of Computational Physics*, vol. 50, no. 2, pp. 215–234, 1983.

[82] U. Ghia, K. N. Ghia, and C. Shin, "High-re solutions for incompressible flow using the navier-stokes equations and a multigrid method," *Journal of computational physics*, vol. 48, no. 3, pp. 387–411, 1982.